

THESIS

EVALUATING THE IMPACT OF HIERARCHICAL DEEP-WATER SLOPE CHANNEL
ARCHITECTURE ON FLUID FLOW BEHAVIOR, CRETACEOUS TRES PASOS
FORMATION, CHILE

Submitted by
Andrew Ruetten
Department of Geosciences

In partial fulfillment of requirements
For the Degree of Master of Science
Colorado State University
Fort Collins, Colorado
Spring 2021

Master's Committee:

Advisor: Lisa Stright

Michael Ronayne
Ryan Bailey

Copyright by Andrew John Ruetten 2021

All Rights Reserved

ABSTRACT

EVALUATING THE IMPACT OF HIERARCHICAL DEEP-WATER SLOPE CHANNEL ARCHITECTURE ON FLUID FLOW BEHAVIOR, CRETACEOUS TRES PASOS FORMATION, CHILE

Channelized deep-water reservoirs inherently contain sub-seismic scale heterogeneity, resulting in uncertainty when evaluating reservoir connectivity and flow patterns. Stratigraphic architectural features, including stacked channel elements, channel element fill, mass transport deposits (MTDs), and channel base drapes, can have a complex and significant impact on fluid flow pathways. While this detailed stratigraphic architecture can be difficult to capture at the development scale, it can be effectively modeled at the sector scale using high-resolution outcrop data. The characterization of flow behaviors and reservoir performance at this finer scale can then be used in the construction of lower-resolution development-scale simulations. This study uses a three-part sensitivity analysis to test how fluid flow behavior responds to channel element stacking patterns, net to gross ratio, channel base drape coverage, and MTD properties. First, simplified models are used to isolate key flow behaviors. Then, field data is incorporated from the seismic-scale Laguna Figueroa outcrop of the Cretaceous Tres Pasos Formation, Magallanes Basin, Chile to construct a deterministic outcrop model that incorporates realistic stacking patterns and architectural features, including MTDs. Finally, stochastic object-based methods are used to try to replicate the flow characteristics of the outcrop model using established geostatistical methods and limited data input. Fluid flow was simulated using a constant flux aquifer at the base of the model

and three producing wells at the top, and the results of the three modeling methods were compared in an effort to elucidate key flow behaviors.

ACKNOWLEDGEMENTS

This study builds upon a large body of geologic research conducted by the Chile Slope Systems (CSS) Joint Industry Project, which is a collaboration between Colorado State University, Virginia Tech University, the University of Calgary, and a bevy of industry sponsors over multiple phases of research, including Chevron, Repsol, Hess, Nexen/CNOOC, ConocoPhillips, BHP Billiton, Anadarko, Equinor, Petrobras, and Shell. Brian Romans, Steve Hubbard, Ryan Macauley, Sean Fletcher, and Sarah Southern performed the field work, data collection, and interpretation of the Laguna Figueroa outcrop, which were the inspiration and building blocks of this study. Much of the groundwork for the deterministic model was completed by Casey Meirovitz, who was also an invaluable resource while navigating the intricacies of geocellular modeling in Petrel. A special thank you to Lisa Stright, who provided expert guidance while letting me explore my research questions at my own pace. Finally, thank you to my friends and instructors in the CSU Geoscience Department for making my time in Fort Collins truly memorable, and to my family for their steadfast love and support.

TABLE OF CONTENTS

ABSTRACT.....	iii
ACKNOWLEDGEMENTS.....	iv
CHAPTER 1: INTRODUCTION.....	1
CHAPTER 2: GEOLOGIC BACKGROUND OF THE MAGALLANES BASIN.....	6
2.1 Tectonic Setting.....	6
2.2 Basin Stratigraphy.....	8
CHAPTER 3: STUDY AREA - LAGUNA FIGUEROA OUTCROP.....	10
3.1 Outcrop Description.....	10
3.2 Hierarchical Architecture.....	10
3.3 Facies.....	14
3.4 Channel Base Drapes.....	16
3.5 Levee/Overbank Deposits.....	16
3.6 Mass Transport Deposits.....	17
CHAPTER 4: THREE-PART SENSITIVITY ANALYSIS.....	18
4.1 Description of Analysis.....	18
4.2 Metrics.....	20
4.3 Simple Models.....	21
4.3.1 Description of Simple Model Analysis.....	21
4.3.2 Model Construction.....	21
4.3.3 Sensitivity Variables.....	26
4.3.4 Flow Simulation.....	30
4.3.5 Simple Model Results.....	33
4.3.5.1 Drape Results.....	33
4.3.5.2 NTG Results.....	35
4.4 Deterministic Outcrop Model.....	37
4.4.1 Description of Deterministic Model Analysis.....	37
4.4.2 Model Construction.....	37

4.4.2.1 Model Framework.....	38
4.4.2.2 Property Modeling.....	44
4.4.3 Sensitivity Variables.....	46
4.4.4 Flow Simulation.....	50
4.4.5 Deterministic Model Results.....	52
4.5 Stochastic Models.....	54
4.5.1 Description of Stochastic Model Analysis.....	54
4.5.2 Model Construction.....	54
4.5.3 Sensitivity Variables.....	61
4.5.4 Flow Simulation.....	63
4.5.5 Stochastic Model Results.....	65
CHAPTER 5: DISCUSSION.....	68
5.1 Flow Baffles.....	69
5.1.1 Baffled Flow in Drape and MTD Proportion Analyses.....	69
5.1.2 Baffled Flow in NTG Analyses.....	73
5.2 Flow Barriers.....	75
5.3 Reservoir Compartmentalization.....	78
CHAPTER 6: CONCLUSIONS AND FUTURE WORK.....	81
6.1 Conclusions.....	81
6.2 Future Work.....	83
REFERENCES.....	86
APPENDIX A: Flow Simulation Results.....	92
APPENDIX B: Modeling Inputs.....	99
APPENDIX C: Sample Flow Simulation File.....	101

CHAPTER 1: INTRODUCTION

Channelized deep-water turbidite systems are widely distributed along continental margins and are often prolific hydrocarbon reservoirs (Posamentier and Kolla, 2003; Mayall et al., 2006; Deptuck et al., 2007; Labourdette and Bez, 2010; McHargue et al., 2010, 2011; Jackson et al., 2019). These systems are architecturally and stratigraphically complex, with variable channel element fill (e.g., variable net-to-gross, grain-sizes and drape coverage; Figure 1A) and hierarchical arrangement (e.g., stacking patterns, presence or absence of mass transport deposits; Figure 1B) (Sprague et al., 2005; Mayall et al., 2006; Hubbard et al., 2014; Meirovitz et al., 2020). This complexity strongly influences reservoir connectivity and flow behavior, with architectural features such as channel element base drapes and mass transport deposits (MTDs) acting as flow baffles or barriers (Moscardelli et al., 2006; Stright, 2006; Alpak et al., 2011, 2013, 2014; Sun and Alves, 2020), and net to gross ratio (NTG) impacting inter-channel element facies juxtaposition (Jackson et al., 2019; Meirovitz et al. 2020). From exploration to development, this heterogeneity creates uncertainty in volume estimates and recovery predictions, which can increase exploration and production costs if not properly mitigated through detailed reservoir characterization and modeling (Abreu et al., 2003; Stewart et al.).

Despite an increased focus on deep-water slope systems, however, reservoir characterization remains a challenge. High-resolution (65 Hz) 3D seismic surveys can be useful for constraining coarse-scale architectural features such as channel complex sets and even channel complexes (Labourdette, 2007), but finer-scale heterogeneity within and between channel elements (e.g., thin beds, shale drapes, inner levees) is sub-seismic scale (Labourdette et al., 2006). Well logs and core can be used to constrain the seismic interpretation with higher resolution data, but their use is limited by the number and spacing of wells, particularly in exploration plays

(Mayall et al., 2006). Incorporating a more comprehensive view of system architecture into geocellular models is critical for producing predictive flow simulations, as an unrealistically homogenous or stochastic model can create an artificially uniform sweep of the system, delaying water breakthrough times and overestimating production (Stewart et al., 2008, Meirovitz et al. 2020). Therefore, a variety of modeling methods are often utilized at different resolutions to capture multiple levels of architecture (Deptuck et al., 2003, 2007; Mayall et al., 2006; Hovadik and Larue, 2007; Sylvester et al., 2010; McHargue et al., 2011; Jackson et al., 2019; Meirovitz et al., 2020).

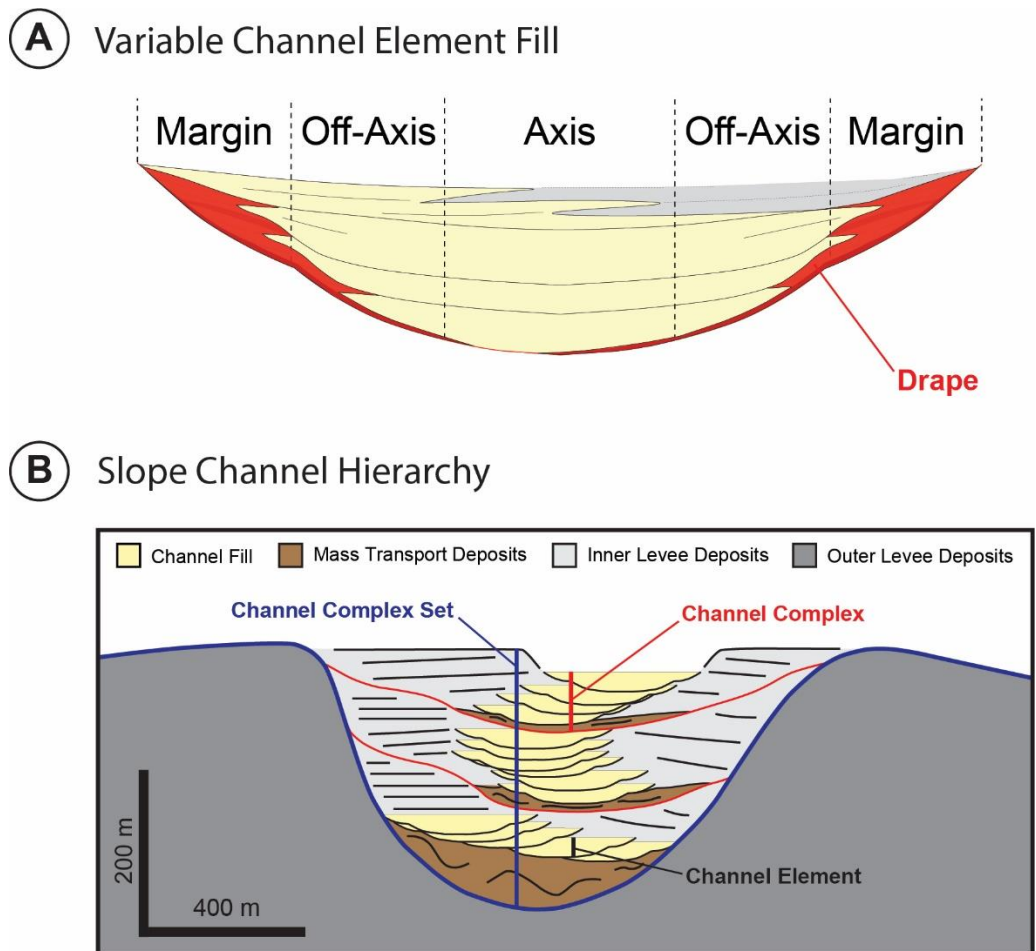


Figure 1. (A) Stylized cross section of a single channel element highlighting heterogeneous fill within a channel element. Axis, off-axis, and margin channel positions are shown, as well as channel base drapes in red. Modified from Vento, 2020. (B) Slope channel hierarchy highlighting architectural heterogeneity between channel elements. Modified from Daniels, 2019.

Previous studies that model slope channel system architecture fall into three categories, 1) bed- to element(geobody)-scale models (or herein referred to as “simple” models) that test the impact of detailed outcrop-scale architecture on fluid flow, 2) full-scale deterministic outcrop models that reconstruct outcrops in three dimensions and test the impact of realistic, reservoir-scale architecture on fluid flow, or 3) traditional and novel stochastic approaches. Meirovitz et al. (2020) used bed- to geobody-scale simulations to explore the influence of intra-channel element heterogeneity on fluid flow between channel elements. The study focused on flow between two simplified channel elements arranged in systematically varying stacking patterns and did not address larger-scale architectural features. Jackson et al. (2019) used larger-scale outcrop modeling tied to outcrop observations and measured data and a digital elevation map. The study focused on connectivity between channel elements controlled by high-resolution bed-scale heterogeneity, and the influence of channel element stacking pattern, net to gross ratio, and channel base drapes. However, the outcrop model was not hierarchically organized, did not include MTDs, and stopped short of full-model flow simulations.

Various authors approach the issues of reservoir connectivity and the impacts of various architectural features using stochastic modeling methods. Hovadik and Larue (2006, 2008, and 2011) utilized Boolean or object-based modeling methods to generate reservoirs for flow simulation, but focused on reservoir connectivity and waterflood performance, not generating realistic channel architecture. Multi-point geostatistics (MPS) were used by Caers and Zhang (2002) to build reservoir models from training images and by Stright (2006) to model channel base drapes, but these studies were more limited in focus, and were not attempting to capture large-scale architecture. McHargue et al. (2010) and Sylvester et al. (2011) used event-based forward modeling to create realistic reservoir architectures, but while this process is able to reproduce

architecture from element to complex set scales, it is very dependent upon rules and boundary conditions. Alpak et al. (2011, 2013, and 2014) used geologically realistic surface-based models and extensive flow simulation to understand the impacts of a large number of stratigraphic and engineering parameters. While these simulation studies are comprehensive, they did not address system-scale architectural like MTDs or complex-level stacking patterns, nor did they address how to build predictive subsurface models from well data. While simple and deterministic modeling workflows provide the opportunity to evaluate realistic architecture on fluid flow, there is not a direct link to predictive subsurface models. Stochastic models are extensively used for subsurface prediction, but their ability to predict realistic flow behavior is difficult to evaluate.

This study explores these three primary modeling approaches (simple, deterministic, and stochastic) to more tightly couple rocks, fluid flow, and modeling. The three-part analysis addresses the overarching question: do particular arrangements and proportions of hierarchical architectural elements (i.e., channel elements and their fill style, stacking patterns, and proportion and properties of MTDs) have distinct characteristic flow behaviors, and if so, can these characteristic flow behaviors be modeled with stochastic modeling algorithms? To answer this question, a three-part study was designed to systematically address three objectives: 1) construct and analyze simple models to isolate the flow characteristics of different stacking patterns and fill; 2) construct a deterministic outcrop model containing MTDs, realistic stacking patterns and fill to evaluate characteristic flow behaviors in comparison to the simple models; and 3) assess the ability of stochastic reservoir modeling methods to capture these characteristic flow behaviors.

This study focuses on the Laguna Figueroa outcrop of the Cretaceous Tres Pasos Formation in Chilean Patagonia. The 2.5 km long, 200 m thick, oblique dip-oriented outcrop is comprised of two channel complex sets containing seven complexes and 20 individual channel elements. MTDs,

channel-base drapes, and inner levee thin-bed deposits are also observed (Macauley and Hubbard, 2013; Pemberton et al., 2018; Southern et al., 2017; Jackson et al., 2019). The outcrop is well preserved and offers 3D exposure through various cuts and gullies, allowing detailed observation and interpretation of architecture from the bed scale to the complex set scale. Laguna Figueroa is also found to be analogous to many slope channel systems globally in terms of stratigraphy and depositional setting (Fildani et al. 2013; Macauley and Hubbard, 2013; Covault et al., 2016; Daniels et al., 2018), making it a prime candidate for this type of sensitivity analysis. The outcrop model was used as the basis for the stochastic modeling work, and was the inspiration for the stacking patterns chosen for the simple model analysis.

CHAPTER 2: GEOLOGIC BACKGROUND OF THE MAGALLANES BASIN

2.1 Tectonic Setting

The Magallanes Basin of Patagonian Chile is a retroarc foreland basin running parallel to the Andean fold-thrust belt (Romans et al., 2011; Pemberton et al., 2018; Jackson et al., 2019). Beginning in the Mid to Late Jurassic, the southern Andes underwent a regional extensional event associated with the breakup of Gondwana, causing crustal thinning and rift-related volcanism (Romans et al., 2010; Fosdick et al., 2011). This extension concluded in the Late Jurassic to Early Cretaceous with the formation of the Rocas Verdes backarc basin (Dalziel, 1981; Fildani et al., 2003; Fosdick et al., 2011). As spreading rates in the southern Atlantic Ocean increased during the Early Cretaceous and subduction rates accelerated along the Pacific margin (Dalziel, 1986), the tectonic regime in the retroarc region of the Patagonian Andes transitioned from extensional to compressional, initiating the closure of the Rocas Verdes (Dalziel, 1982; Fosdick et al., 2011). These compressional forces resulted in an uplifted fold-thrust belt along the basin's western margin, creating crustal loading and foreland subsidence of the Magallanes Basin (Romans et al., 2010). This fold-thrust belt became the primary source of more than 4000 m of deep-water sedimentary fill into the basin over the next 20+ million years (Wilson, 1991; Romans et al., 2011). The stratigraphic fill in the Rocas Verdes and Magallanes Basins is detailed in Figure 2A, while a map of the primary geologic formations that are described in subsequent sections can be found in Figure 2B.

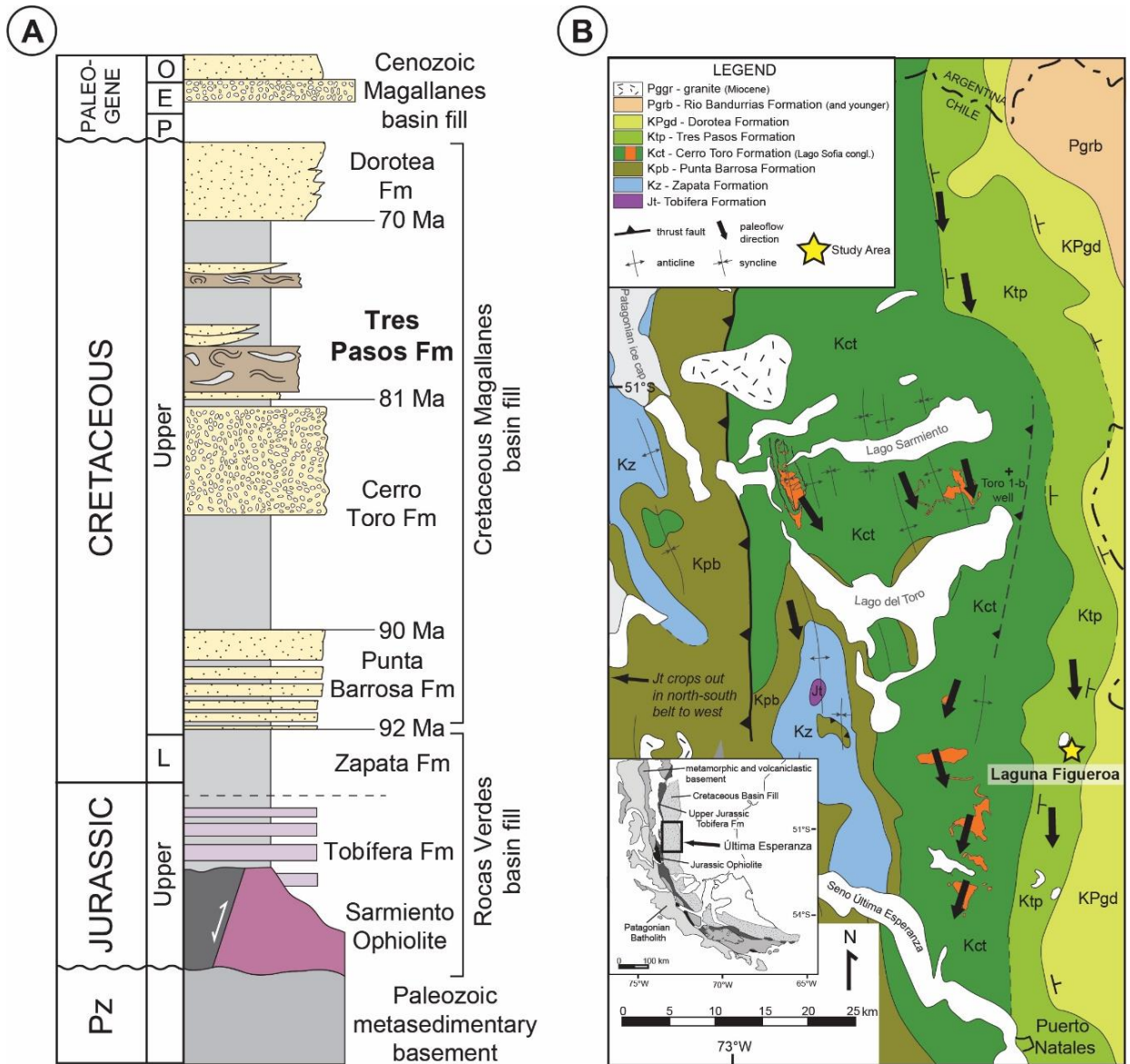


Figure 2. (A) Stratigraphic column of the Rocas Verdes and Magallanes Basin fill. Modified from Daniels et al., 2018 and Vento, 2020. (B) Geologic map of Última Esperanza District in southern Chile (modified from Romans et al., (2011); originally adapted from Wilson (1991) and Fosdick et al., (2011)), with inset image showing relative geographic location. Paleoflow direction is south/southeast along the axis of the basin. The Laguna Figueroa, marked with a star, is north of Puerto Natales along the Tres Pisos Formation band.

2.2 Basin Stratigraphy

Tobifera and Zapata

Stratigraphy within the Magallanes Basin reflects the changing tectonic regime of the Cretaceous and the evolution of the aforementioned fold-thrust belt (Romans et al., 2011). The closing of the Rocas Verdes Basin in the Early Cretaceous is marked in the stratigraphy by the Zapata Formation, a dark gray to black shale with rare thinly-bedded sands (Fildani and Hessler, 2005). The Zapata lies conformably over the marine volcanoclastics of the Tobifera Formation and the Sarmiento Ophiolites, indicating a very deep, restricted basin with a water depth of at least 2500 m (Fildani and Hessler, 2005; Romans et al., 2011).

Punta Barrosa

Transition from the Zapata Formation to the Punta Barrosa (~92-85 Ma) is related to the onset of Andean orogeny, and records the beginning of turbiditic sedimentation into the Magallanes Basin (Wilson 1991; Romans et al., 2011). The change is marked by an increased presence of thin to medium bedded sandstones and a decrease in thick mudstone packages, particularly in the upper sections (Romans et al., 2011). The Punta Barrosa is characterized by relatively thin sheets or fan-like lobate sand deposits that indicate a largely unconfined depositional setting. The system was likely confined to about a 100 km wide trough running parallel to the fold-thrust belt (Fildani and Hessler, 2005; Romans et al., 2011).

Cerro Toro

The change from the Punta Barrosa to the Cerro Toro Formation (~86-80 Ma) is evidenced by a cessation of coarse-grained beds and the appearance of the dark Cerro Toro mudstone (Katz, 1963; Romans et al., 2011). The Cerro Toro is predominantly composed of shale, but does contain a conglomeratic unit referred to as the Lago Sofia Member (Winn and Dott, 1979) near the center of the stratigraphic package (Katz, 1963; Hubbard et al., 2008; Romans et al., 2011). Additionally,

turbiditic sandstones and debris flow deposits are locally present (Crane and Lowe, 2008; Hubbard et al., 2008). The Cerro Toro represents a channel-levee complex running axially along the basin, where the channel bodies become increasingly amalgamated further down paleo-slope to the south (Jobe et al., 2009; Romans et al., 2011).

Tres Pasos

The Tres Pasos Formation (~80-70 Ma), which is the focus of this study, is recognized in section by the first prominent sandstone overlying the thick shale of the uppermost Cerro Toro (Katz, 1963; Romans et al., 2011). The lower Tres Pasos is composed primarily of lenticular to tabular sandstone packages and MTDs (Armitage et al., 2009), while the mostly fine-grained upper section incorporates coarse-grained deposits including turbidites, structureless sandstone, and mudstone-clast conglomerates (Shultz and Hubbard, 2005; Romans et al., 2011). The Tres Pasos is interpreted as a progradational slope system, with channel complex geometry and amalgamation strongly influenced by slope position (Hubbard et al., 2010; Romans et al., 2011).

Dorotea

The Dorotea Formation (~72-65 Ma) conformably overlies the Tres Pasos and represents the final filling stage of the Magallanes Basin (Covault et al., 2009; Romans et al., 2011). The formation is marked by the first significant sandstone overlying the mudstone-rich upper Tres Pasos Formation (Katz, 1963), and is composed primarily of shallow-water sandstone (Covault et al., 2009; Hubbard et al., 2010). The Dorotea is interpreted to be upward-shallowing, transitioning from upper slope to shallow marine, deltaic, and non-marine strata at the very top of the section (Macellari et al., 1989; Hubbard et al., 2010).

CHAPTER 3: STUDY AREA - LAGUNA FIGUEROA OUTCROP

3.1 Outcrop Description

The Upper Cretaceous-aged Tres Pasos formation is well preserved and exposed at Laguna Figueroa, located approximately 40 km north of Puerto Natales, Chile. The 2.5 km long, 300 m thick, oblique dip-oriented outcrop is composed of a series of turbiditic slope channel elements, representing the terminal phase of deep-water sedimentation in the Magallanes Basin (Fosdick et al., 2011; Romans et al., 2011; Hubbard et al., 2014; Meirovitz et al., 2020). Macauley and Hubbard (2013) utilized over 1600 m of cm-scale measured section, over 100 paleoflow measurements, and thousands of GPS data points to provide a detailed characterization of the outcrop (Macauley and Hubbard, 2013; Jackson et al., 2019).

3.2 Hierarchical Architecture

Channel elements, defined as distinct, mappable channelized sedimentary bodies, are the fundamental architectural component of the slope channel hierarchy at Laguna Figueroa. Multiple stacked, related channel elements form a channel complex, and two or more complexes form a channel complex set (McHargue et al., 2011; Macauley and Hubbard, 2013, Meirovitz et al., 2020). Three additional architectural components are present in the outcrop: mudstone drapes at the base of channel elements, mass transport deposits (MTDs) at the base of channel complexes, and inner-levee thin-bed deposits encasing the channelized elements (Macauley and Hubbard, 2013; Hubbard et al., 2014; Pemberton et al., 2018; Jackson et al., 2019). Each of these will be discussed more in this section.

Two complex sets have been interpreted at Laguna Figueroa, simply referred to as the Upper and Lower Figueroa (Fig. 3A; Hubbard et al., 2014). Eight channel elements have been

interpreted in the upper complex set (Fig. 3B), named (from youngest to oldest) Blue, Gabriela, Mistral, Lucila, Old Complex 6, Upper Pink, and Lower Pink (Fig. 4). These elements are divided into four distinct channel complexes, with Lower Pink, Upper Pink, and Blue each being contained within its own distinct complex. All elements have a standardized width of 400 m and thickness of 25 m, with the exception of Lower Pink, which is 800 m wide. The lower complex set (Fig. 3C) contains twelve channel elements, simply named (from youngest to oldest) L12 – L1 (Fig. 5). These elements are divided into three channel complexes and have a standardized 400 m width and 25 m thickness. The base of the Upper Figueroa incises into the top of the Lower Figueroa, creating connectivity between the two.

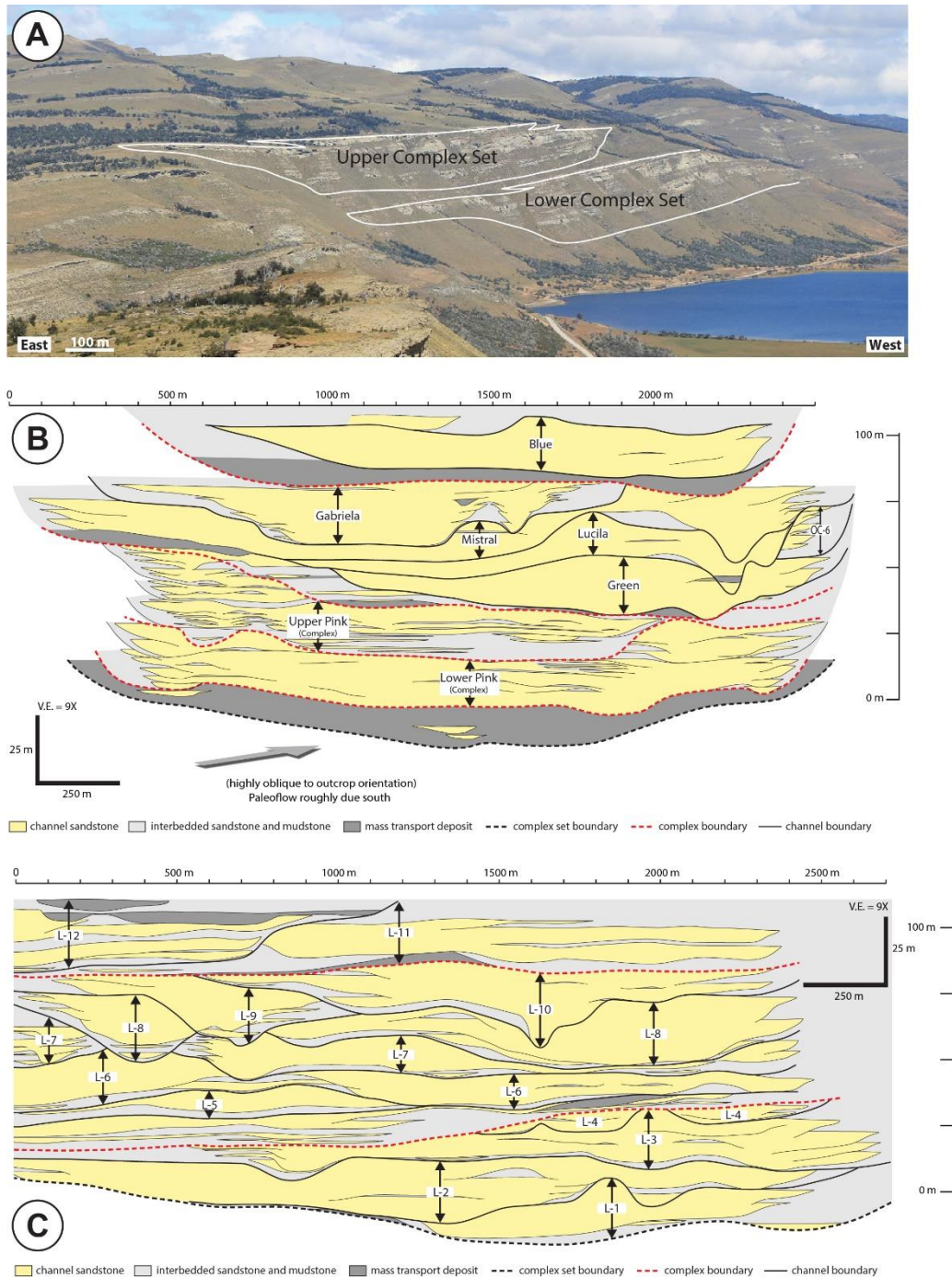
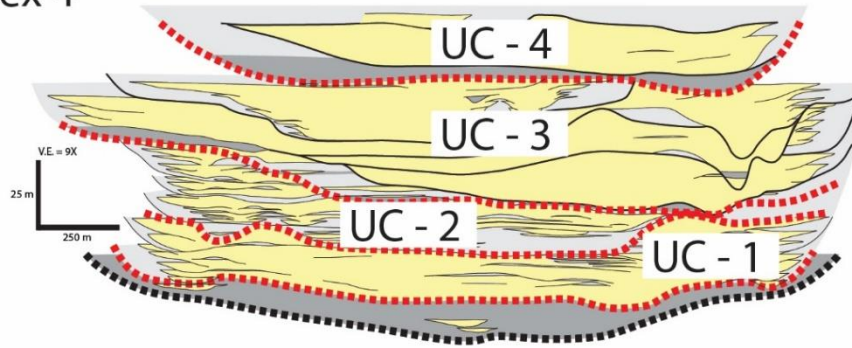


Figure 3. (A) Photo of the upper and lower channel complex sets at Laguna Figueroa with complex sets outlined (adapted from Daniels et al. (2019)). (B) Oblique dip-oriented cross section of Upper Figueroa with channel elements labeled. Channel complexes are separated by dashed red lines. Note that Upper and Lower Pink are each distinct complexes (adapted from Southern et al., (2017)). (C) Oblique dip-oriented cross section of Lower Figueroa with channel elements labeled. Channel complexes are separated by dashed red lines (adapted from Southern et al., (2017)).

Upper Complex 4



Upper Complex 3



Upper Complex 2 (Upper Pink)

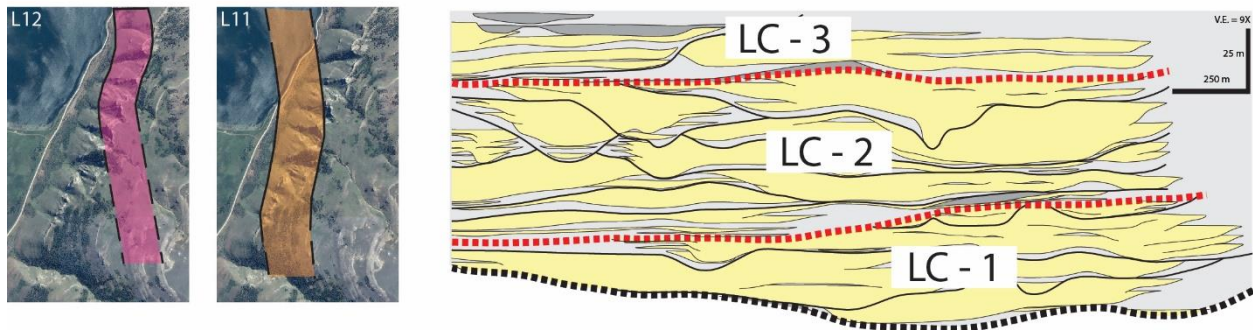


Upper Complex 1 (Lower Pink)

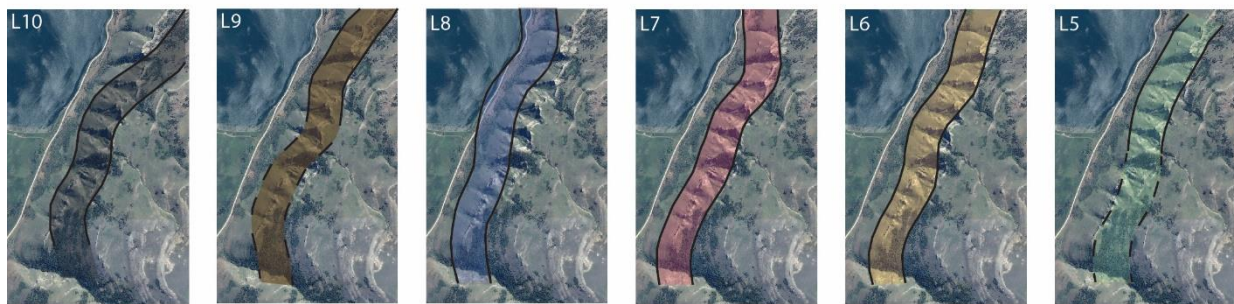


Figure 4. Interpreted channel planforms for the Upper Complex Set overlaid on a satellite image of the Laguna Figueroa outcrop. Planforms are organized by complex, with Upper Pink and Lower Pink assigned to their own complexes. Lower Pink is shown as a single, wide channel element, but is interpreted as a massive, highly amalgamated channel complex in outcrop. The planform used in the model (dashed lines) was edited from the original (solid lines) to accommodate this interpretation. A simplified cross section is included, highlighting the four channel complexes within the Upper Laguna Figueroa.

Lower Complex 3



Lower Complex 2



Lower Complex 1

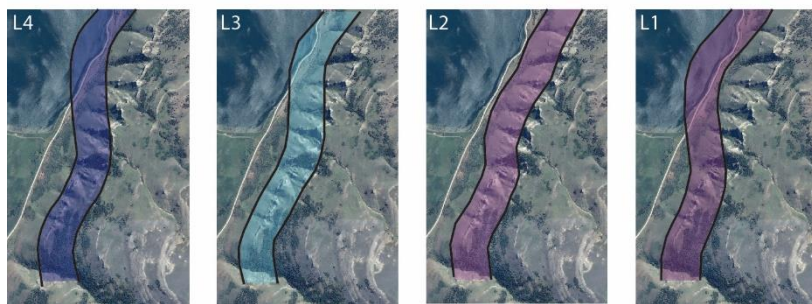


Figure 5. Interpreted channel planforms for the Lower Complex Set overlaid on a satellite image of the Laguna Figueroa outcrop. Planforms are organized by complex, and a simplified cross section is included, highlighting the three channel complexes within the Lower Laguna Figueroa. Dashed lines represent the assumed path of a channel element that was not visible in outcrop.

3.3 Facies

The outcrop characterization begins at the bed scale, where Macauley and Hubbard (2013) described three major facies associations [F1-F3]. These include: thick-bedded amalgamated sandstone [F1], thick- to thin-bedded semi-amalgamated sandstone [F2], and thin-bedded non-

amalgamated sandstone and siltstone [F3] (Fig. 6B). In general, these facies associations form the brunt of the internal channel element architecture, and are largely correlated with channel position. F1 is the principal component of the channel axes, while F3 is most closely associated with channel margins. F2 tends to be present between F1 and F3, in the “off-axis” portion of the elements (Fig. 6A, Macauley and Hubbard, 2013; Meirovitz et al., 2020).

This study utilizes two additional facies for modeling purposes MTD facies, which will be discussed more in this section, and “background” facies, which encompasses anything that is not within a channel element or MTD and is considered to have no flow properties and no storage.

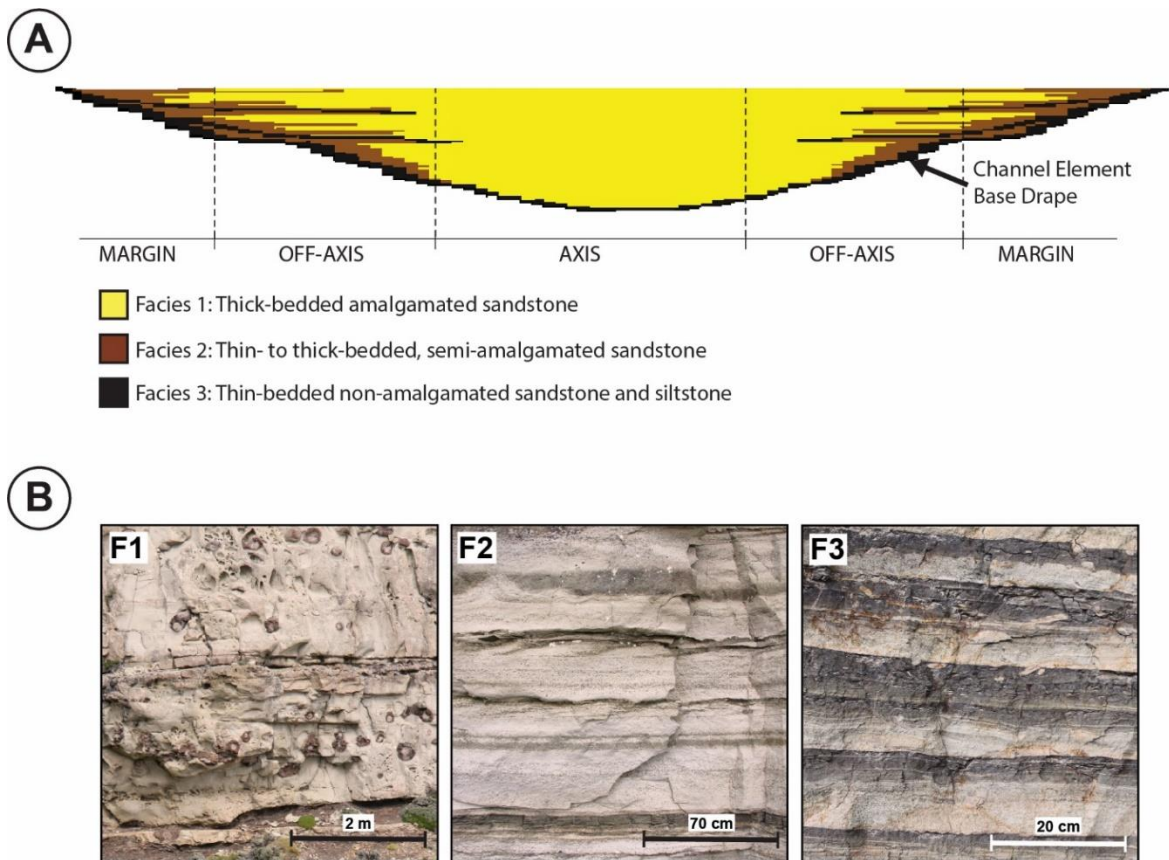


Figure 6. Modified from Meirovitz et al., 2020. (A) Generic channel element cross-section showing varying channel position and associated facies. (B) Representative facies photos including: F1- thick-bedded amalgamated sandstone; F2 – thin- to thick-bedded, semi-amalgamated sandstone; and F3 - thin-bedded non-amalgamated sandstone and siltstone.

3.4 Channel-base Drapes

Channel-base drapes are a result of sediment bypass within a channel element erosion surface or incision, where the coarser sediment of a turbidity current has continued down slope and only the tail of silt and mudstone remains (Mutti and Normark, 1987; Macauley and Hubbard, 2013; Hubbard et al., 2014). These drape deposits are primarily preserved on the channel element margins, but can rarely also remain along the more axial sections of the element (Barton et al., 2010; Hubbard et al., 2014; Meirovitz et al., 2020). Despite the relatively small proportion of sediment volume that drapes account for within the channel element (Hubbard et al., 2014), they can have a large impact on production by acting as a flow baffle or barrier between adjacent elements (Stright, 2006; Barton et al., 2010).

3.5 Levee/Overbank Deposits

Levee deposits are divided into two categories: external and internal levees. External levees wholly or partially bound an entire channel-levee system, and are associated with erosional master conduit surfaces (Kane and Hodgson, 2011; Macauley and Hubbard, 2013). These external levees are wedge shaped and thin perpendicularly away from the channel belt (Deptuck et al., 2003; Kane and Hodgson, 2011). Internal levees form as overbank deposits that partially spill from individual channel element conduits, but are unable to escape the confines of the channel-belt as a whole (Kane and Hodgson, 2011). At Laguna Figueroa, levees are made of up fine-grained, mudstone-prone turbiditic deposits, and are often poorly exposed in outcrop due to vegetative cover (Deptuck et al., 2003; Macauley and Hubbard, 2013; Hubbard, 2014). Levees are not the focus of this study, and are modeled as non-storage and non-flowing “background” facies in the modeling due to the mudstone-prone nature of the deposits.

3.6 Mass Transport Deposits (MTDs)

Mass transport deposit (MTD) is a general term for a deposit from various gravity-driven mass-wasting events, including slumps, slides, and debris flows (Posamentier and Kolla, 2003; Moscardelli and Wood, 2008; Armitage et al., 2009; Hubbard et al., 2009; Cardona et al., 2020). A series of stacked MTDs is sometimes referred to as a mass transport complex (MTC), but specific focus to MTD architecture has not been extensively studied in this field area. Therefore, this study will only refer to these deposits as MTDs. These deposits have a variety of lithologies and petrophysical properties, and can thus act as a reservoir, seal, or even source (Aplin and Macquaker, 2011; Cardona et al., 2020). In the Tres Pasos Formation, MTDs are typified by chaotically bedded mudstone and sandstone with rare outsized extra-basinal clasts and organic detritus (Fletcher, 2013). They are architectural elements that are present between the sandy channel elements and found at the bases of channel complexes or other large-scale channelform bodies (Deptuck et al., 2003; Armitage et al., 2009; Romans et al., 2011). In this study, MTDs are modeled as low porosity and permeability “seals,” and act as flow baffles or barriers depending on assigned permeability values and geometries.

CHAPTER 4: THREE-PART SENSITIVITY ANALYSIS

4.1 Description of Analysis

We present three sensitivity analyses with varying model complexity: 1) a series of simple models, 2) a deterministic outcrop model, and 3) a series of stochastic object-based models. Individual models were constructed in isolation, with similar rock properties and boundary conditions for each analysis that will be discussed in detail in each section. Two-phase (oil and water) flow simulations were then performed. Rather than a traditional injector-producer pairing, such as in a waterflood simulation, this study utilizes a constant flux aquifer at the base of each model coupled with three constant-rate producing wells situated in the uppermost channel element. Flow simulation results from each series of models were analyzed to create a more comprehensive picture of characteristic flow behaviors in stacked deep-water reservoirs.

The simple models use generic, idealized sets of stacked channel elements to test the fluid flow impacts of stacking pattern, channel-base drape coverage, and net to gross ratio. By focusing on straight and symmetrical channel elements, this study allows for the isolation of drape coverage and NTG as a function of stacking pattern, eliminating variability such as sinuosity and asymmetry. These simple models provide a foundation for the flow principles that govern the results of the more complex deterministic and stochastic models.

The deterministic outcrop model incorporates more architectural elements, including complex and complex set surfaces and associated mass transport deposits, to test the impacts of drape coverage, NTG, and variable MTD permeability. The outcrop model acts as our ground truth model, as it is the most realistic due to the incorporation of actual field data. It was constructed using channel element planforms and outcrop cross sections derived from measured sections and paleoflow measurements in the field. The complex stacking pattern of the deterministic model

incorporates elements of all three stacking patterns evaluated in the simple models, while the presence of MTDs adds another level of complexity. The outcrop model is a useful tool to evaluate more complex flow behaviors, but it is limited by the large volume of data required for construction and the difficulty of incorporating new data into the model.

The stochastic models use object-based modeling methods to test drape coverage, NTG, and variable MTD facies proportions. These models were constructed using complex set surfaces and pseudo-wells derived from the deterministic model as the only external input, and used a range of model realizations to add variability to the results. The object-based models are an attempt to simulate a scenario where a small amount of data is available, in this case a couple of seismically-resolvable erosional (complex set) surfaces and three wells. This method allows for a broad range of outcomes using the same limited input, and thus can be useful for de-risking purposes. However, using built-in software algorithms and a purely stochastic approach limits the stratigraphic realism of the results.

While each section of the three-part sensitivity analysis has its own distinct methods and focus, they are cohesive in that they test the impacts of critical variables at different levels of data availability. By utilizing all three methods, the aim is to decipher the relative impact of these key variables (drape, NTG, stacking pattern, MTD properties) at a more fundamental level, allowing the results to be adapted to a variety of exploration and production scenarios.

4.2 Metrics

Flow simulation results for the sensitivity analysis are evaluated using several different metrics: water breakthrough time (*BT*), recovery efficiency (*RE*), and the volume of cumulative oil produced at 0.1 pore volumes injected (*CUMoil @ 0.1 PVI*). *BT* is the amount of simulated time it takes for water to flow from the aquifer to the producing wells. *BT* is deemed to have been reached when the volumetric rate of water produced is 0.1% of the volumetric rate of total liquid (oil+water) production, a ratio known as water cut. This was an arbitrary water cut value chosen to standardize the results. As the simulated reservoirs are originally completely saturated with oil, any water production indicates that water has broken through from the aquifer. Recovery efficiency is a measure of the volume of cumulative oil produced (*CUMoil*) relative to the original oil in place (*OOIP*). The metric is a product of displacement efficiency and areal and vertical sweep efficiencies, and essentially describes the efficiency of fluid recovery (Fanchi, 2002). The volume of *CUMoil @ 0.1 PVI* is a way to look at early flow behavior in the system. The magnitude of this early produced volume is an indicator of whether fluid is effectively being displaced from aquifer to producer or if the displacement is being hindered by a flow baffle or barrier.

When comparing results between different stacking patterns (i.e. vertical, diagonal, and lateral) or different modeling methods (i.e. simple, deterministic, and stochastic), the results are often normalized relative to a base case model such as 0% *drape*, 100% *NTG*, or 0% *MTD* proportion.

4.3 Simple Models

4.3.1 Description of Simple Model Analysis

The first sensitivity analysis uses straight, symmetrical channel elements to isolate the flow characteristics of different stacking patterns and fill. Three distinct stacking patterns (vertical, diagonal, and lateral) provide a simple framework to quantify characteristic flow behaviors for each pattern. Internal channel element architecture (fill) is then incrementally added by systematically varying net to gross ratio and drape coverage.

4.3.2 Model Construction

Models each consist of five straight channel elements that measure 400 m wide, 2400 m long, and 25 m thick. Channel elements were created using three polylines: two level lines for the channel edges and one line offset by 25 m for the channel centerline. Channel surfaces were gridded using a built-in minimum curvature algorithm, and trimmed to be flat at the top of the channel element surface. This process is detailed more fully in Chapter 2: Deterministic Outcrop Model, including an example of channel element construction in Figure 17. The five channel elements are stacked in a way representative of offsets seen in outcrop, with vertical offsets ranging from 0-15 meters. This is consistent with the roughly 0-20 meters of offset seen in the deterministic model, and ensures that there is sufficient overlap between adjacent channels for fluid flow to not be restricted at high *NTG* values. The models are gridded at a 15 m x 15 m grid increment, with 5 m cell thickness. Layering is flat, and follows the model top rather than the channel element bases (Fig. 7).

Internal channel element fill was created from a geometrical trend, where the properties gradationally change as a function of distance from the channel element center line that was used

in the creation of the element surface. The following process and equations are based on previous work from Meirovitz et al., 2018, and the calculated properties are visualized in Figure 8.

The calculations begin with *NTG*, which utilizes a normalized distance from centerline (*NormDist*) (Fig. 8A) property and an elevation above zone base (*EAZB*) (Fig. 8B) property. Equation 1, below, is used to scale the *NTG* values to achieve the outwardly decreasing, curvilinear distribution seen in Figure 8C. The *NTG* values are then clipped between 0 and 1.

$$NTG = (-X * NormDist) + 1 + (EAZB * 0.02) \quad (1)$$

To create a range of *NTG* values for the sensitivity analysis, the multiplier in front of the *NormDist* property was manually adjusted until the desired average *NTG* value for the model was achieved (Table 2). Porosity (φ) (Fig. 8D), horizontal permeability (K_{xy}) (Fig. 8E), and vertical permeability (K_z) (Fig. 8F) are then derived from the normalized *NTG* property.

$$\varphi = (0.1 * (1 - NTG)) + (0.3 * NTG) \quad (2)$$

Equation 2 calculates porosity such that a *NTG* value of 1 correlates with a φ value of 0.3, which is consistent with the value for channel axis given in Stewart et al., 2008.

$$K_{xy} = 721.35 * Ln(\varphi) + 1661 \quad (3)$$

$$K_z = if(NTG > 0.9, K_{xy}, 0.1 * K_{xy}) \quad (4)$$

K_{xy} and K_z are then calculated in Equations 3 and 4 based on data obtained from industry partners for deep-water channelized systems in the Gulf of Mexico and West Africa (Meirovitz et al., 2018).

In these equations, it is assumed that shale interbeds restrict fluid flow in the vertical direction, while not significantly impacting horizontal flow. Channel axes ($NTG > 0.9$) are considered to be free of shale interbeds, and therefore are modeled as isotropic, whereas the channel margins show restricted vertical flow.

$$Drape = if((NormDist < X)Or(EAZB > 2.5), 1, 0) \quad (5)$$

The calculation for channel base drapes is unrelated to NTG . A transmissibility multiplier is used along the basal cells of each channel element, where a value of 0 constitutes a no-flow boundary and a value of 1 results in unrestricted flow. Equation 5 is a generic formula for creating a *drape* property (Fig. 8G) that extends from the channel element margins inward toward the center. The X variable, which relates to the normalized distance from centerline property, controls the percentage of the channel element that is draped (Table 3). The elevation above zone base property is used to restrict the drapes to the bottommost cells in each channel element.

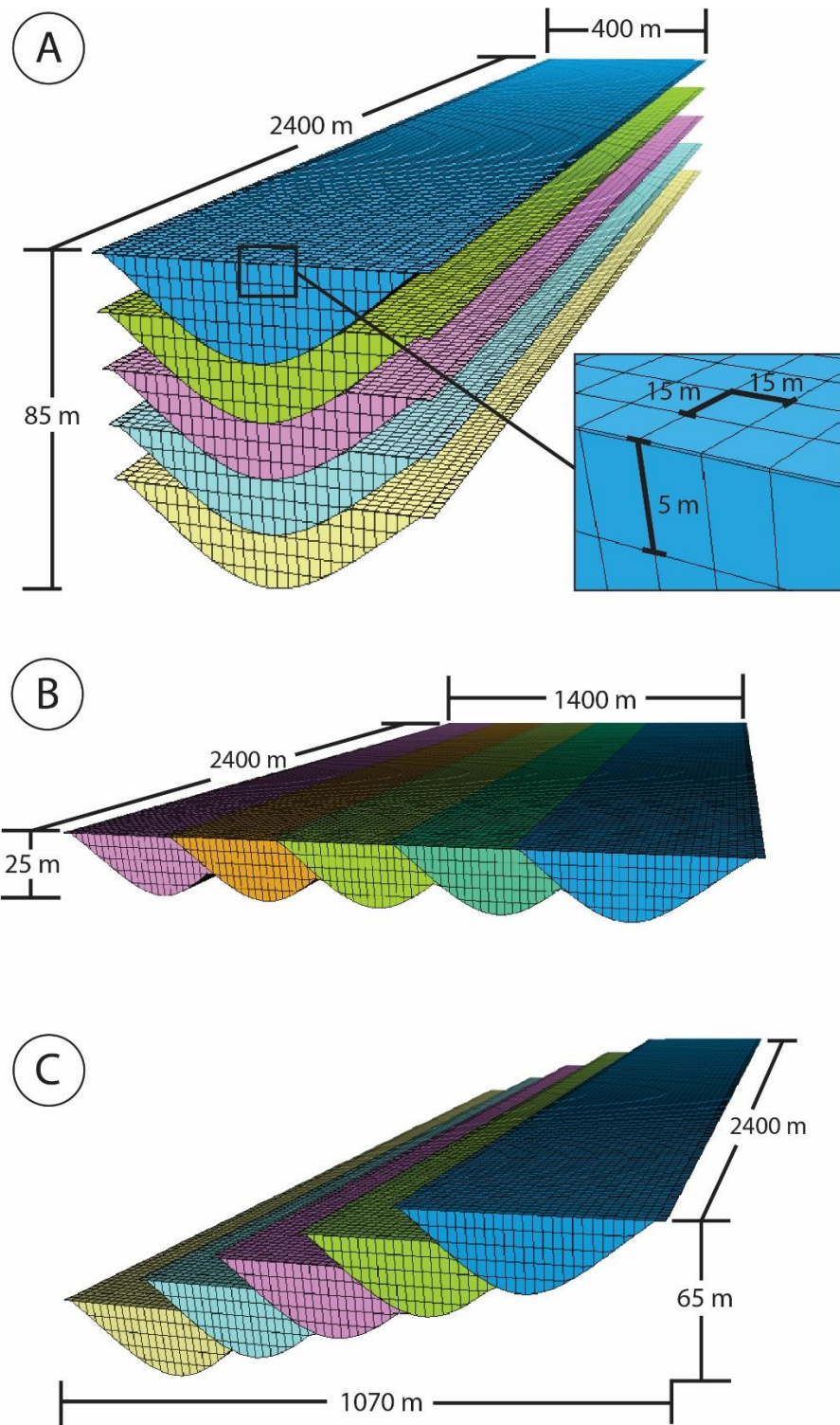


Figure 7. Simple models highlighting model dimensions and gridded cell sizes for (A) vertical, (B) lateral, and (C) diagonal stacking patterns.

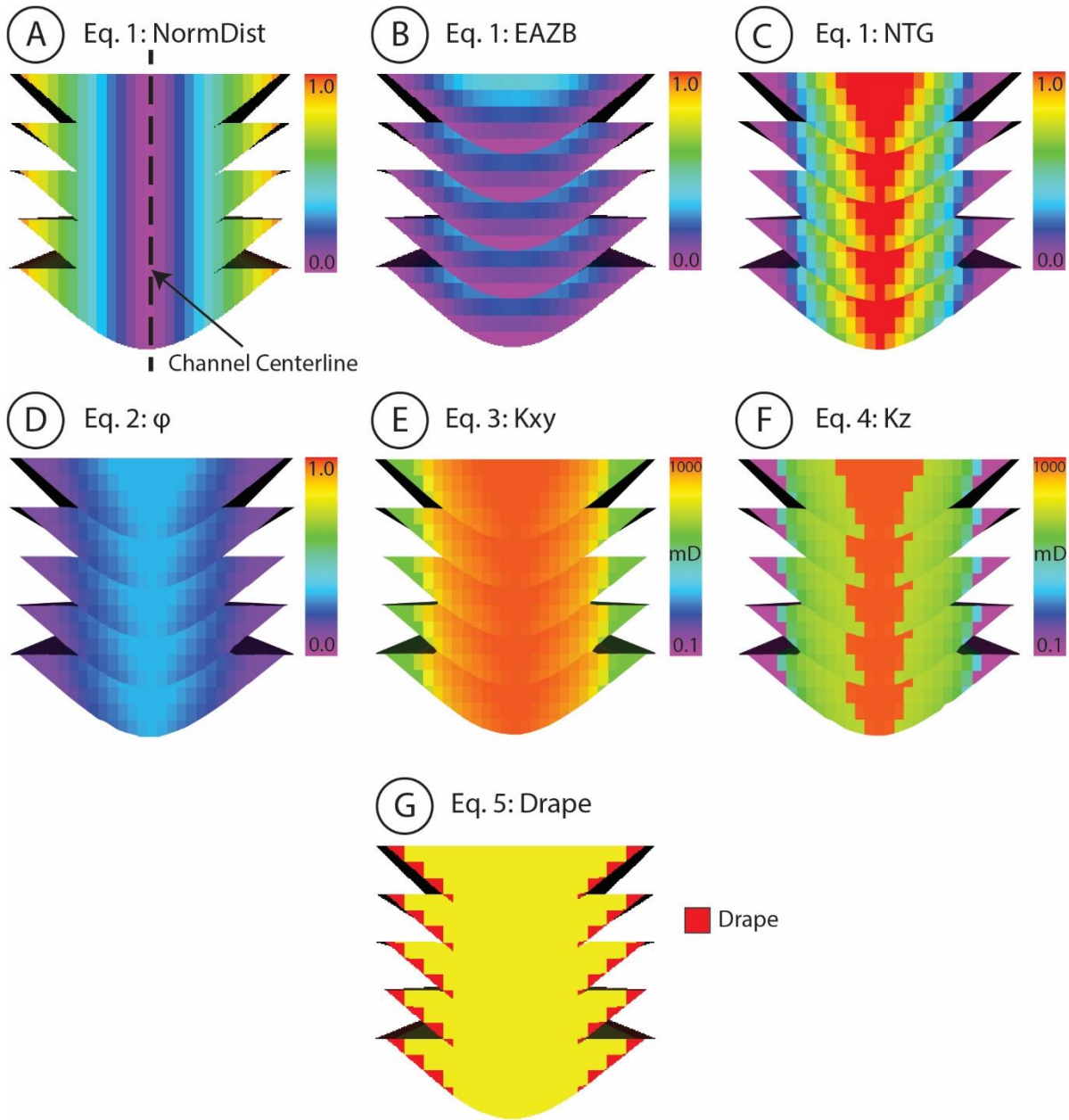


Figure 8. Petrophysical properties of vertically stacked simple models showing: (A) normalized distance from center line ($NormDist$), (B) elevation above zone base ($EAZB$), (C) NTG , (D) porosity (ϕ), (E) horizontal permeability (K_{xy}), (F) vertical permeability (K_z), and (G) $drape$.

4.3.3 Sensitivity Variables

A range of channel-base drape coverage and *NTG* values were tested for each of the three stacking patterns (Table 1, Figures 9, 10, 11). As described in the previous model construction section, *NTG* and *drape* were calculated using equations 1 and 6, respectively, which were manually altered to achieve the desired property values. Full lists of the multiplier values used to create the *NTG* and *drape* property models can be found in Tables 2 and 3. In total, 47 models were created for the simple model sensitivity analysis, though the number of models per stacking pattern varied based on the ranges of *drape* and *NTG* values that still allowed the models to achieve water breakthrough. In the case of the diagonally stacked models, *drape* values above 70% did not allow the simulation to achieve breakthrough, while the laterally stacked models were stymied at *drape* values above 40% and *NTG* values below 50%.

For the drape analysis, a *NTG* value of 100% was maintained for every model, resulting in isotropic, homogenous channel fill with a ϕ value of 0.3, and K_Z/K_{XY} value of 792.5 mD. For the *NTG* analysis, however, ϕ and K_Z/K_{XY} were scaled with the decreasing *NTG* according to equations 2, 3, and 4. Essentially, as *NTG* was lowered, the proportion of channel fill associated with the channel axis was decreased, while the channel margins were expanded. Value ranges and mean values for ϕ , K_Z , and K_{XY} for the vertically stacked models are shown at different *NTG* values in Table 4.

Table 1: Table of sensitivity variable value ranges for vertically, diagonally, and laterally stacked simple models. Models were created at 10% increments within the variable value ranges, including a “base case” model for each stacking pattern with 100% *NTG* and 0% *drape*.

Stacking Pattern	Drape Coverage Range (%)	NTG Range (%)
Vertical	0 - 90	20 - 100
Diagonal	0 - 70	20 - 100
Lateral	0 - 40	50 - 100

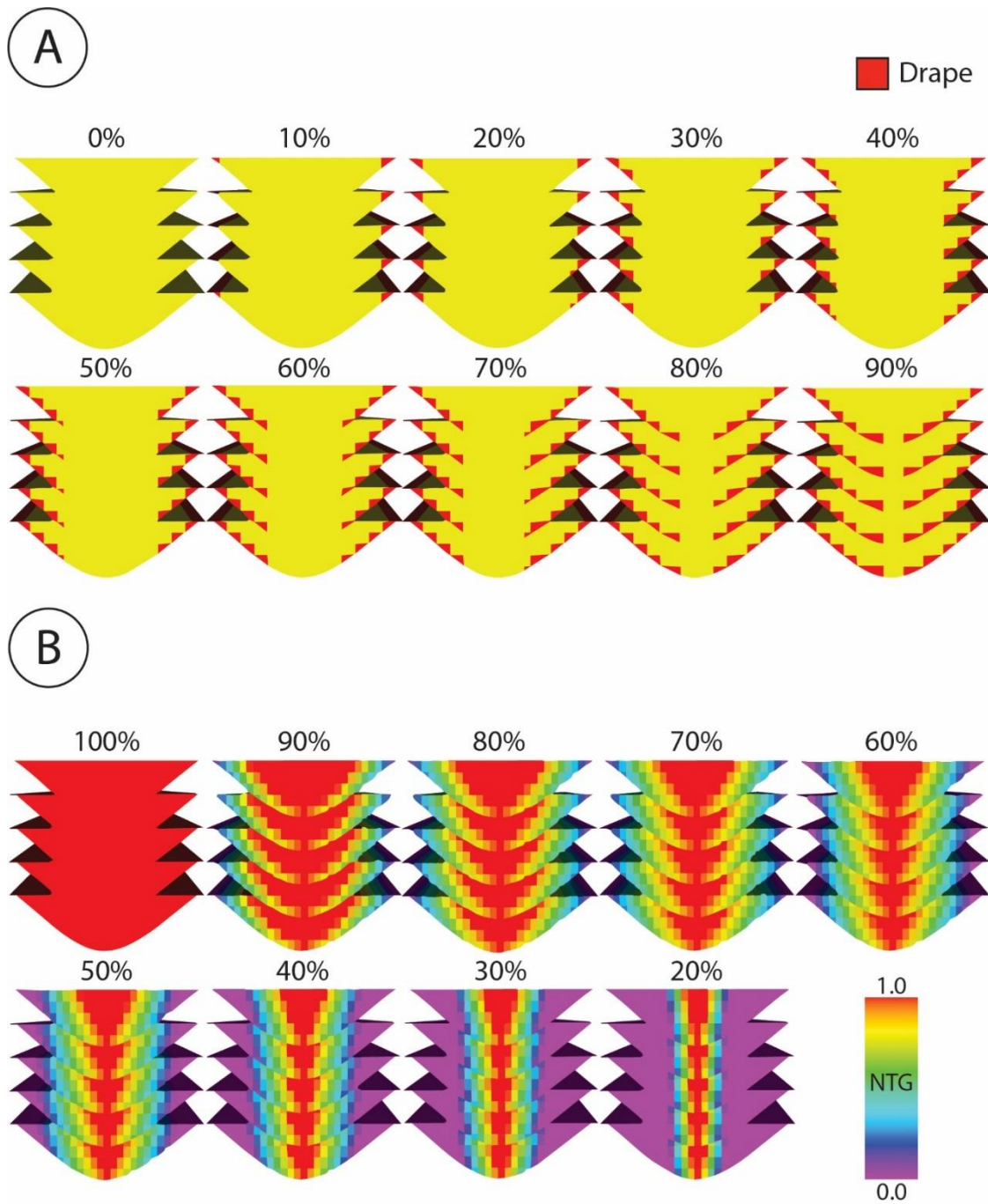


Figure 9. Vertically stacked simple models showing (A) *drape* values ranging from 0-90% and (B) *NTG* values ranging from 20-100%.

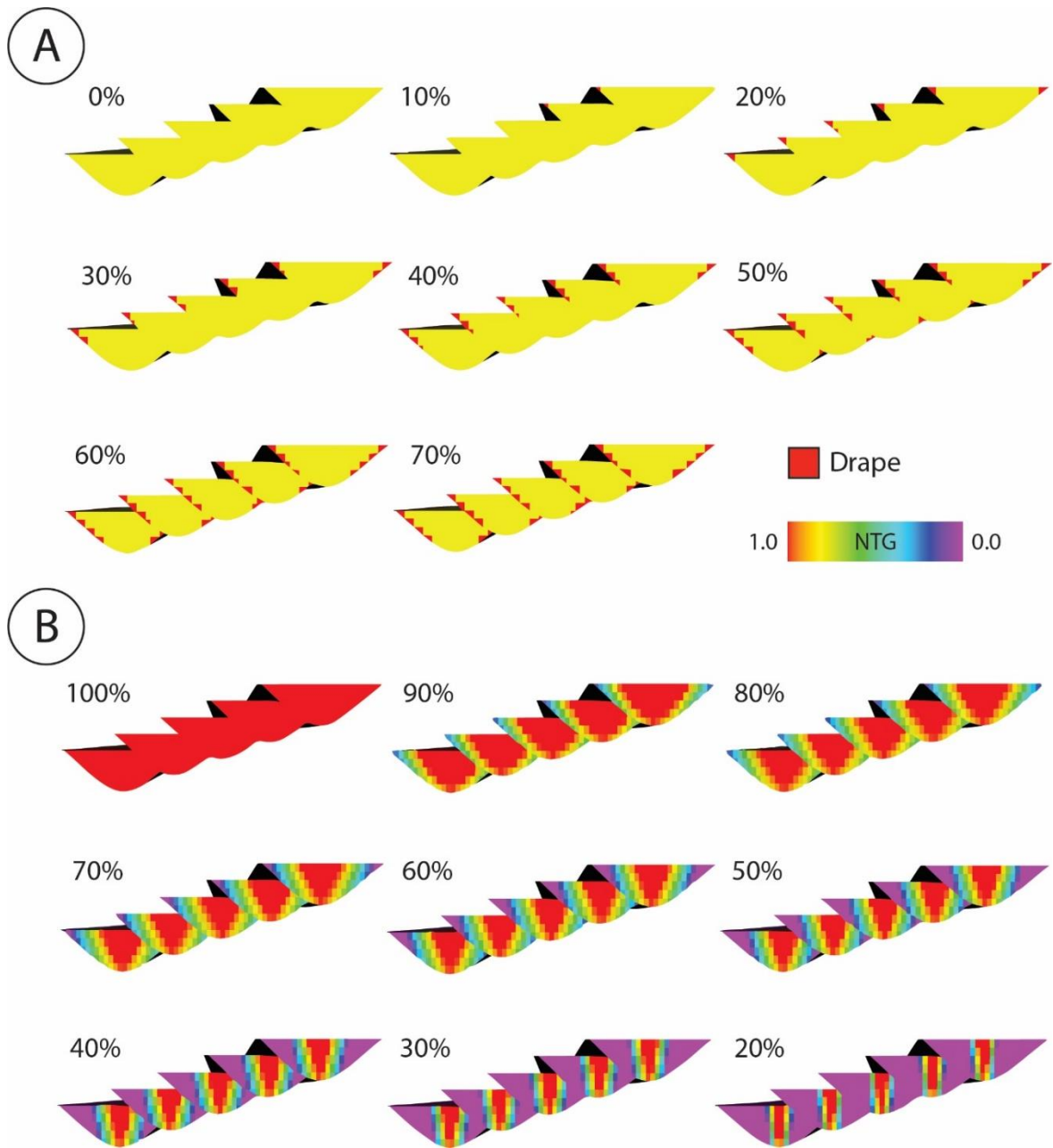


Figure 10. Diagonally stacked simple models showing (A) *drape* values ranging from 0-70% and (B) *NTG* values ranging from 20-100%.

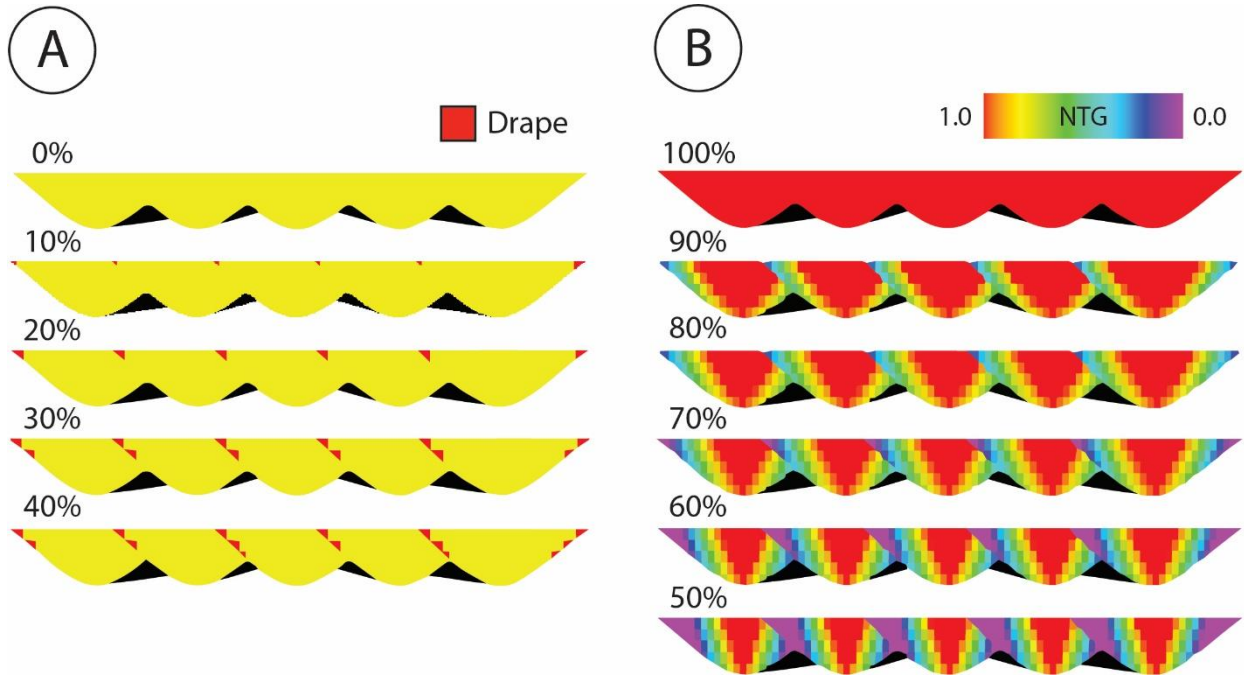


Figure 11. Laterally stacked simple models showing (A) *drape* values ranging from 0-40% and (B) *NTG* values ranging from 50-100%.

Table 2: Table of multiplier values used in Equation 1 [$NTG = (-X * NormDist) + 1 + (EAZB * 0.02)$] to produce the range of *NTG* values used in the simple model sensitivity analysis. Mean *NTG* refers to an average *NTG* value across all channel elements in the model, and does not include zones outside of the channel elements.

Vertical	Mean NTG	0.9	0.8	0.7	0.6	0.5	0.4	0.3	0.2	0.1
	X Value	0.43	0.7	0.95	1.23	1.55	2.05	2.8	4.6	12
Lateral	Mean NTG	0.9	0.8	0.7	0.6	0.5	0.4	0.3	0.2	0.1
	X Value	0.55	0.9	1.27	1.7	2.3	3.2	4.9	8.5	25
Diagonal	Mean NTG	0.9	0.8	0.7	0.6	0.5	0.4	0.3	0.2	0.1
	X Value	0.52	0.89	1.25	1.7	2.25	3.1	4.7	8.1	27

Table 3: Table of multiplier values used in Equation 6 [$Drape = if((NormDist < X)Or(EAZB > 2.5), 1,0)$] to produce the range of drape coverage values used in the simple model sensitivity analysis. “Open Cells” refer to grid cells along the base of a channel element that have a transmissibility multiplier value of 1, and are therefore not draped.

X Value	Open Cells	Total Cells	% Open	% Drape
0.05	3	27	0.11	0.89
0.1	4	27	0.15	0.85
0.15	5	27	0.19	0.81
0.2	7	27	0.26	0.74
0.25	8	27	0.30	0.70
0.3	9	27	0.33	0.67
0.35	11	27	0.41	0.59
0.4	12	27	0.44	0.56
0.45	13	27	0.48	0.52
0.5	15	27	0.56	0.44
0.55	16	27	0.59	0.41
0.6	17	27	0.63	0.37
0.65	19	27	0.70	0.30
0.7	20	27	0.74	0.26
0.75	21	27	0.78	0.22
0.77	22	27	0.81	0.19
0.8	23	27	0.85	0.15
0.85	24	27	0.89	0.11
0.9	25	27	0.93	0.07

Table 4: Ranges and mean values for ϕ , K_{XY} , and K_Z for the vertically stacked NTG analysis. Identical values were used in the diagonally and laterally stacked models, as well as for the deterministic outcrop model NTG analysis.

NTG	ϕ Range	Mean ϕ	K_{XY} Range (mD)	Mean K_{XY} (mD)	K_Z Range (mD)	Mean K_Z (mD)
1	0.30 - 0.30	0.30	792.51 - 792.51	792.51	792.51 - 792.51	792.51
0.9	0.21 - 0.30	0.28	548.86 - 792.51	737.59	54.89 - 792.51	493.79
0.8	0.16 - 0.30	0.26	339.10 - 792.51	678.65	33.91 - 792.51	379.89
0.7	0.11 - 0.30	0.24	68.82 - 792.51	609.81	6.88 - 792.51	305.92
0.6	0.10 - 0.30	0.22	0.03 - 792.51	525.08	0.003 - 792.51	238.28
0.5	0.10 - 0.30	0.20	0.03 - 792.51	445.64	0.003 - 792.51	203.64
0.4	0.10 - 0.30	0.18	0.03 - 792.51	354.25	0.003 - 792.51	171.07
0.3	0.10 - 0.30	0.16	0.03 - 792.51	269.94	0.003 - 792.51	133.43
0.2	0.10 - 0.30	0.14	0.03 - 792.51	177.82	0.003 - 792.51	93.65

4.3.4 Flow Simulation

Two-phase flow simulations were performed using Schlumberger's ECLIPSE reservoir simulator (*SimLauncher Version 2016.2.0.0*). In each simulation case, the reservoir was above the oil water contact, initially contained a water saturation value of 0.12, and had an initial reservoir pressure of 4800 psi. Water enters the system via a constant flux aquifer situated at the base of the model. Three evenly-spaced production wells penetrate the top layer of the top channel element in each stacking pattern, set at a constant liquid pumping rate of 2500 barrels of fluid per day. When the producing wells were unable to produce oil at the prescribed rate, such as in high drape cases, the wells switch to bottom-hole pressure control. Aquifer influx and well liquid rates were held constant throughout the simulation, regardless of the impact on reservoir pressure in order to compare across models. Simulation results, including cumulative oil volume, reservoir pressure, and water cut, were recorded at 10 day intervals. The simulations ran at least until water breakthrough was achieved, or until it became clear that the flow paths were obstructed to the point of being unable to achieve breakthrough.

Fluid flow was restricted to the channel elements and any other internal architectural features, such as MTDs in the deterministic and stochastic modeling setups. All "background" zones, i.e. zones outside of the channel elements and MTDs, were designated as no-flow boundaries, either through the use of a transmissibility multiplier with a value of 0 or by assigning them porosity and permeability values of 0. Flow simulation setups are shown in Figure 12, with examples of completed flow simulations shown in Figure 13.

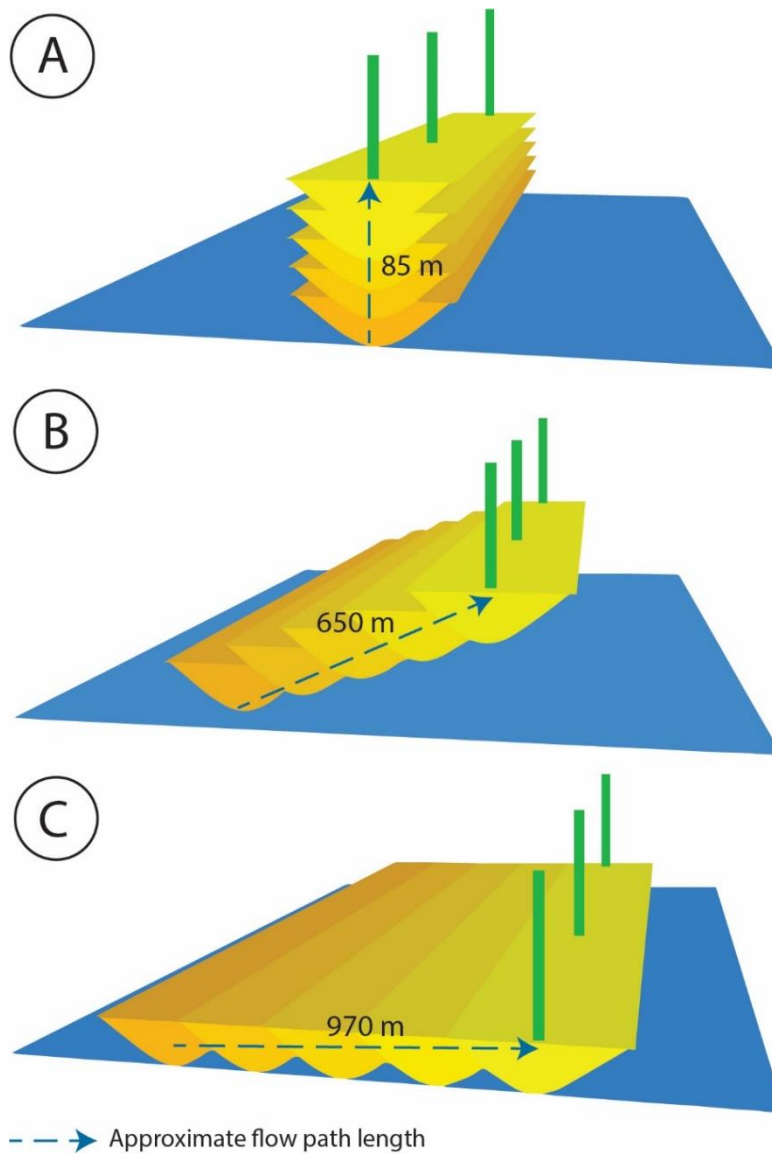


Figure 12. Flow simulation setup for simple model analysis of (A) vertically, (B) diagonally, and (C) laterally stacked channel elements. A constant flux aquifer inputs water at the base of the model, while three evenly-spaced producing wells draw from the uppermost/most distant channel element. In the laterally stacked case (C), water only entered the reservoir through the leftmost channel element. Approximate flow path lengths are annotated.

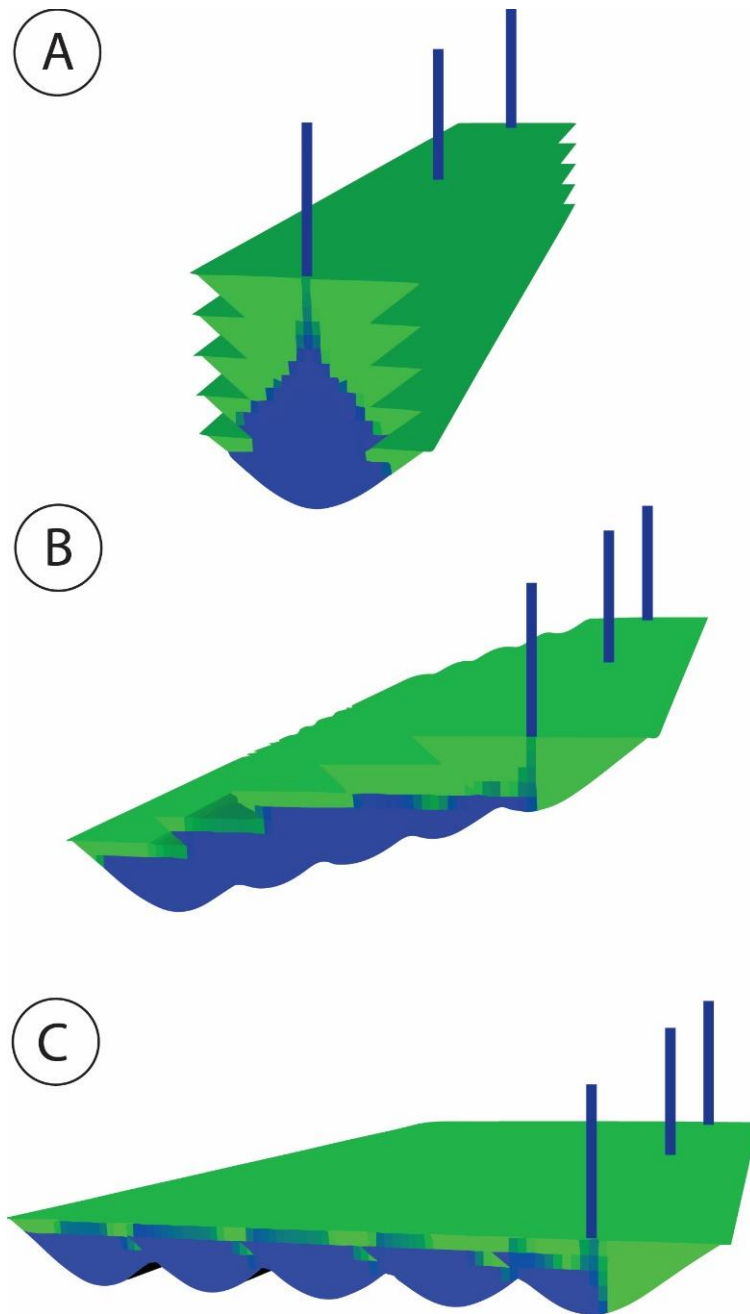


Figure 13. Example flow simulations of high net to gross, low drape coverage models for simple models stacked (A) vertically, (B) diagonally, and (C) laterally. Green cells have been bypassed and are oil saturated, while blue cells have been displaced with water.

4.3.5 Simple Model Results

4.3.5.1 Drape Results

Simulation results for drape coverage are expressed in terms of water breakthrough time (*BT*) (Fig. 14A), recovery efficiency (*RE*) (Fig. 14B, 14C), and cumulative oil produced at 0.1 pore volumes injected (*CUMoil @ 0.1 PVI*) (Fig. 14D). Due to the different geometries of the three stacking patterns, there is a clear difference in the amount of time it takes for water to travel between the aquifer and producing wells. The most rapid water breakthrough is in the vertical series (Fig. 14A, blue series), while the lateral stacking pattern accounted for the longest water breakthrough times (Fig. 14A, gray series). This aligns with the distance that the water must travel between the aquifer and the producing wells, which is much shorter in the vertical case than the lateral case (~85 m compared to ~970 m, Fig. 12). The constant pumping rates result in this discrepancy directly translating to *RE*, and thus two plots are provided: one for the unmodified *RE* values that directly reflect *BT* (Fig. 14B), and one plot where results are normalized relative to the “base case” of each stacking pattern, i.e. 100% *NTG* and 0% *drape* (Fig. 14C).

This normalized *RE* plot helps to illuminate some differences in flow behaviors between the three stacking patterns. Breakthrough was able to be achieved through 90% drape coverage in the vertical case, but a closure of the flow pathway only allows breakthrough through 70% and 40% of drape coverage in the diagonal and lateral cases, respectively (Fig. 14). For the vertical stacking pattern, there is a linear decrease in *RE* (related to a decrease in *BT*) beyond 40% drape coverage. A similar trend is seen for the diagonal and lateral stacking patterns, with the exception of the highest *drape* case for each. At these higher *drape* values, *BT* increases slightly before the flow pathways are completely obstructed at any additional *drape* increase.

While increasing *drape* leads to a quicker water breakthrough, this trend is not reflected when looking at *CUMoil @ 0.1 PVI* (Fig. 14D). Production trends remain completely flat for the lateral and diagonal stacks, and through 70% drape coverage in the vertical case. This shows that despite a quicker *BT* and lower *RE* with increasing drape coverage, the ability of the wells to produce the prescribed volumes is not inhibited (with the exception of 70%+ drape in the vertical case). Additionally, the laterally stacked series produces more oil at 0.1 PVI than the vertical and diagonal series, which may be related to the more horizontal nature of the flow pathways.

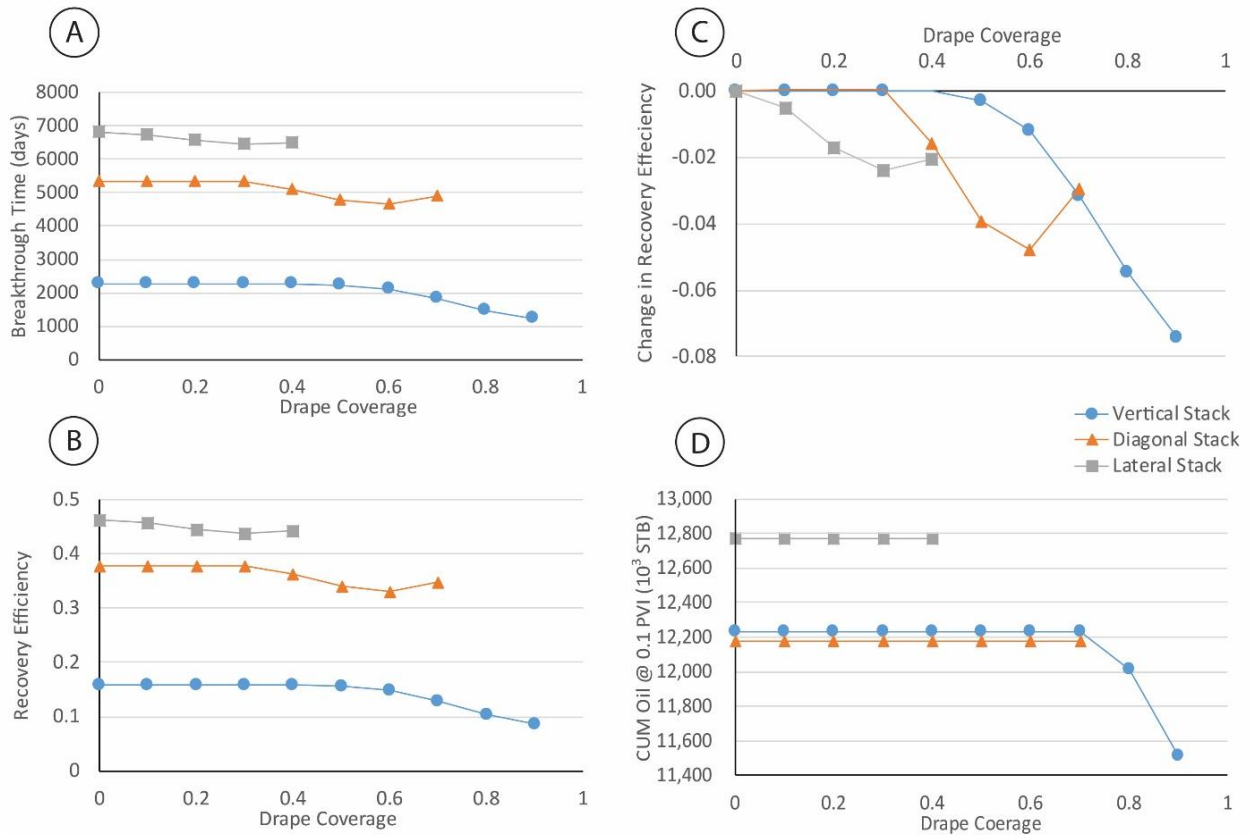


Figure 14. Simulation results of sensitivity analysis for channel base drape coverage for vertically, diagonally, and laterally stacked simple models. (A) *BT* versus *drape*. (B) *RE* versus *drape*. (C) *RE* normalized to a 0% *drape* base case versus *drape*. (D) *CUMoil @ 0.1 PVI* versus *drape*.

4.3.5.2 NTG Results

Simulation results for decreasing *NTG* have some similarities to those observed for increasing *drape* with some key differences (Fig. 15). A similar trend of decreasing breakthrough time with decreasing *NTG* is observed, with the lateral and diagonal series showing a reversal in the trend at low *NTG* values (Fig. 15A). Unlike with the *drape* results however, the trend for recovery efficiency does not directly mirror the breakthrough times (Fig. 15B). This is because as *NTG* decreases, the original oil in place values also decrease, largely offsetting the drop in breakthrough time and resulting in flatter curves.

The normalized *RE* results are more illuminating when paired with the *CUMoil @ 0.1 PVI* results (Fig. 15C, 15D). For both the diagonal and lateral stacking patterns, once *NTG* drops below a certain threshold (0.6 for lateral, 0.5 for diagonal), there is a precipitous drop-off in the ability of the producing wells to maintain their prescribed liquid rates. The tortuosity of the flow paths, created by the low-net channel margins, restricts fluid flow enough that despite an increase in breakthrough times, the actual oil production is considerably lower and results in a sharp drop-off in recovery efficiency. The trend for the vertical stacking pattern has a more constant decline, as the clear flow path through the channel axes allows the producing wells to better maintain their production even at very low *NTG* values.

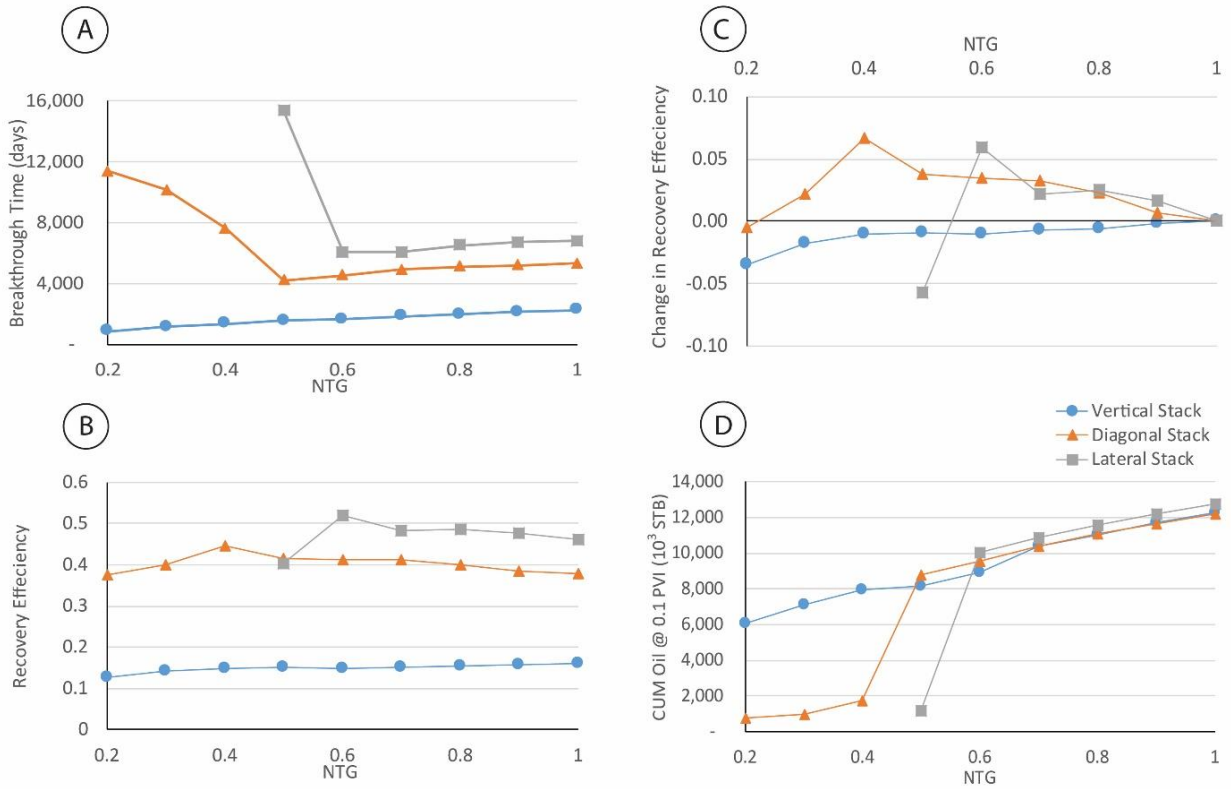


Figure 15. Scatter plots of net to gross ratio simulation results for vertically, diagonally, and laterally stacked simple models. (A) *BT* versus *NTG*. (B) *RE* versus *NTG*. (C) *RE* normalized to a 100% *NTG* base case versus *NTG*. (D) *CUMoil* @ 0.1 *PVI* versus *NTG*.

4.4 Deterministic Outcrop Model

4.4.1 Description of Deterministic Model Analysis

The second sensitivity analysis uses a deterministic outcrop model to evaluate flow behaviors associated with various architectural elements, including complex stacking patterns and mass transport deposits. The model framework utilizes field data and working interpretations to create a more realistic approximation of a deep-water channelized system, with the intention of acting as the “ground truth” model in this three-part sensitivity analysis. Simplifying the internal channel element fill then allows for the systematic variation of net to gross ratio, drupe coverage, and MTD properties. This stage of the analysis builds upon the simplified models, as the deterministic model is in essence a combination of vertically, diagonally, and laterally stacked channel elements with the added complexity of mass transport deposits.

4.4.2 Model Construction

The existing measured section data and planforms interpreted from paleoflow measurements provided the foundation for 3D reconstruction from the Laguna Figueroa outcrop. The planforms were used as a basis for the sinuous geometries of the channel elements in the model. The original planform interpretations shown in Figures 4 and 5 of the *Study Area: Laguna Figueroa Outcrop* section of this thesis range from roughly 200-500 m wide, but the decision was made to simplify the model by standardizing channel widths to 400 m. The Lower Pink complex/element was the exception, and was modeled with a wider (800 m) geometry, as this complex has been interpreted as a single laterally amalgamated, mostly homogeneous sandstone body (working interpretation from Dr. Steven Hubbard) (Fig. 3B, “Lower Pink”). Based on statistics from measured sections, each channel element was created with a standard 25 m thickness

before erosion by overlying channel elements. This study does not delve into asymmetry, and therefore each element was created to be symmetric across its centerline.

4.4.2.1 Model Framework

Construction of the outcrop model was surface-based, and relied on a hierarchical layer ordering of channel element top and base surfaces, channel complex surfaces that enclose 2-5 grouped channel elements, and channel complex set surfaces grouping channel complexes (Figures 1, 17, 18 and 19; Sprague et al. 2002, 2005). In all, 49 separate surfaces were utilized to build the model framework, which was based on the conceptual model shown in Figure 16A. Some concessions had to be made to facilitate successful flow simulation, including reducing the spacing between the upper and lower complex sets to allow fluid flow between the two sections of reservoir. This resulted in a reduction of overall thickness of the outcrop model from the 300 m seen in Figure 16A to the roughly 265 m seen in Figure 16B. Additionally, the final model was created flat as opposed to honoring the roughly 15-degree dip of the actual outcrop (from field measurements), and does not directly align with GPS-anchored measured section data. This was done due to the unrealistic channel element geometries that were created when attempts were made to incorporate the measured section data.

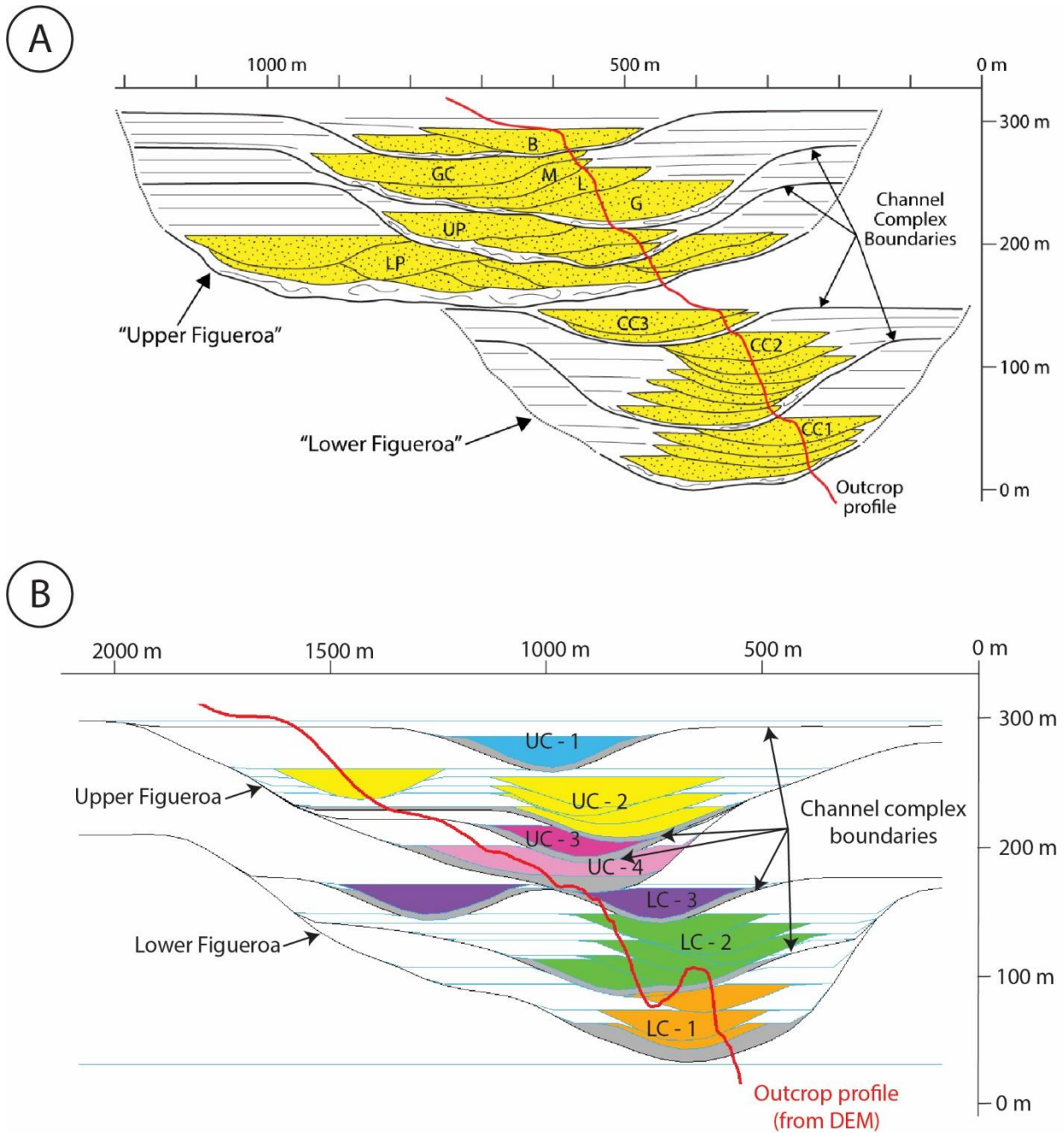


Figure 16. (A) Conceptual model of Upper and Lower Laguna Figueroa outcrop showing hierarchical architecture, including channel complex boundary surfaces. Modified from Macauley and Hubbard (2013) and Covault et al. (2016). This interpretation uses a different number of channel elements, but maintains a similar overall hierarchy. Outcrop profile is marked with a red line. (B) Intersection along southern edge of the deterministic model used in this study, with channel elements color-coded according to channel complex. Outcrop profile derived from a digital elevation map (DEM) marked with a red line.

The process for creating channel element surfaces was the same as that described in Chapter 1: Simple Models, which utilized three depth-shifted channel polylines and a built-in minimum curvature surface generation algorithm (Fig.17). The primary difference is simply that elements in the deterministic model were created using the interpreted channel planforms, which contain more sinuosity than the idealized straight elements of the simple models.

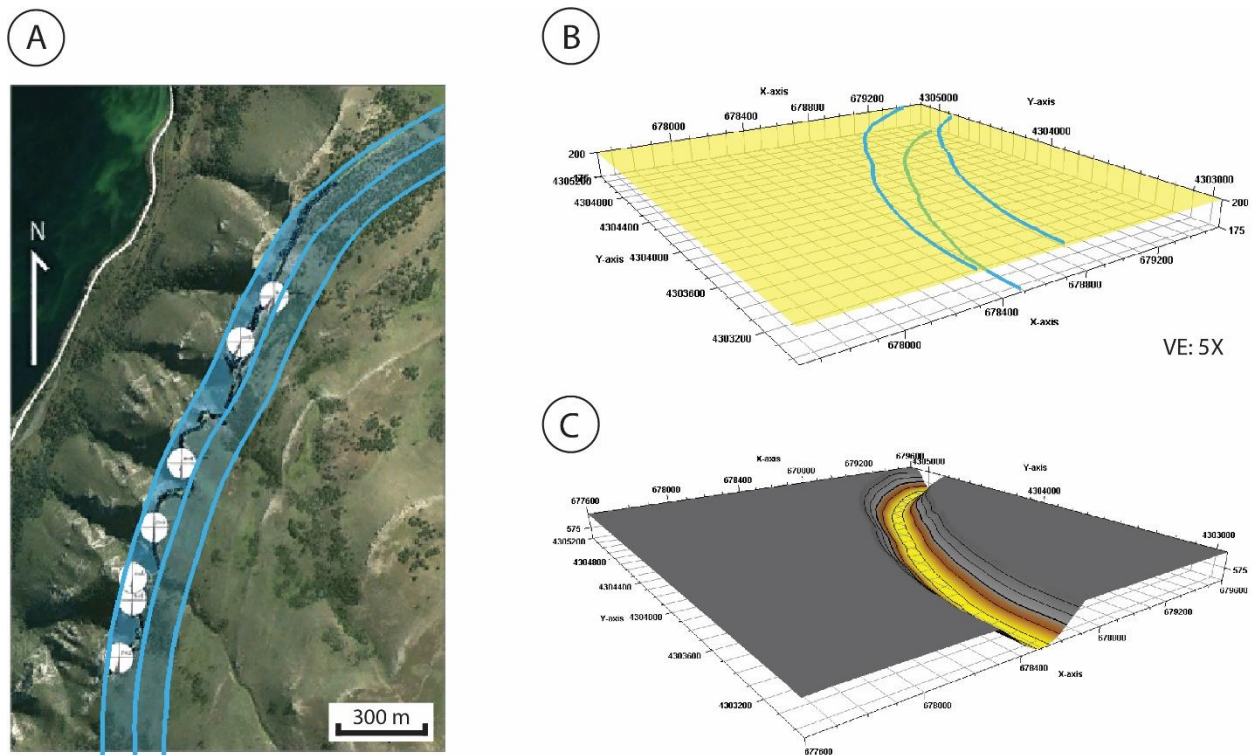


Figure 17. (A) Satellite image of Laguna Figueroa outcrop with Blue channel element interpreted. (B) Flat surface and channel polylines used as inputs for generating a channel element surface. (C) Final channel element surface for the Blue channel element.

Complex and complex set surfaces were created to bound the channel elements and allow for the introduction of mass transport deposits. The upper and lower complex set surfaces were generated utilizing channel polylines from the various elements contained within them, and then manually smoothed and adjusted to better fit the confined channels (Fig. 18). Channel complex

surfaces were generated by depth shifting and smoothing copies of the existing channel element surfaces (Fig. 19). Both complex and complex set surfaces are designed as base surfaces in the gridding process, resulting in all overlying surfaces truncating against them. In this manner, these confining surfaces are able to properly contain the channel elements and MTDs found within.

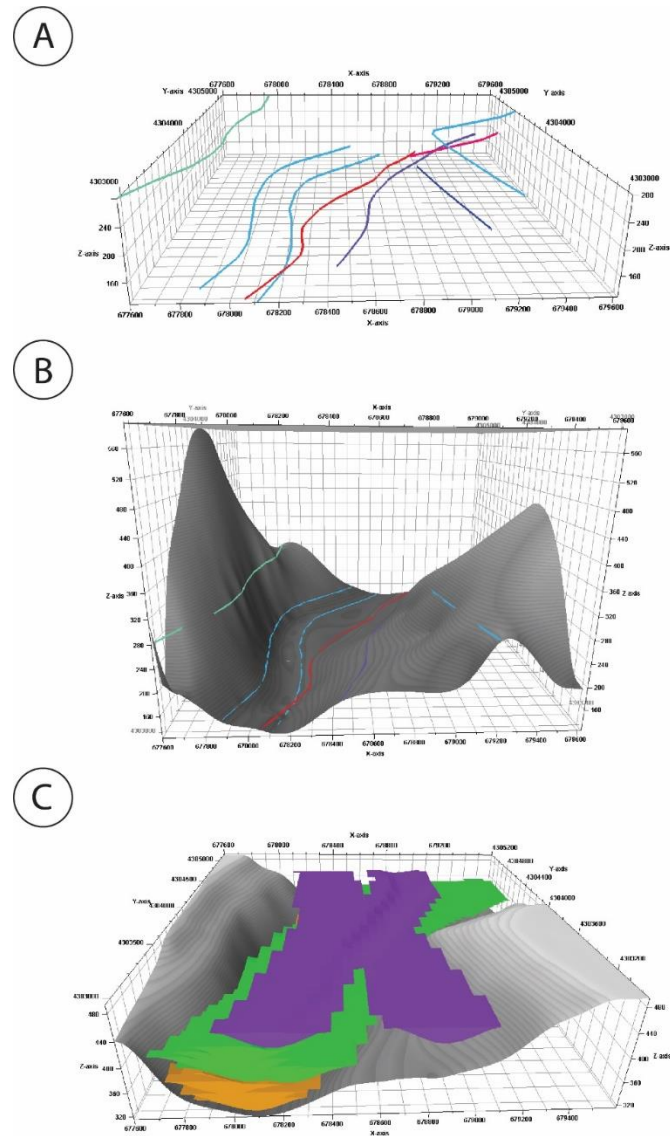


Figure 18. Constructional phases of the Lower Channel Complex Set surface. (A) Depth-shifted channel element polylines are selected as the framework of the complex set surface. (B) Minimum curvature gridding is used to generate the surface. (C) The complex set surface is trimmed, smoothed, and manually manipulated to ensure it contains all relevant channel elements. Lower Figueroa channel elements are shown within the complex set surface, color-coded by channel complex.

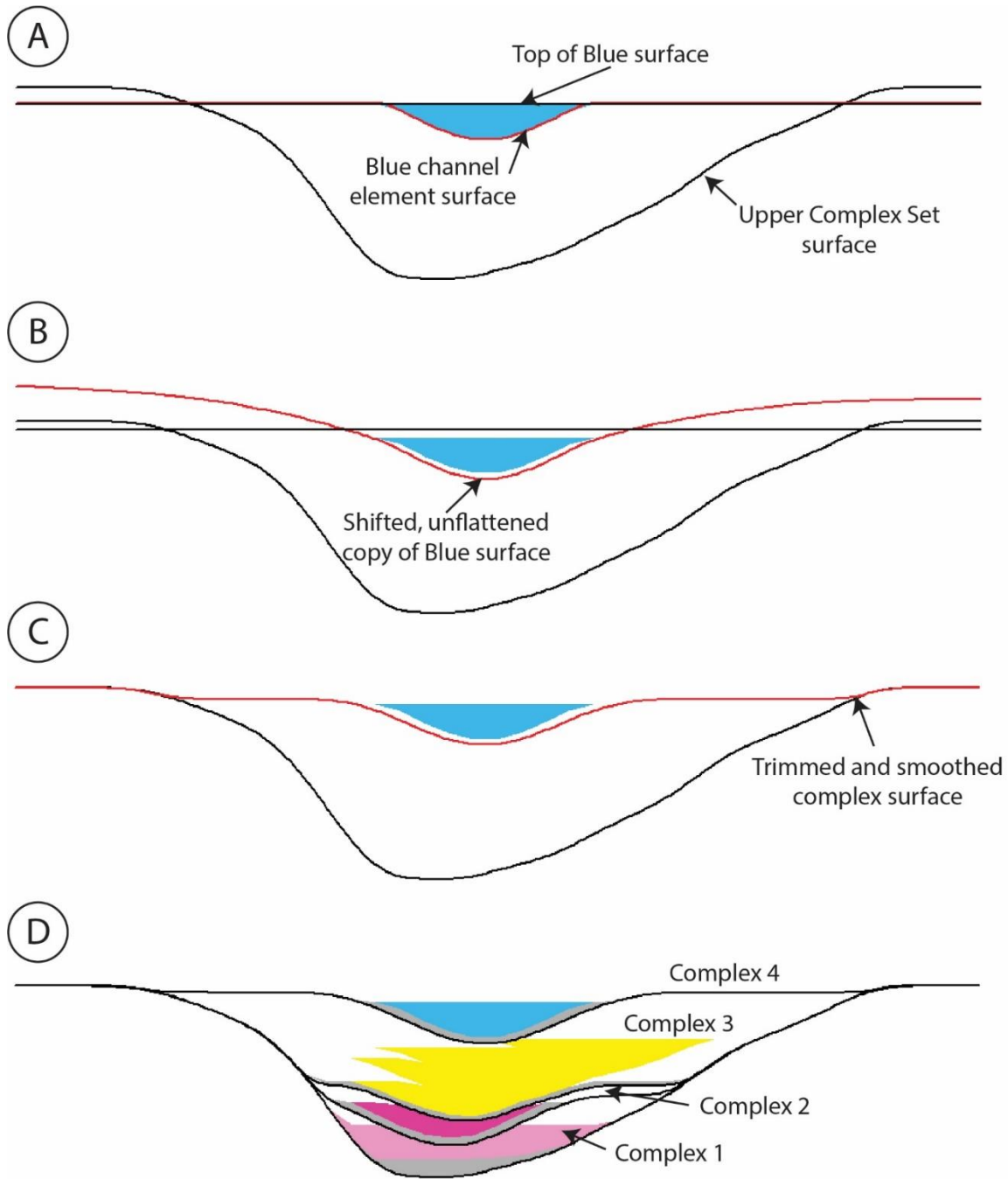


Figure 19. Phases of constructing a channel complex surfaces and overlying MTD. (A) Replicate the channel element surface of the lowest (oldest) element in the complex. (B) Use minimum curvature to extrapolate the edges of the complex, and manually shift the complex surface. (C) Use surface calculations to constrain the complex surface within the complex set surface. (D) Iterate using surface calculations and smoothing to reach the desired final surface.

A built-in simple, surface-based grid was created using a 50 m x 50 m x 2.5 m cell size. Previous iterations of the model used a finer mesh, but the resulting models contained an excessively large amount of cells that increased flow simulation time. Using the 50 m grid increment, the final model measures 2250 m x 2000 m x 265 m (I x J x K), with 1,038,600 total grid cells (Figure 20). While some finer detail is obviously lost by using a coarser grid increment, this resolution strikes a balance between being able to capture heterogeneity and being able to efficiently flow simulate the model.

This coarse grid increment differs from that used in the simple model analysis (15 m x 15 m x 5 m), which could have an impact when comparing final flow simulation results. The different cell sizes could potentially change the flow paths that fluids will take between aquifer and producing wells, ultimately impacting water breakthrough times.

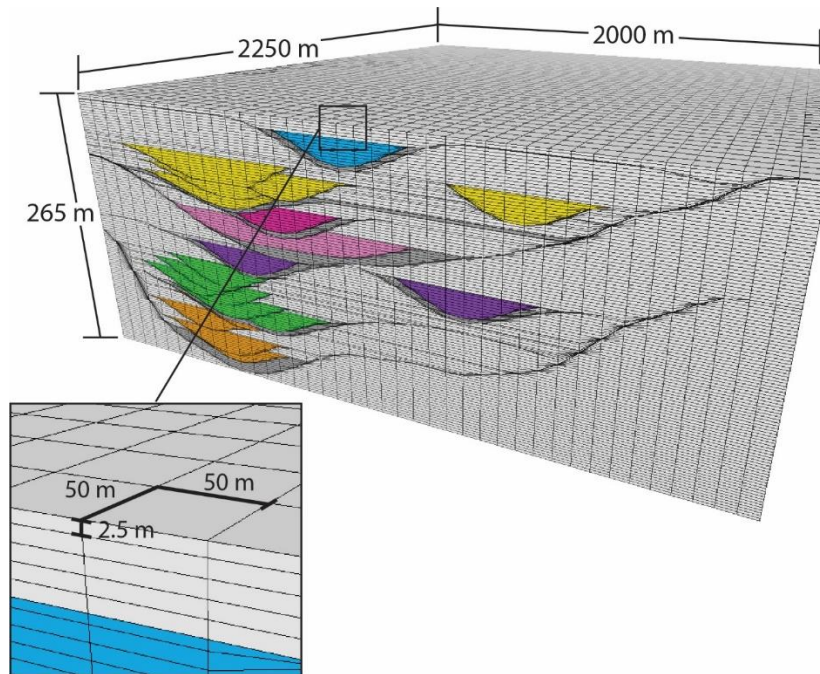


Figure 20. Full deterministic model showing model dimensions with inset showing grid cell size. Channel elements are color coded according to channel complex, with MTDs shown in gray at the base of each complex.

4.4.2.2 Property Modeling

The process used to generate petrophysical properties was the same as that used in *Chapter 1: Simple Models*, which utilized geometrical trend modeling to calculate *NTG* (Fig. 21C), which was then used to calculate φ (Fig. 21D), K_{xy} (Fig. 21F), and K_z (Fig. 21E). The deterministic model, however, includes the addition of a *facies* property (Fig. 21B), generated using Equation 6.

$$Facies = if(NTG = U, 0, if(NTG > 0.9, 1, if(NTG > 0.4, 2, 4))) \quad (6)$$

Five total facies were used, which were described in the *Study Area: Laguna Figueroa* section of this thesis. F1 – F3 constitute channel fill, and were calculated using the *NTG* cutoffs shown in Equation 6. MTD facies were simply assigned to the zones (Fig. 21A) between the complex surfaces and the bottommost channel element within each complex. Cells outside of the channel elements and MTDs contain an unassigned *NTG* value, and are therefore calculated as “background” facies that contains no storage or flow properties.

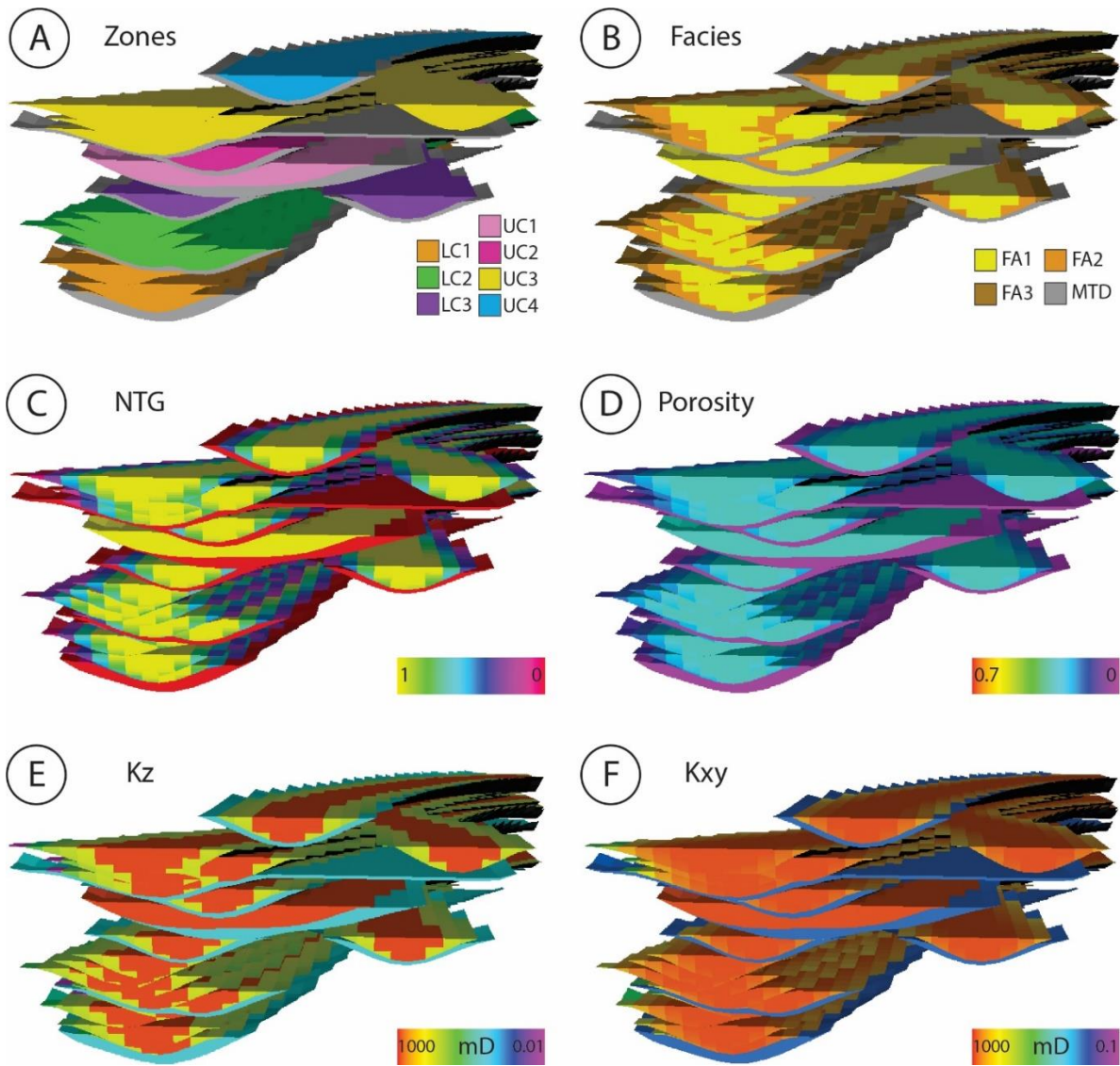


Figure 21. (A) *Zones*, color coded according to channel complex. MTDs are shown in gray at the base of each complex. (B) *Facies*. (C) *NTG*. MTDs are shown in red and assigned 0% *NTG*. (D) Porosity (ϕ). (E) Vertical permeability (K_z) (F) Horizontal permeability (K_{xy}).

4.4.3 Sensitivity Variables

Part two of the three-part sensitivity analysis uses the deterministic outcrop model to test the impacts of channel base drupe net to gross ratio, and the added hierarchical variable of the permeability of MTD facies on fluid flow. The three sensitivity variables, with their ranges of values listed in Table 5 and displayed in Figures 22, 23, and 24, were each tested independently, with two variables remaining constant while one is tested. For the MTD permeability analysis, values are chosen on a logarithmic scale, with K_{xy} being equal to 10 times K_z in each case (Table 7). Additionally, MTDs were assigned a porosity value of 0.01 for all permeability cases.

Table 5: Table of sensitivity variable value ranges for the deterministic model analysis. Models were created at 10% increments within the variable value ranges.

Sensitivity Variable	Range
Drape Coverage	0-90%
NTG	20-100%
MTD Kz	0.001-1000 mD

Drape was calculated in a similar manner to that seen in the simple model analysis (Equation 5, Table 3), and MTD permeability values (Table 7) were simply assigned to all zones containing MTD facies. *NTG* for the deterministic models utilized a new equation to account for the amalgamated nature of the Lower Pink complex in the Upper Figueroa.

$$NTG_x = if(Zones_hierarchy = 18, X, ((-Y * NormDist) + 1 + (EAZB * 0.02))) \quad (7)$$

Equation 7 was used to calculate a mean *NTG* value for the model, where X refers to the target *NTG* value (e.g. 0.6) and Y refers to the multiplier used with the *NormDist* property. The Lower Pink complex coincides with *Zone* number 18, which was assigned the target average *NTG* value.

A full table of inputs for Equation 7 are shown in Table 6, along with the calculated mean *NTG* values for each model.

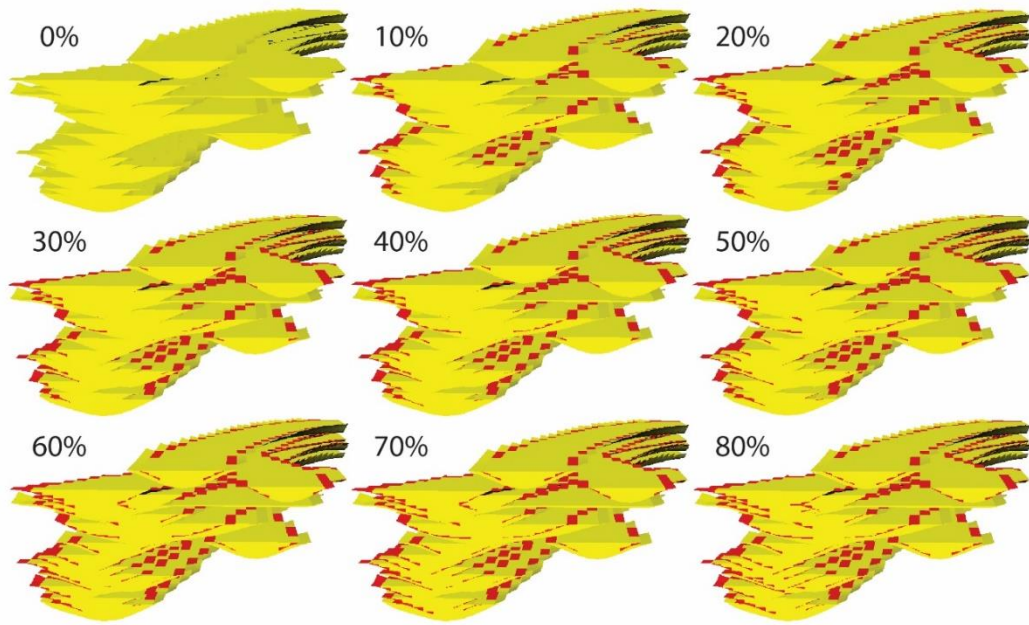
Table 6. Table of multiplier values used in Equation 7 $NTG_x = if(Zones_hierarchy = 18, X, ((-Y * NormDist) + 1 + (EAZB * 0.02)))$ to produce the range of average *NTG* values used in the deterministic model sensitivity analysis. *Zones_hierarchy = 18* refers to the Lower Pink channel complex.

Target NTG	X Value	Y Value	Calculated Mean NTG
0.9	0.9	0.95	0.901
0.8	0.8	1.67	0.801
0.7	0.7	2.39	0.701
0.6	0.6	3.25	0.604
0.5	0.5	4.6	0.500
0.4	0.4	6.7	0.402
0.3	0.3	10.9	0.301
0.2	0.2	20.5	0.203

Table 7. Table of MTD K_{xy} , K_z , and ϕ values for the deterministic model sensitivity analysis.

K_{xy} (mD)	K_z (mD)	ϕ
0.01	0.001	0.01
0.05	0.005	0.01
0.1	0.01	0.01
0.2	0.02	0.01
0.5	0.05	0.01
1	0.1	0.01
10	1	0.01
100	10	0.01
1000	100	0.01
10000	1000	0.01

(A)



(B)

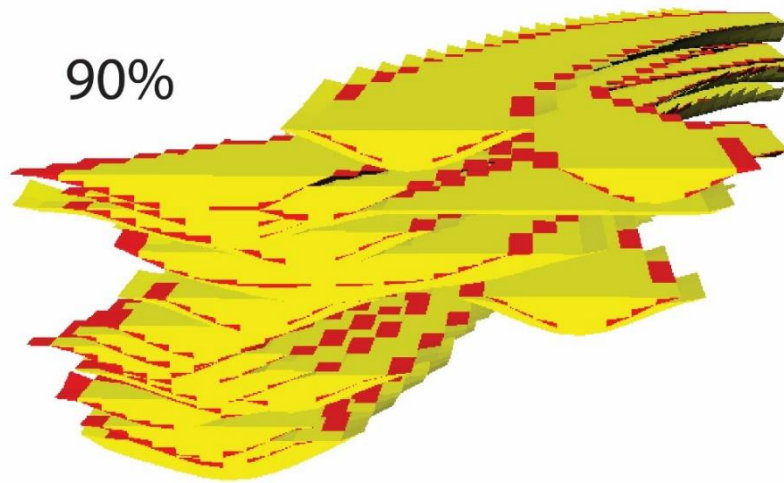


Figure 22. (A) Deterministic models showing *drape* values ranging from 0% to 80%. (B) Close-up of deterministic model with 90% *drape*. Draped cells are colored red and act as flow barriers.

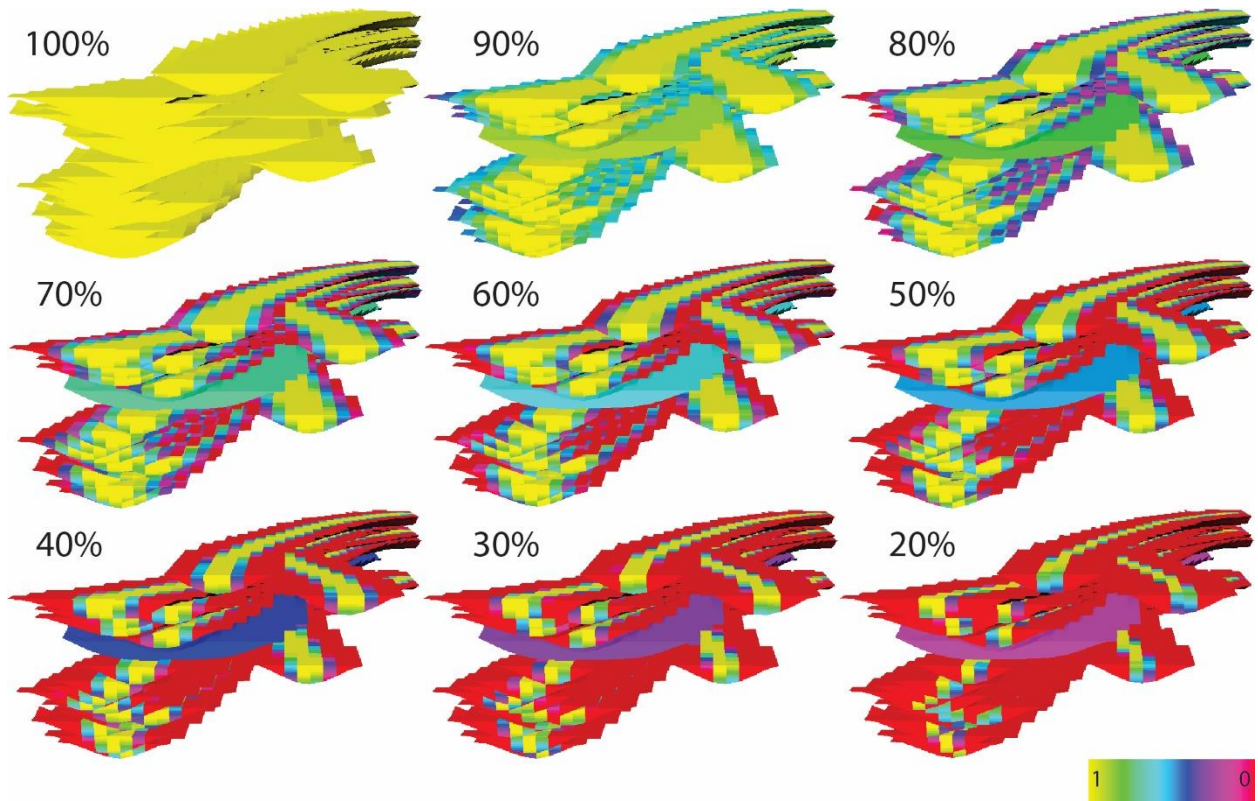


Figure 23. Deterministic models showing average *NTG* values ranging from 100% to 20%. The Lower Pink channel element/complex is assigned the average value of each model.

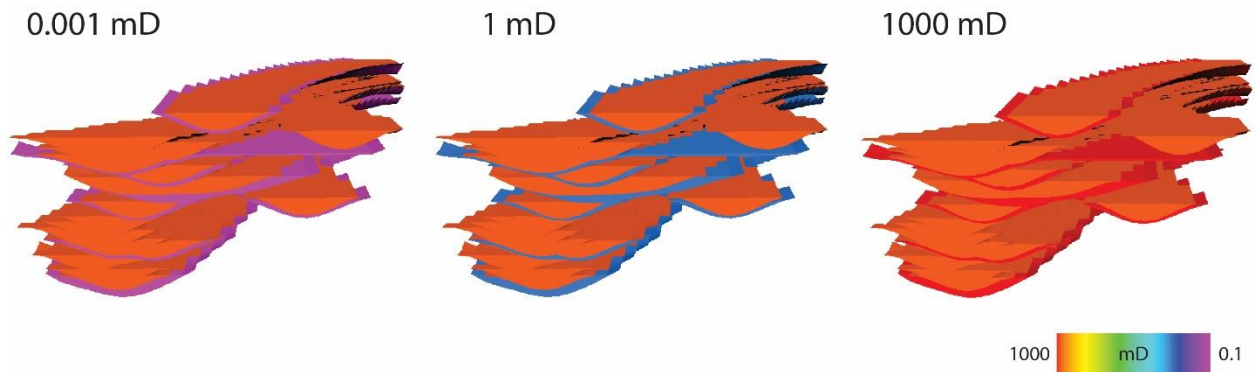


Figure 24. Deterministic model with K_z property displayed. MTDs are shown with permeabilities of 0.001, 1, and 1000 mD.

4.4.4 Flow Simulation

The flow simulation setup is much the same as for the simple model analysis, with a constant flux aquifer connected to the lowermost channel element and three producing wells drawing from the top layer of the uppermost channel element (Fig. 25). Again, fluid flow was restricted to the channel elements and MTDs, with all background zones being designated as no-flow. The pumping rate for each well was set at a constant liquid rate of 5000 barrels per day. When the producing wells were unable to produce at the prescribed rate, such as in low permeability cases, the wells would switch to bottom hole pressure control. Aquifer influx and well liquid rates were held constant for all models in the deterministic study, regardless of the impact on reservoir pressure.

Model run times were continually adjusted based on *drape*, *NTG*, and MTD K_z values, as the water breakthrough times ranged from 2370 days for the 20% *NTG* model to 30,900 days for the 0.001 mD MTD K_z model. A sampling of the flow simulation results for each of the sensitivity variables at water breakthrough time is shown in Figure 26.

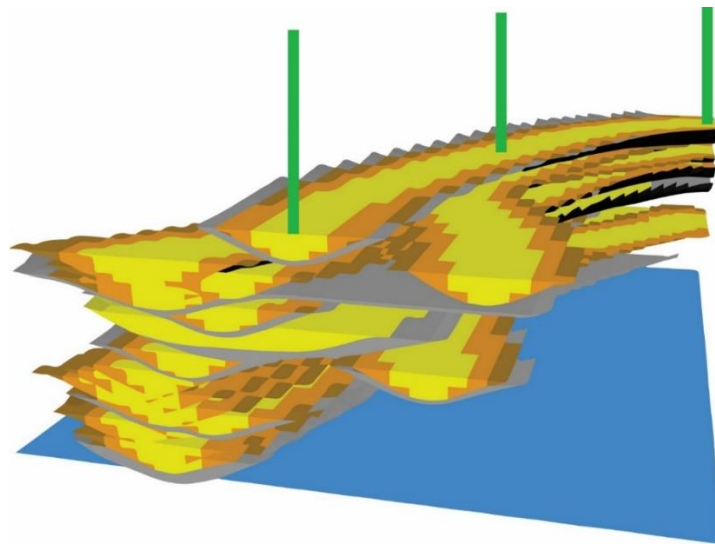


Figure 25. Flow simulation setup for deterministic model analysis. A constant flux aquifer inputs water at the base of the model, while three evenly-spaced producing wells draw from the uppermost channel element. Property shown is facies, with MTD facies colored gray.

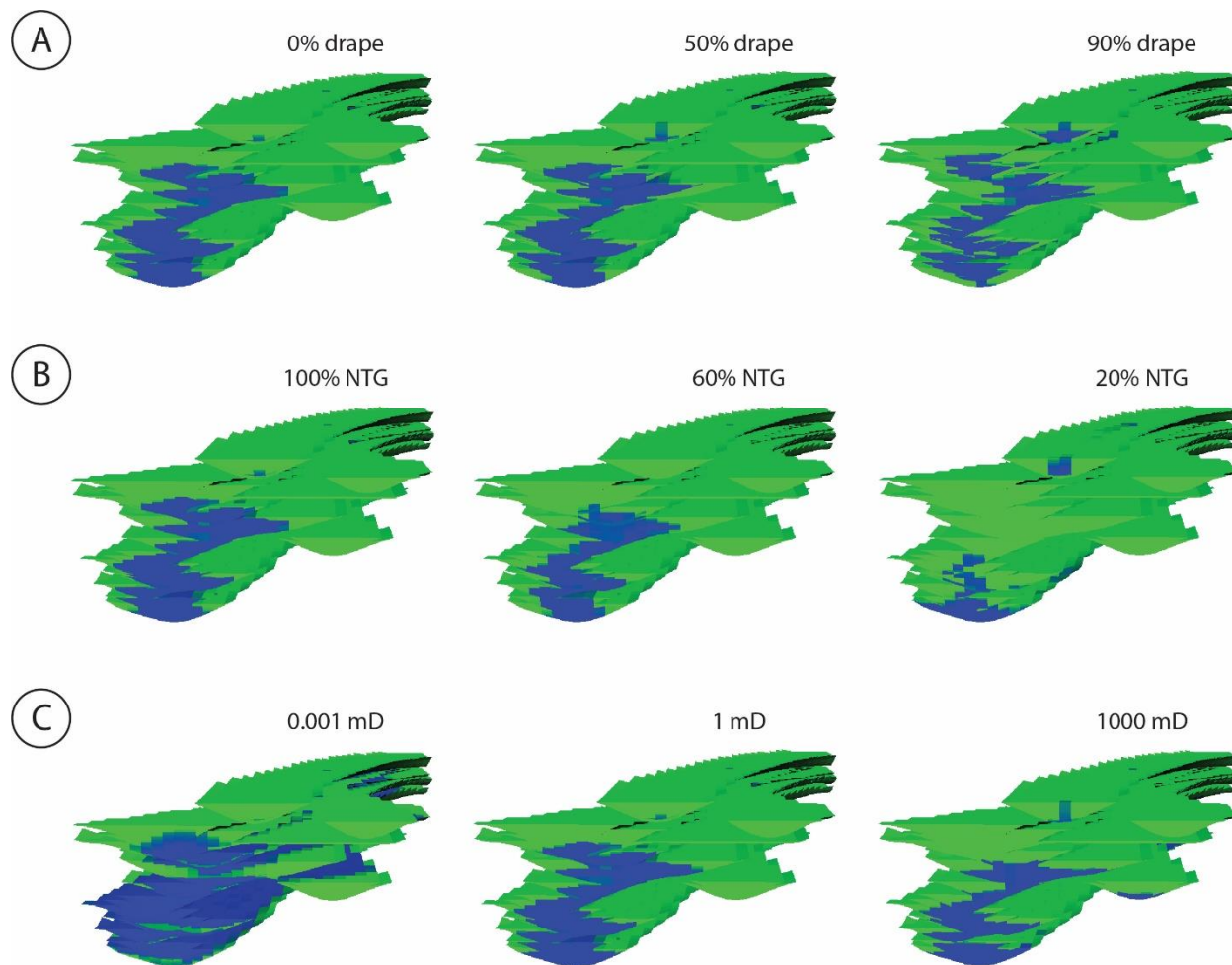


Figure 26. Deterministic model flow simulations at varying values for (A) channel base drape coverage, (B) net to gross ratio, and (C) vertical permeability of MTD facies. Green cells have been bypassed and are oil saturated, while blue cells have been swept with water.

4.4.5 Deterministic Model Results

Much like in the simple model analysis, RE decreases with both increasing $drape$ and decreasing NTG (Fig. 27A). Decreasing either of these parameters creates a constriction of the flow path, resulting in a quicker breakthrough time and less oil produced at water breakthrough. The effect is more pronounced when decreasing the NTG , and more muted when increasing $drape$. This result differs from that seen in the simple model analysis, where the quicker breakthrough times achieved when lowering NTG is offset by a lower $OOIP$, resulting in a flatter RE curve. Conversely, the funneling effect observed in the simple model $drape$ analysis leaves a high amount of bypassed pay, providing a steeper curve. In the case of the deterministic model, it appears that despite a restriction in the flow path provided by increasing $drape$, the system doesn't show significant decline in RE below 70% $drape$ coverage. RE does drop off quickly when lowering NTG , as the lower net margins of the channels combined with the complex stacking pattern result in a significantly constricted flow pathway and a high amount of bypassed pay.

Decreasing NTG also results in lower $CUMoil @ 0.1PVI$, as the producing wells are unable to maintain their assigned liquid rates at anything below 100% NTG (Fig. 27C). The curve for $drape$, however, is completely flat. The high NTG channel elements allow oil to continue flowing into the producing wells, despite the increasing $drape$, resulting in very little decrease in RE .

When MTD K_z is the sole restriction to fluid flow, the trend for BT is very clear and predictable. As you decrease the permeability of the MTDs, water takes much longer to pass through them, increasing the BT (Fig. 27B). The curve flattens at high perm values, as the MTDs no longer restrict fluid flow. The trend for RE is more complex, however. As MTD K_z decreases to 0.1 mD, the trend of increasing RE with increasing BT fits with trends seen in the simple models (Fig. 27B). The producing wells have more time to produce oil, and thus are able to drain a larger

portion of the *OOIP*. However, as MTD K_z decreases beyond 0.1 mD, the *RE* experiences a steep drop-off from 0.45 at 0.1 mD to 0.10 at 0.001 mD. This reversal in the trend coincides with the precipitous drop-off in *CUMoil @ 0.1PVI* (Fig. 27D). This curve is essentially flat at K_z values above 0.1 mD, implying that the producing wells were able to produce at their prescribed liquid rates, despite the presence of the MTDs. As the K_z drops below 0.1 mD however, this cumulative oil value quickly drops, as the flow restriction caused by the MTDs does not allow the wells to maintain their production. Thus, even as *BT* continues to increase with decreasing MTD K_z , the actual oil produced at breakthrough continues to drop, resulting in lower *RE* values.

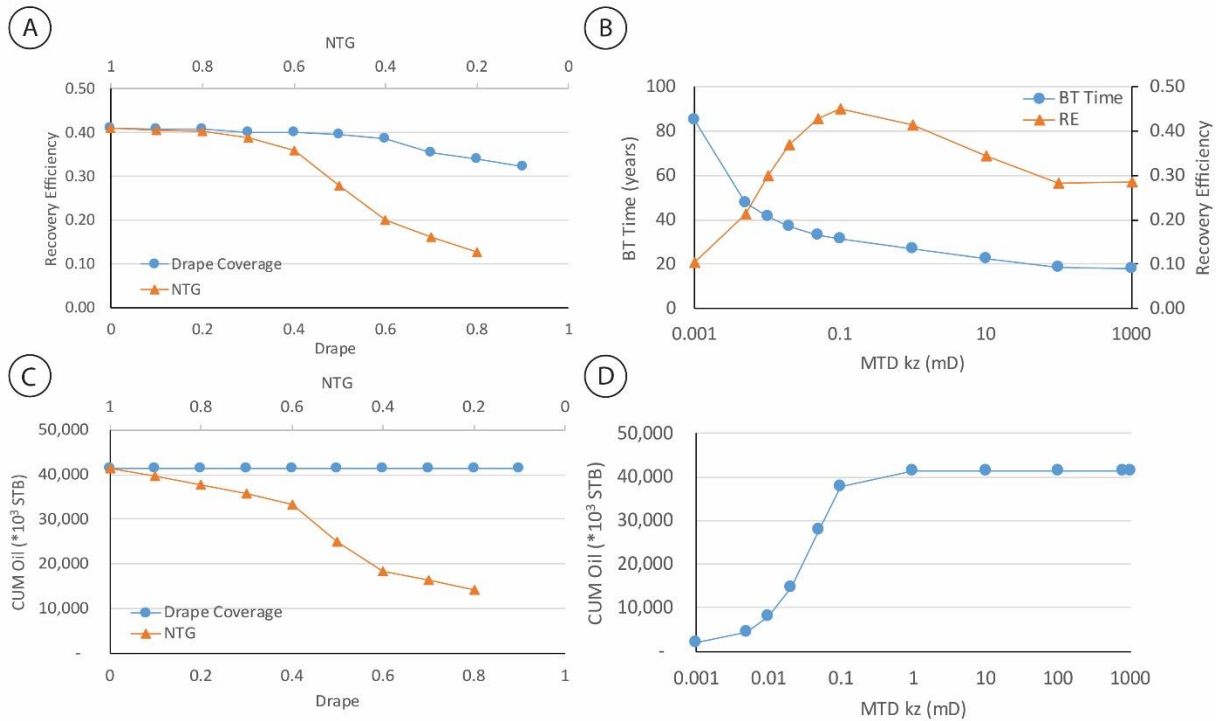


Figure 27. Scatter plots showing simulation results for the deterministic model runs. (A) *RE* versus *NTG* and *drape*. (B) *BT* in years and *RE* versus K_z of MTD facies. (C) *CUMoil @ 0.1 PVI* versus *NTG* and *drape*. (D) *CUMoil @ 0.1 PVI* versus K_z of MTD facies.

4.5 Stochastic Models

4.5.1 Description of Stochastic Model Analysis

The third and final sensitivity analysis utilizes object-based modeling methods to test whether readily available subsurface data (e.g. seismic-scale horizons and well information) could be used to constrain channel placement and recreate the previously documented deterministic connectivity using standard geostatistical modeling approaches. Object-based modeling was chosen over other cell-based categorical geostatistical methods (e.g. multiple point statistics or sequential indicator simulation) because 1) it produces visually attractive and identifiable geometries that honor those seen in outcrop or high-resolution seismic data, 2) these geometries were easily sourced from the existing deterministic model, and 3) the method allows considerably more control on channel geometry than methods employing variograms or multiple-point statistics. This final stage of analysis utilizes channel complex set surfaces and three pseudo-wells derived from the deterministic model as representations of subsurface data to generate a series of models that explore the sensitivity to three variables that are unknown and must be modeled in the subsurface: 1) channel position, 2) MTD proportion, and 3) channel element NTG. Overall proportion of channels are kept consistent with the deterministic model, resulting in very similar *OOIP* values (359,000,000 STBO in the base-case deterministic model versus an average of 351,000,000 STBO in the stochastic models).

4.5.2 Model Construction

The stochastic models were meant to mimic the deterministic model, with two zones representing the upper and lower complex sets being populated with a set proportion of channel facies. The basic framework was constructed using five surfaces: model base, lower complex set

surface, top of lower complex set, upper complex set surface, and model top (Figure 28A). Complex set surfaces were chosen to constrain the model because these surface are often resolvable in seismic surveys, whereas the channel complex and element surfaces are not. The dimensions of the stochastic models (2250 m x 2000 m x 265 m) are identical to the deterministic model, as are the cell sizes (50 m x 50 m x 2.5 m) (Figure 28B). Layering in the stochastic models is a simplified version of the deterministic model, with the complex set surfaces still acting as base surfaces and the layering scheme still following a flat top surface which creates flat layers within the two channel complex set containers.

Three pseudo-wells were generated to use as input for the stochastic modeling, spaced evenly across the model following the axes of the complex set surfaces. Synthetic *facies* logs were created for each well from the *facies* property of the deterministic model, and were used to generate a new *facies* property for the stochastic model (Figure 29A). A total of four facies are included in the models: thick-bedded amalgamated sandstone (axis), thick to thin-bedded semi-amalgamated sandstone (off-axis), mass transport deposit facies, and out of channel or background facies. Notably absent is the thin-bedded non-amalgamated sandstone facies, which corresponds to the channel margins. This exclusion is a consequence of the input parameters offered in the object-based modeling menu, which only include facies options for “channel sand” and “channel levee” (Figure 30A).

The object-based facies modeling method maps facies to specific geometries, in this case meant for a fluvial system. However, this process is easily adapted to a deep-water environment by using channel sizes and geometries consistent with what is observed in outcrop. The modeling was performed using two types of objects: fluvial channels, which include channel sands and levees, and lower half pipes used to represent mass transport deposits. Channel levees are not

actually being modeled in this study; due to the limited input options, they are being used as a proxy for the off-axis of the channel element. Lower half pipes were the chosen geometry for the MTDs because it was the option that most closely resembled the MTD fills at the bases of channel complex erosion surfaces. Proportion of facies and object geometries were chosen based on average values from the deterministic model. Stochastic objects were only simulated within the interpreted channel complex sets surfaces (Zones 2 and 4; Figure 28B). Both zones contained identical input parameters. Zones 1 and 3 were designated as inactive or background facies (i.e., no porosity or permeability), removing them from the flow simulations. In total, 91 different models were generated and flow simulated to test a variety of MTD proportions, NTG ratios, and stacking patterns. A simplified example of input parameters used to generate the stochastic models is shown in Figure 30.

The geometric method used to calculate petrophysical properties in the deterministic model was not feasible for the stochastic models, as the random placement of channel elements eliminated the possibility of calculating rock properties in relation to a channel centerline. Rather, channel properties were assigned using simple calculations shown in Equations 8, 9, and 10. Equation 8 is an example of a porosity calculation, where facies 1 (channel axis) is assigned a ϕ of 0.3, facies 2 (channel off-axis) is assigned a ϕ of 0.2, facies 5 (MTD) is assigned a ϕ of 0.01, and anything else (i.e. background facies) is assigned a ϕ of 0. The channel properties were chosen from Stewart et al., 2008, and the MTD properties were chosen based on the MTD K_z results from the deterministic model, where a value of 0.1 mD is at the apex of the RE curve. The out of channel facies are assigned porosity and permeability values of zero, giving them no storage or flow potential.

$$\phi = \text{if}(\text{facies} = 1, 0.3, \text{if}(\text{facies} = 2, 0.2, \text{if}(\text{facies} = 5, 0.01, 0))) \quad (8)$$

K_{xy} (Equation 9) and K_z (Equation 10) were calculated in the same manner, using values referenced from the base-case deterministic model. As in the deterministic model, the K_z value for the axis facies is equal to K_{xy} , but is equal to one tenth of the value in the in the off-axis, and in this case in the MTD facies as well.

$$K_{xy} = \text{if}(\text{facies} = 1, 792.5, \text{if}(\text{facies} = 2, 600, \text{if}(\text{facies} = 5, 1, 0))) \quad (9)$$

$$K_z = \text{if}(\text{facies} = 1, 792.5, \text{if}(\text{facies} = 2, 79.2, \text{if}(\text{facies} = 5, 0.1, 0))) \quad (10)$$

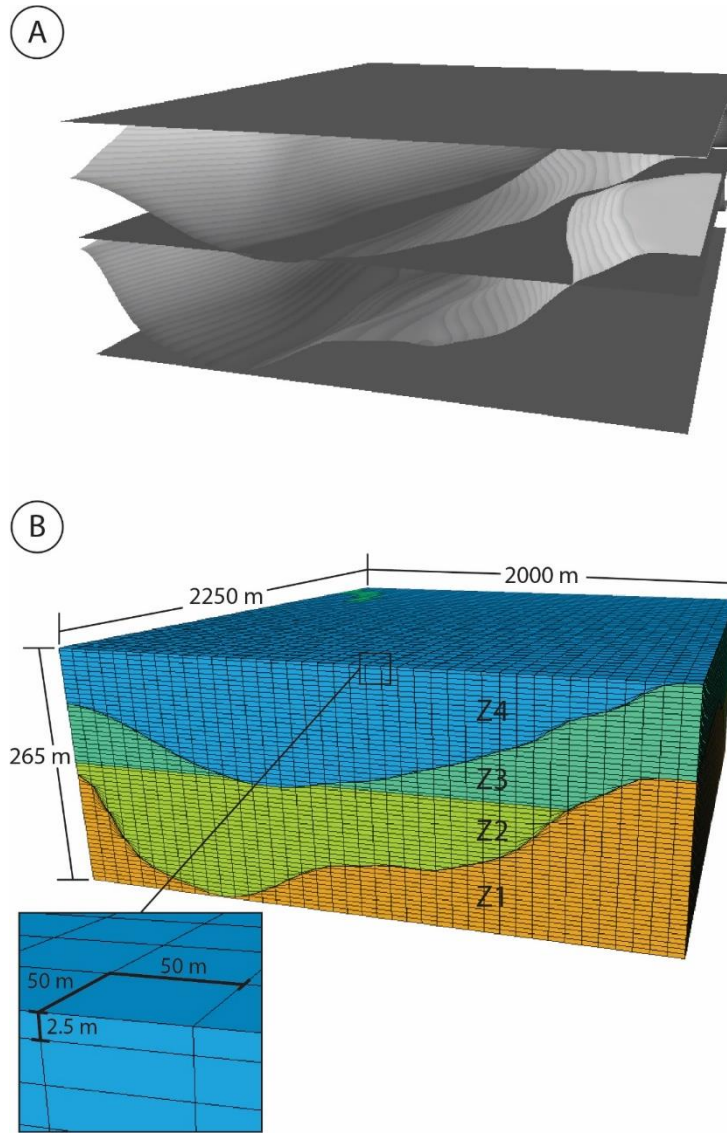


Figure 28. (A) Image of the five surfaces used in generating the stochastic modeling framework, displayed in 3D space. (B) Model dimensions and grid cell size for the stochastic modeling framework. Zones are labeled Z1-Z4 for reference.

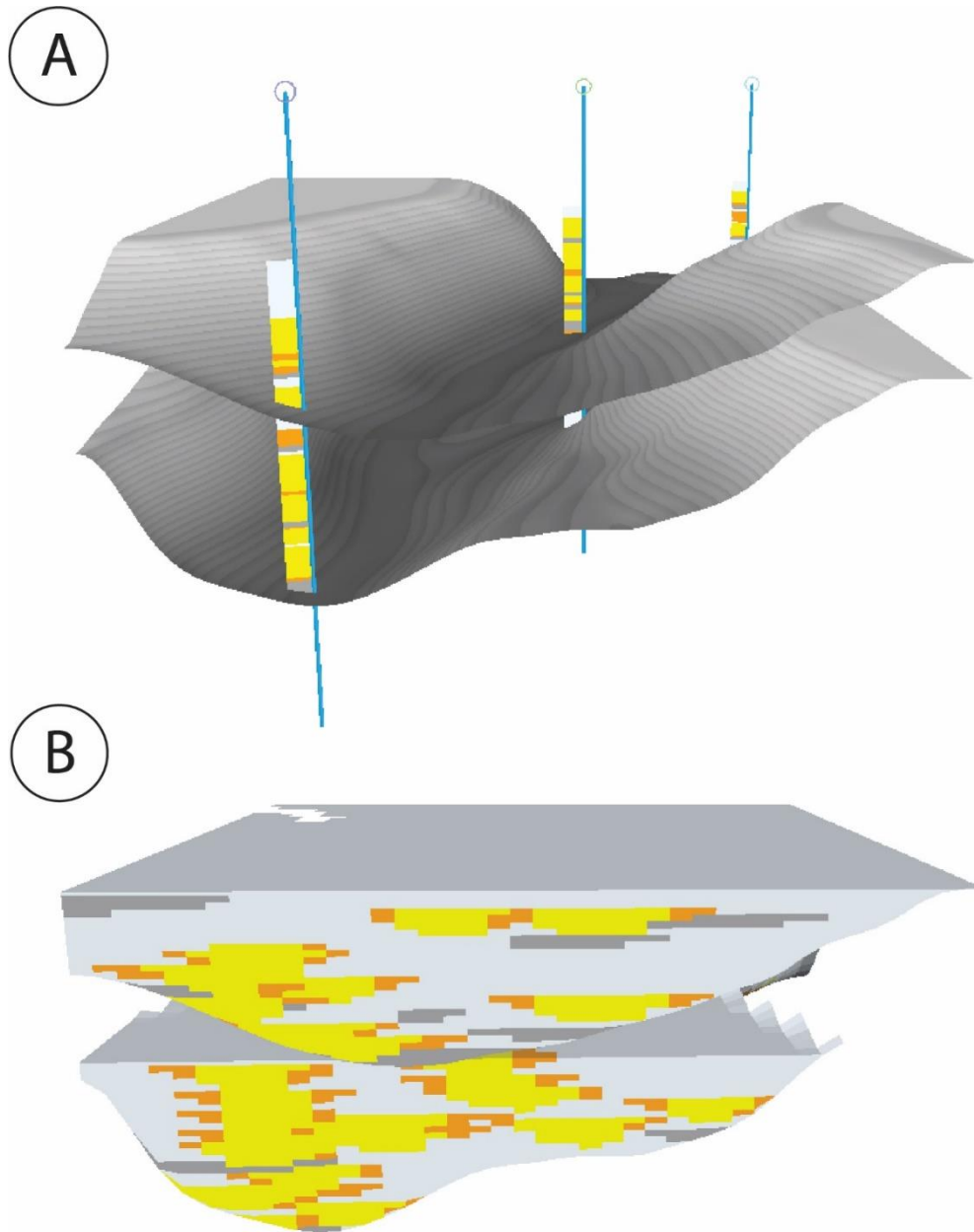


Figure 29. (A) Pseudo-wells with facies logs derived from the deterministic model, evenly spaced along the axes of the channel complex sets. These were the basis of the stochastic models. (B) Example of a stochastically generated model, including channel sands (axis), channel levees (off-axis/margin), and mass transport deposits. Hidden zones contain only background facies.

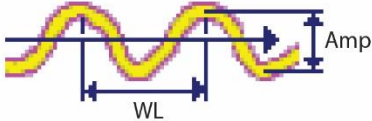
A Stochastic Channel Inputs

1. Channel sand and levee facies

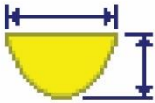
Facies: 1: Highly A Channel sand

2: Semi-A Levee

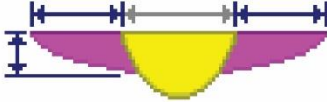
2. Channel orientation, amplitude, and wavelength



3. Channel width and thickness



4. Levee width and thickness



B Stochastic MTD Inputs

1. Object facies

Facies: 5: MTD

2. Object body shape

- Box
- Pipe
- Upper half pipe
- Lower half pipe
- Ellipse
- Half ellipse
- Quart ellipse
- Fan lobe
- Aeolian sand dune
- Oxbow lakes

3. Object orientation, length, width, and thickness

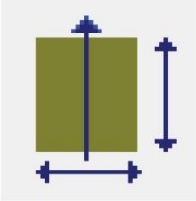


Figure 30. Simplified input parameters for object-based facies modeling. (A) Input parameters for stochastic fluvial channels, adapted for a deep-water system. Options control facies inputs and geometries for channel sands (axis) and levees (off-axis/margins). (B) Input parameters for stochastic “lower half pipes” used to represent MTDs. Options control facies, object body shape, and object geometry.

4.5.3 Sensitivity Variables

Two primary sensitivity variables were evaluated in this study: proportion of MTD facies and NTG ratio (Table 8). A third variable, stacking pattern, was created as a direct result of utilizing multiple realizations at each *NTG* or MTD proportion value to provide a range of outcomes for the two primary variables. Seven proportion values ranging from zero to thirty percent were used for the MTD analysis, with ten different models using different stochastic channel placements generated for each MTD value. For the *NTG* analysis, three similar models were chosen from the 15% MTD proportion series, corresponding to seed numbers 400, 500, and 900. These models were chosen for their similarity of channel stacking pattern and similar *RE* values in the MTD proportion analysis. Different *NTG* values were assigned to the channel sand and channel levees, creating average *NTG* values for the models ranging from approximately 35 to 95%. Porosity and permeability were then calculated in the same manner as the simple and deterministic models, utilizing equations 2, 3, and 4. MTD facies were assigned a constant ϕ of 0.01, K_{XY} of 1 mD, and K_Z of 0.1 mD. Background facies were assigned values of 0 for ϕ and K_{XY}/K_Z .

The variation in the stochastic stacking patterns is on display in Figure 31, with Figure 31A displaying ten different model realizations using the same input parameters, and Figure 31B showing a varying proportion of MTD facies. Seed numbers were entered manually for each simulation, with the intention of creating more consistent stacking patterns for each MTD proportion value. However, despite repeated use of the same seed numbers, the addition of MTD facies into the model generation alters each stacking pattern slightly (Fig. 31B). An example from the *NTG* analysis is shown in Figure 32, with three different models with an average *NTG* value

of 95% (Fig. 32A) being shown alongside their associated φ (Fig. 32B), K_{xy} (Fig. 32C), and K_z (Fig. 32D) properties.

Table 8: Table of sensitivity variable value ranges for stochastic models. For the MTD proportion analysis, 0% MTD represents the base case, while the NTG analysis is represented by the 95% NTG case.

Sensitivity Variable	Value Range
MTD Proportion	0-30%
NTG	35-95%

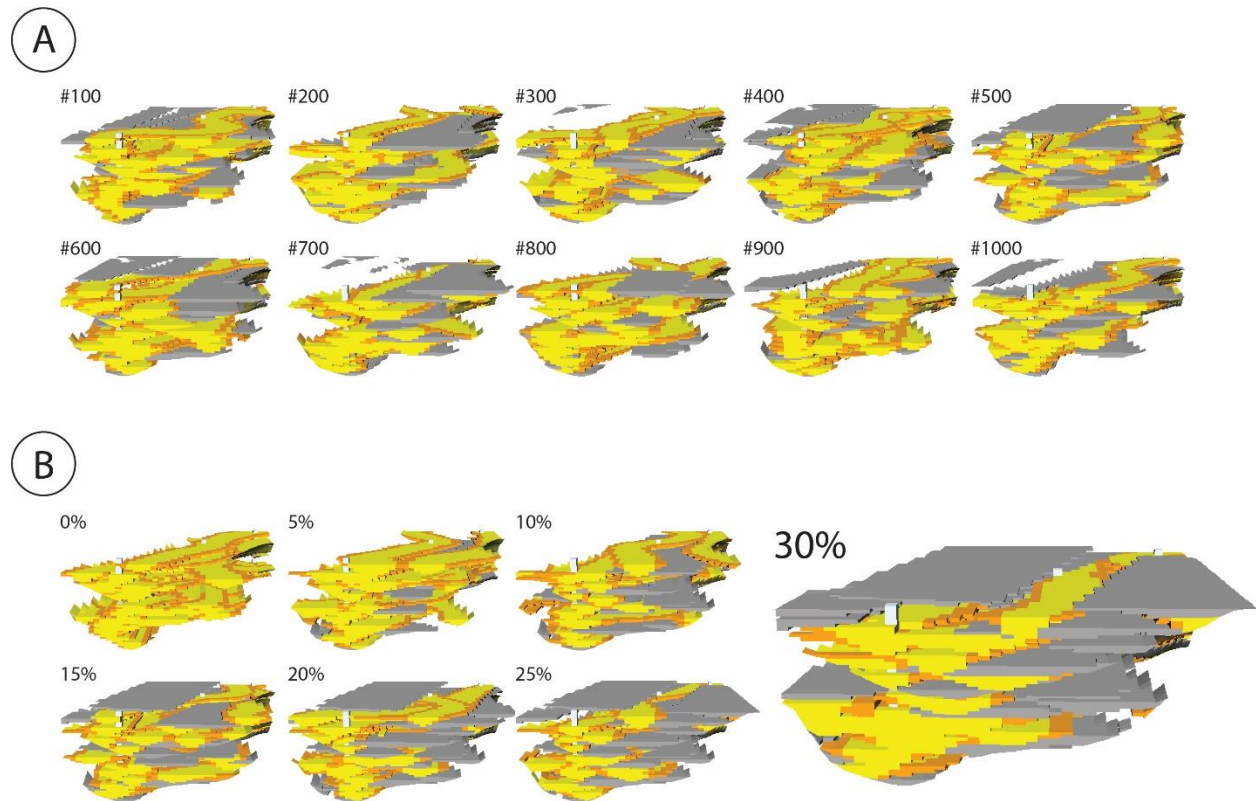


Figure 31. Stochastic model simulations showing different (A) stacking patterns from different model realizations, and (B) proportion of MTD facies.

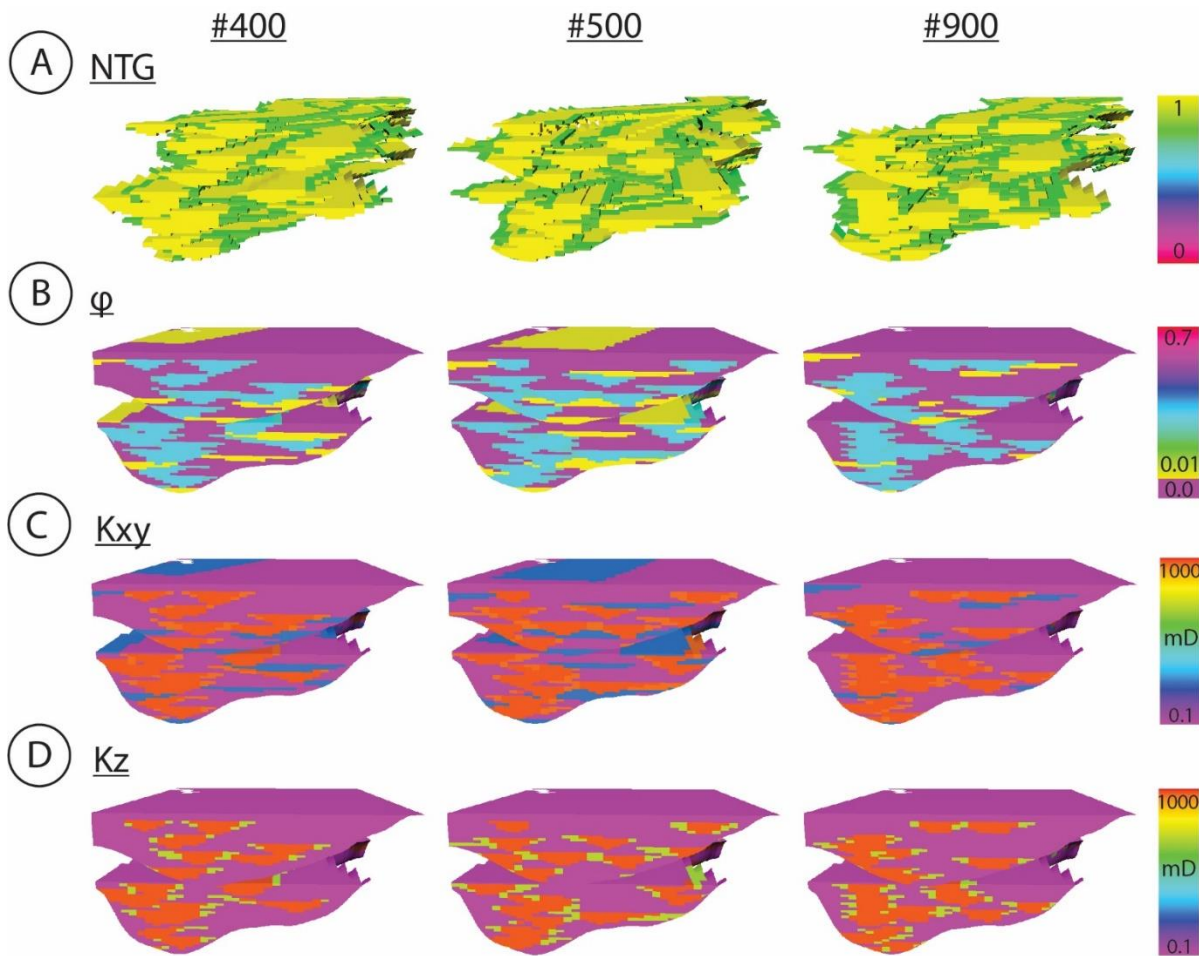


Figure 32. Petrophysical properties used in the net to gross analysis for the stochastic models. Examples are shown for each model realization used in the sensitivity analysis. (A) *NTG* (average 96%). (B) Porosity (φ) (C) Horizontal permeability (K_{xy}). (D) Vertical permeability (K_z).

4.5.4 Flow Simulation

As with the first two chapters of the sensitivity analysis, the flow simulations in the final chapter were performed utilizing a constant flux bottom-drive aquifer at the base of the model and three producing wells (Figure 33). The placement and depth of the producing wells needed to take the stochastic nature of the channel elements into account, ensuring that each well was connected to an element. Therefore, the wells were placed in the exact locations of the pseudo-wells used to generate the object-based models, with the extraction depth coinciding with the uppermost channel facies of each upscaled facies log.

The producers were set at a constant liquid rate of 5000 barrels per day, and when the wells were unable to produce at the prescribed rate, they would switch to being controlled by bottom hole pressure. Aquifer influx and well liquid rates were held constant for all models in the stochastic study, once again ignoring the effects on reservoir pressures. As in the deterministic model, run times varied depending on the sensitivity variables being tested, as well as the stochastic stacking pattern of the channels. Breakthrough times ranged from 1295 days (15% MTD facies, seed #300) to 27,200 days (0% MTD facies, seed #1000). Of the 91 total flow simulations performed in this analysis, only three were unable to achieve water breakthrough. In each of these cases, there was not a continuous flow path of permeable facies from the aquifer to the producing wells, causing large pressure spikes but no actual vertical flow beyond a certain point.

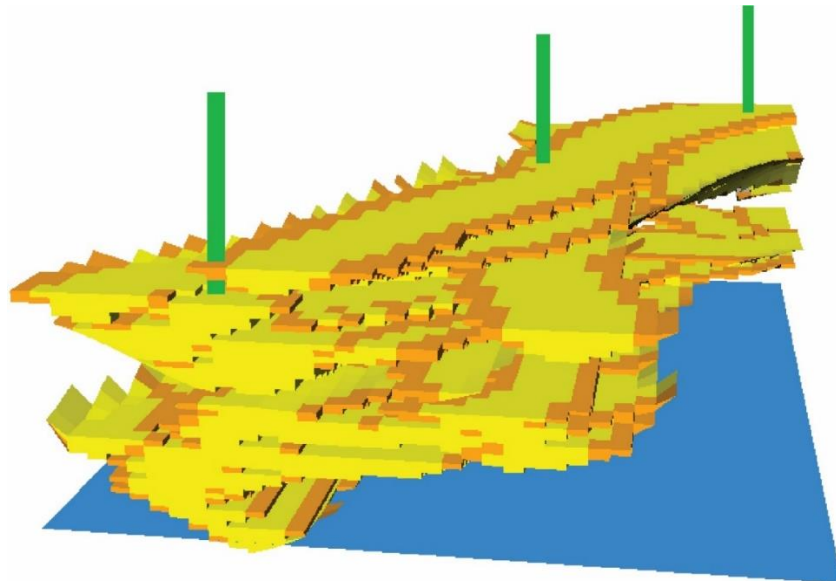


Figure 33. Flow simulation setup for the stochastic model sensitivity analysis. A constant flux aquifer inputs water at the base of the model, while three evenly-spaced producing wells draw from the top of the model. In the stochastic analysis, the producing wells draw from the depth of the uppermost channel facies in each of the three original pseudo-wells to ensure connection to a channel element.

4.5.5 Stochastic Model Results

Stochastic model simulation results for the MTD proportion and *NTG* analyses are shown in Figure 36, with individual model runs expressed as blue circles and mean values for each set of models (e.g. all models with 20% MTD facies) expressed as orange triangles. Each stochastic model was assigned a set proportion of each facies (e.g. 20% MTD), but due to the stochastic variation in stacking patterns with different model realizations, the actual proportion of MTD facies was variable (e.g. 19.24% – 20.40%). Therefore, the average value indicator sits slightly above or below the assigned value for the set (e.g. 19.86%).

Beginning with the MTD proportion analysis, there is a fairly high amount of scatter in *BT* at low MTD proportion values, but a general decrease in *BT* as MTD proportion is increased from 0% to 15% is apparent (Fig. 34A). As MTD proportion is increased further, the trend remains largely flat, with slightly more scatter in the results at 30% MTD facies. This trend is somewhat consistent with the results seen in the simple and deterministic model drupe analyses, implying that the low-permeability MTD facies may be acting to constrict fluid flow and accelerate breakthrough times. This trend appears to mostly hold up for *RE*, but much more scatter is evident in the results for different channel placement realizations (Fig. 34B). There is a small decrease in *RE* from 0% to 15% MTD proportion, with a flatter trend at increased proportions. The lack of clustering around the average *RE* values speaks to a variety of factors at work, likely directly tied to the stochastic nature of the stacking patterns in the models. While *BT* does still impact *RE*, other factors like reservoir compartmentalization due to blocked flow paths are likely at play. This concept is further reinforced by the plot of *CUMoil @ 0.1PVI* (Fig. 34C). The noticeable scatter within each set of points is evidence that the producing wells are not able to produce at the same

liquid rates for each different stacking pattern, meaning that not all reservoirs exhibit the same flow path connectivity.

The *NTG* analysis utilizes far fewer data points, and thus shows more defined trends. Scatter among each set of three points is low, as the three model realizations chosen for this analysis were selected based on their similar *RE* values in the MTD proportion analysis. A clear trend of decreasing *BT* with decreasing *NTG* is observed (Fig. 34D), which most closely resembles the trend seen in the *NTG* analysis for the deterministic model. Likewise, the flatter trend seen with *RE* is consistent with that seen in the previous sections, as *OOIP* decreases alongside decreasing *NTG* (Fig. 34E). Despite the constant prescribed liquid rates for each simulation, there is also a clear trend of decreasing *CUMoil @ 0.1PVI* with decreasing *NTG* (Fig. 34F). As with the deterministic model analysis, the decreased *NTG* ratio does not allow the pumping wells to maintain their assigned rates. This result speaks to a restriction of the fluid flow caused by the low permeability of the reservoir, particularly in the channel levees (off-axis).

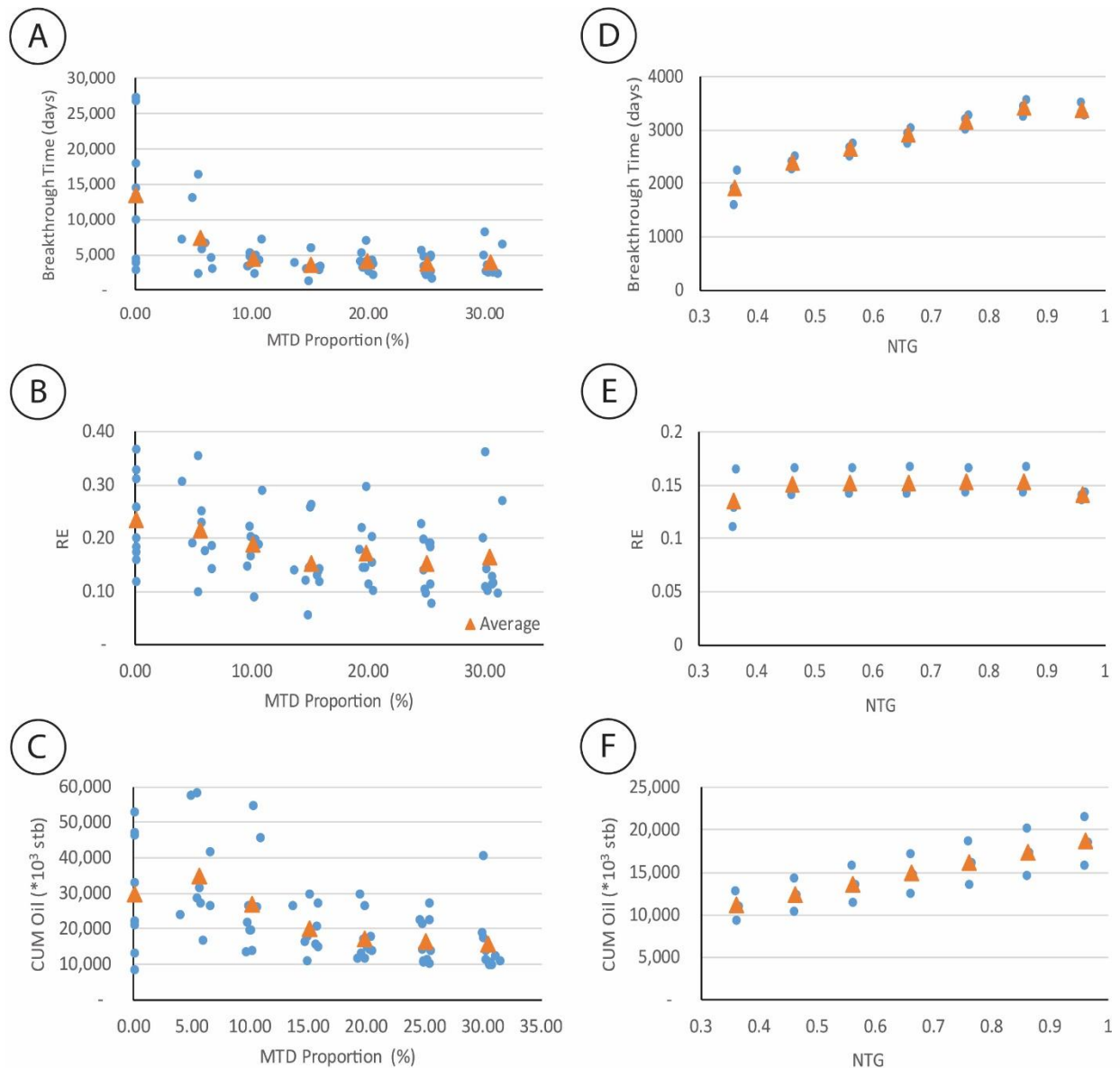


Figure 34. Scatter plots of the stochastic model simulation results for the MTD proportion and *NTG* analyses. Individual runs with varying channel positions are shown as blue circles, while results averaged across model realizations are marked with orange triangles. (A) *BT* in days versus proportion of MTD facies. (B) *RE* versus proportion of MTD facies. (C) *CUMoil* @ 0.1 *PVI* versus proportion of MTD facies. (D) *BT* in days versus *NTG*. (E) *RE* versus *NTG*. (F) *CUMoil* @ 0.1*PVI* versus *NTG*.

CHAPTER 5: DISCUSSION

The goal of this study was to determine whether specific arrangements of hierarchical elements had distinct characteristic flow behaviors, and if so, whether they could be modeled with stochastic modeling algorithms. Three separate modeling techniques were utilized to evaluate architectural elements including percentage and flow properties of mass transport deposits and channel element stacking patterns and fill (i.e. net to gross and drupe coverage).

Simplified models were used to analyze the flow characteristics of channel element stacking patterns and fill in an idealized way that allowed for true isolation of the sensitivity variables. A deterministic model then built upon these results, using outcrop data to create a more architecturally realistic model, including mass transport deposits and a complex stacking pattern that was essentially a combination of those seen in the simple model analysis. Finally, complex set surfaces and pseudo-wells derived from the deterministic model were used in place of subsurface data to try to replicate the previously observed flow properties using stochastic object-based models.

The utilization of all three modeling workflows allowed for a more robust analysis of characteristic flow behaviors in hierarchically organized deep-water systems. The three stages of analysis built upon each other, allowing the research question to be approached from several angles. This ultimately aided in identifying flow behaviors common throughout the stratified approach, including flow baffles, flow barriers, and reservoir compartmentalization. Each of these patterns were observed in all three stages of analysis, and will be discussed in this section.

5.1 Flow Baffles

Flow baffling is created in the models when combinations of channel element stacking, low NTG fill, drape coverage, and the presence of MTDs funnel fluid through constricted and tortuous pathways. This reduction in the flow pathway can either increase or decrease breakthrough time depending on the severity of the constriction, and is observed in all three phases of this analysis.

5.1.1 Baffled Flow in Drape and MTD Proportion Analyses

Flow baffles can decrease *BT* and reduce overall *RE* by bypassing pay in sections of the reservoir not along the constricted flow path. This funneling effect is demonstrated by two simple, vertically stacked flow simulations with different *drape* values, where Figures 35A and 35B are constricted by 30% and 80% drape coverage, respectively. The 30% *drape* model achieves water breakthrough after 2,259 days, with an *RE* value of 0.16. While the upper three channel elements remain largely oil saturated, oil in the lower two channel elements, including the margins, is mostly displaced. The much more constricted 80% model preferentially flows directly upward between the impermeable drapes, breaking through more quickly at 1,484 days with an *RE* value of 0.11. In this high *drape* scenario, oil trapped between draped surfaces is completely bypassed, leading to a considerably quicker *BT* and lower *RE* value. This trend is seen in the vertical models above 40% *drape*, diagonal above 30% *drape*, and immediately upon the introduction of any *drape* in the lateral models (Figure 36A).

Baffles can also reduce the flow pathway significantly enough to actually increase *BT* and *RE*. This behavior is seen in the diagonally and laterally stacked models, when the *drape* is increased from 60% to 70% and 30% to 40%, respectively (Figure 36A). In the diagonal case,

increasing *drape* from 60% to 70% increases *BT* from 4,905 days to 5,320 days, resulting in an increase in *RE* from 0.35 to 0.38. Likewise, in the lateral case, increasing *drape* from 30% to 40% increases *BT* from 6,447 days to 6,500 days, resulting in a modest increase in *RE* from 0.438 to 0.441. These four simulation results are shown in Figure 37, where the red drape cells constrict the flow pathways between adjacent channel elements in the 70% diagonal (Fig. 37B) and 40% lateral (Fig. 37D) cases. These two cases show slightly more displacement of oil (i.e. more blue cells), though the effect is subtle due to the low increases in *RE*, particularly in the lateral case.

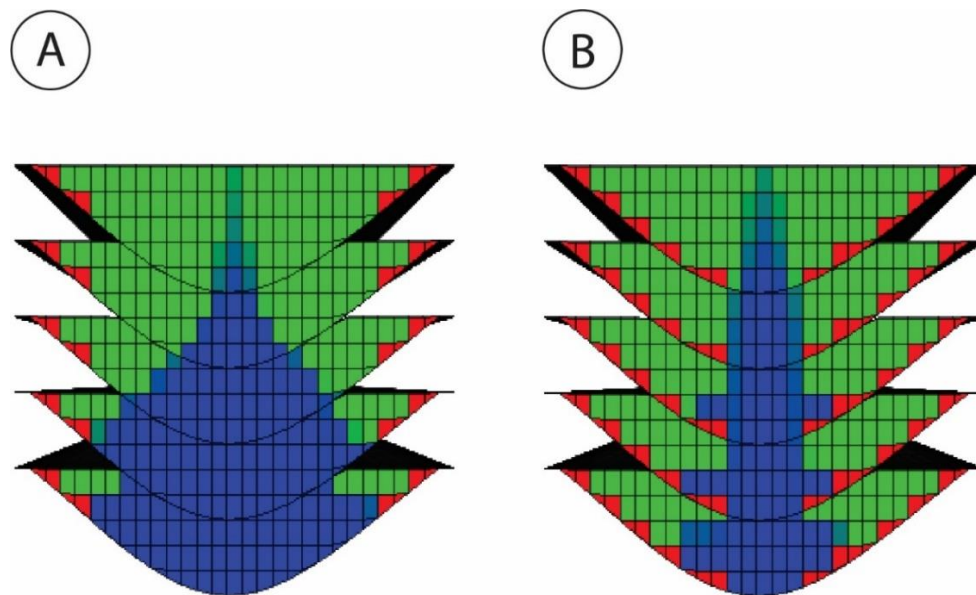


Figure 35. Comparison of two flow simulations from the vertically stacked simple model series to illustrate the funneling effect of drape coverage. (A) 30% *drape*, water breakthrough in 2,259 days, *RE* of 0.159. (B) 80% *drape*, water breakthrough in 1,484 days, *RE* of 0.105.

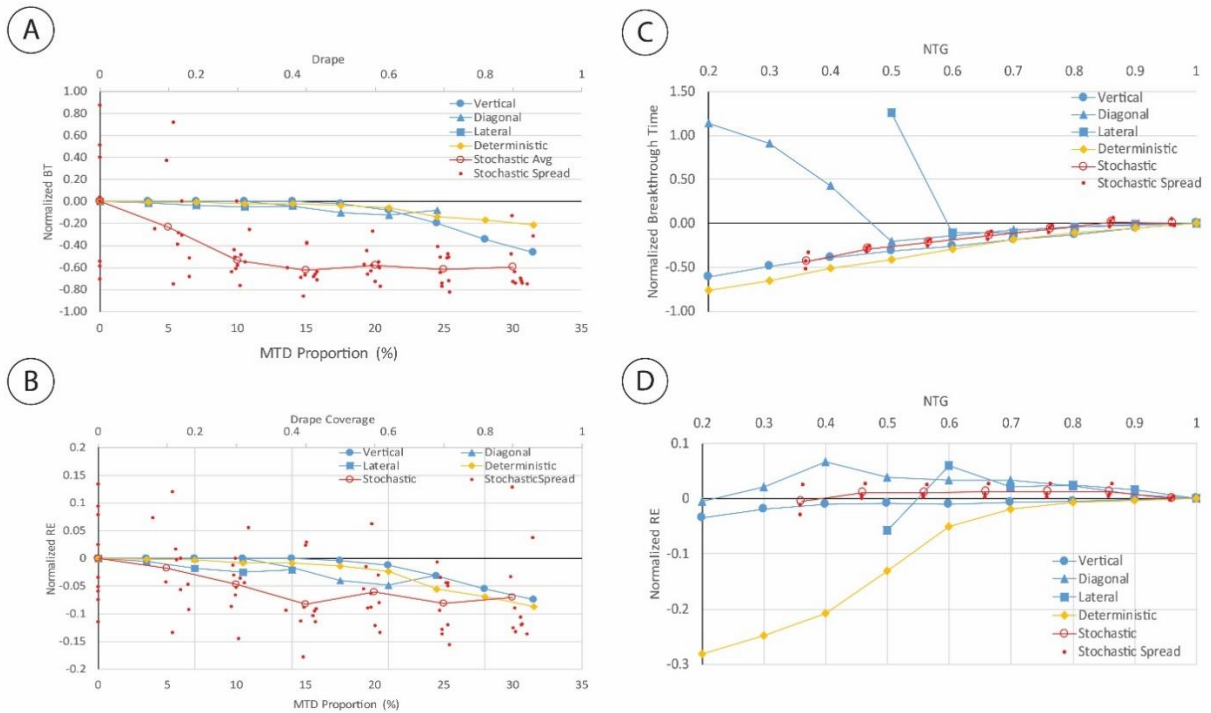


Figure 36. Scatter plots showing combined simulation results of simple, deterministic, and stochastic models. Data points are shown for each stochastic model as solid red circles, while the average of results at each MTD proportion are shown as open red circles. Two anomalously high BT data points have been removed from the 0% MTD series. (A) Normalized BT versus $drape$ and MTD proportion. BT has been normalized as a proportional decline relative to the 0% $drape$ or 0% MTD base cases. (B) Normalized RE versus $drape$ and MTD proportion. RE has been normalized relative to the base case for each set of models. (C) Normalized BT versus NTG . BT has been normalized as a proportional change relative to the 100% NTG case for simple and deterministic models and 95% NTG case for the stochastic models. (D) Normalized RE versus NTG . RE has been normalized relative to the base case for each set of models.

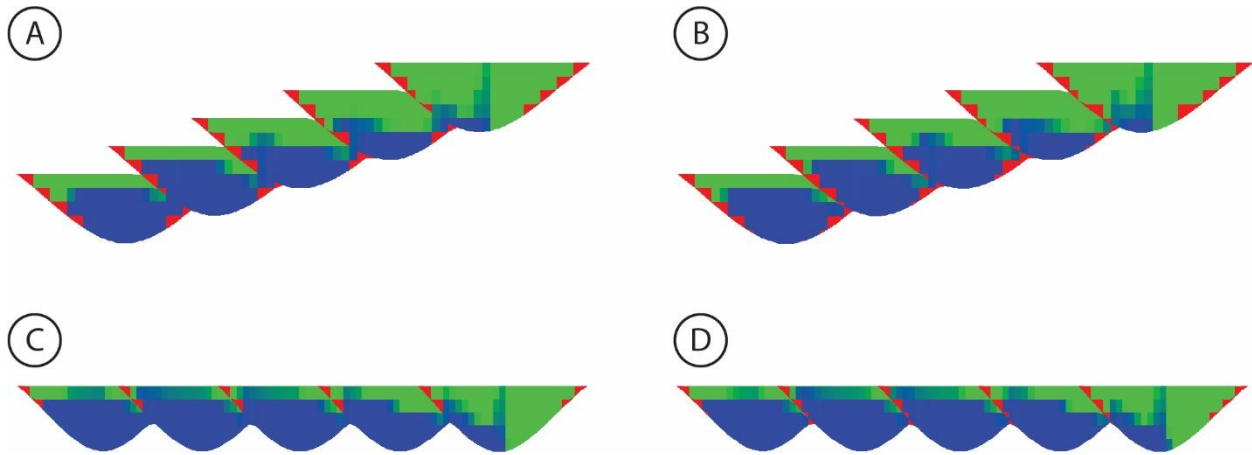


Figure 37. Comparison of simulation results at water breakthrough between simple models stacked (A) diagonally with 60% *drape*, (B) diagonally with 70% *drape*, (C) laterally with 30% *drape*, and (D) laterally with 40% *drape*. Green cells have been bypassed and are oil saturated, blue cells had oil displaced by water, and red drape cells act as flow barriers. Intersection slices are aligned with one producing well.

Similar flow behavior to that observed in the drape coverage analysis for the simple models is observed in the deterministic and stochastic models. In the case of the deterministic model, the simulation results closely mimic those seen for the vertically stacked simple models, where an increase in *drape* results in decreased *BT* and *RE* (Fig. 36A & B). The deterministic model is in essence a combination of stacking patterns, but it appears that the overall vertical orientation results in flow behavior most closely matching that of the vertically stacked simple models, as observed in Figure 38A. The addition of stochastic MTDs had an effect more similar, albeit more severe and with more scatter, to that observed in the lateral and diagonal simple models. *BT* and *RE* declined steeply as MTD proportion was increased from 0% to 15%, at which point the curves generally leveled off (Fig. 36A & B). This trend is reminiscent of the increases in *BT* seen for the diagonal and lateral simple models at high *drape* levels, highlighting that the stochastic MTDs act more as flow baffles than barriers. This idea is discussed in more detail in the barriers section of this chapter.

5.1.2 Baffled Flow in NTG Analyses

Flow behaviors related to a reduction in *NTG* are slightly more complex than those for increasing *drape*, as a decrease in *NTG* coincides with a decrease in *OOIP*. In the vertically stacked simple models, decreasing *NTG* acts very similarly to increasing *drape* in that there is a steady decline in *BT*. Flow in a vertically stacked system is concentrated in the high-net axes, so a reduction of *NTG* in the channel margins acts very similarly to a reduction in the flow pathway caused by channel drapes. This trend is directly mirrored by both the deterministic and stochastic models (Fig. 36C, Fig. 38B). For the diagonally and laterally stacked simple models however, there is a very sharp increase in *BT* when the *NTG* drops below a certain threshold (50% for diagonal, 60% for lateral) (Fig. 36C). This shows that the low net margins of channel elements that exhibit significant lateral offset have a larger overall impact than channel base drapes on the ability of fluid to flow through the system.

Reductions in *BT* as a result of decreased *NTG* are largely offset by a reduction in *OOIP*, leading to flatter normalized *RE* curves in the simple and stochastic model results (Fig. 36D). The vertically stacked simple models still show a slight decrease in *RE* with decreasing *NTG*, but the diagonal, lateral, and stochastic models all show a slight increase in *RE* until a certain threshold is reached. The deterministic model results, however, show a steep decline in *RE* with decreasing *NTG* (Fig. 36D, yellow line). While the deterministic model also had the steepest decline in *BT*, this drop in *RE* appears disproportionately large, meaning there are other factors at work. Most likely, the significant impact of low net margins in laterally offset channels discussed previously has the effect of highly compartmentalizing sections of the reservoir, creating a large amount of bypassed pay. Reservoir compartmentalization will be discussed more thoroughly later in this section.

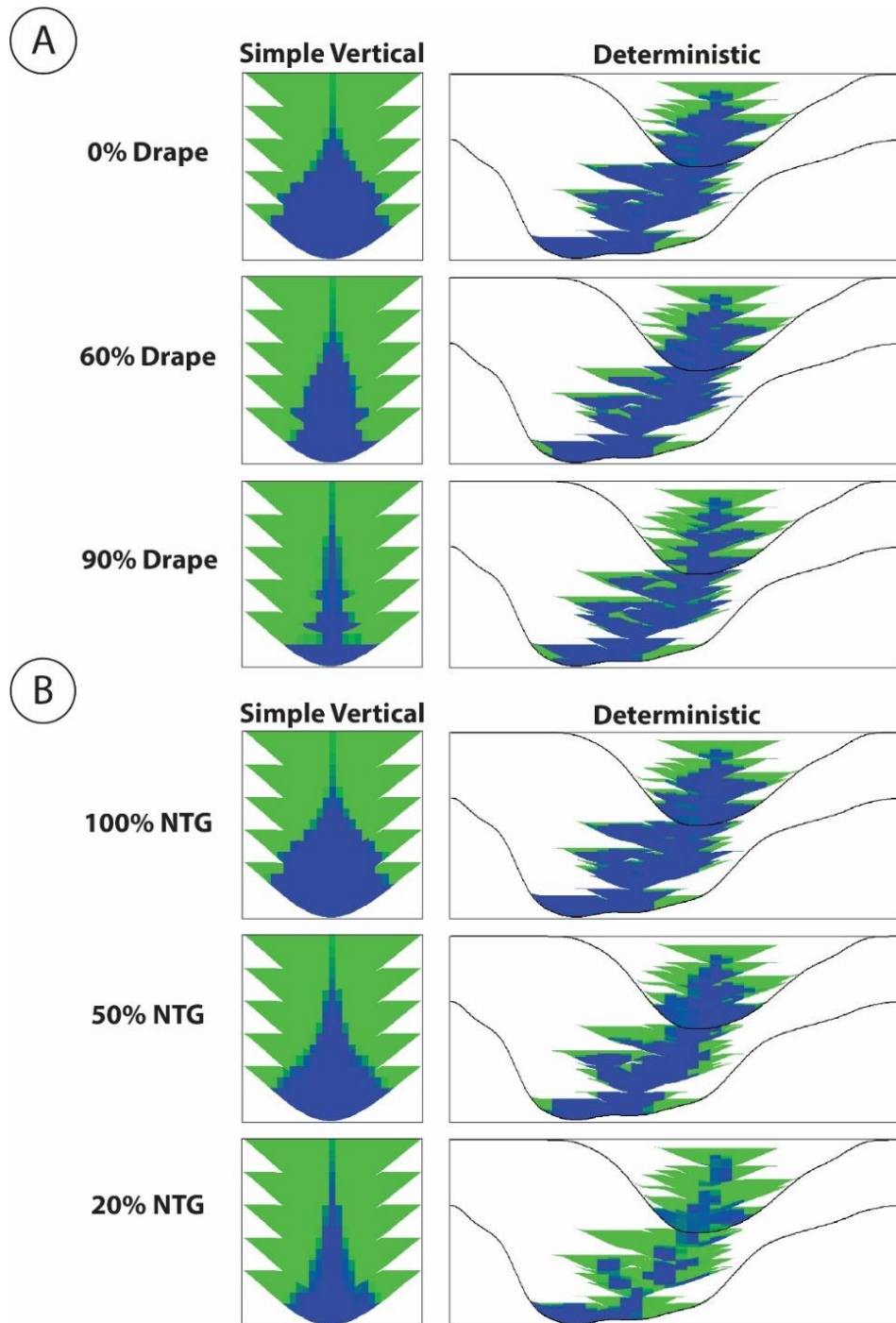


Figure 38. Comparison of flow simulation results at water breakthrough between vertically stacked simple models and the deterministic model across varying (A) drape coverage and (B) net to gross ratio. Green cells have been bypassed and are oil saturated, while blue cells have been replaced with water. Intersection slices are aligned with one producing well.

5.2 Flow Barriers

A flow baffle becomes a flow barrier in this study when the flow path is completely obstructed, either from increasing impermeable drupe coverage, juxtaposing very low net to gross margins, or entirely blocking the flow path with a low permeability MTD. When one or multiple of these situations occurs, the flow simulation is generally unable to achieve water breakthrough, or *BT* occurs after too much time to be useful as a data point. In the diagonally and laterally stacked simple models, the flow pathway is completely shut off once a certain *drape* or *NTG* threshold is reached. The tightening of these pathways is visible in the increases in *BT* seen in Figure 36A & B, after which points flow is cut off completely and the flow baffles have turned into flow barriers. These thresholds provide a natural constraint on the sensitivity ranges used in this study, as any further increases in *drape* or decreases in *NTG* will not result in a usable *BT* data point.

In the deterministic model, flow barriers were created by reducing the vertical permeability of the MTDs at the bases of each channel complex. The scatter plots in Figure 27 demonstrate the effect that reducing permeability in these zones has; *BT* increases exponentially and *RE* quickly drops (Fig. 27B) because the producing wells are unable to maintain their production rates (Fig. 27D).

The intent of introducing MTD facies into the stochastic models was to create a similar barrier effect to that seen in the deterministic model, but on aggregate the MTD objects responded more as flow baffles than barriers. This is highlighted by two stochastic models, both containing a 30% MTD facies proportion (Fig. 39). The MTD objects have set geometries, but are only constrained to the complex set boundaries. There was no additional strict hierarchy built into the stacking pattern, and thus the randomly generated placement of each MTD object dictated how it would impact fluid flow through the system.

Figures 39A and 39C correspond to the model realization with seed number 600, where an MTD object completely obstructed the flow path between the lower and upper complex sets. The MTD facies was assigned a low permeability value, which slowed the flow of water between the lower and upper complex sets considerably. It ultimately took 8,295 days to break through to the producing wells, achieving an *RE* value of 0.36. Figures 39B and 39D correspond to the model realization with seed number 700, where an MTD object only partially obstructed flow between the complex sets. Water was quickly able to permeate through the system, reaching *BT* in just 2,590 days and achieving an *RE* value of 0.11. In effect, the MTD object placement makes model #600 respond more like the deterministic model with low perm MTDs, while model #700 acts more like a vertically stacked simple model or deterministic model with a drape-coverage induced funneling effect (Fig. 40). Revisiting the results for the MTD proportion analysis (Figure 34), it is clear that model #700 is much more representative of the group. While there is a fair amount of scatter due to the stochastic nature of the object placements, there appears to be a general decrease in *BT* with increased MTD proportion, as well as an accompanying decrease in *RE*.

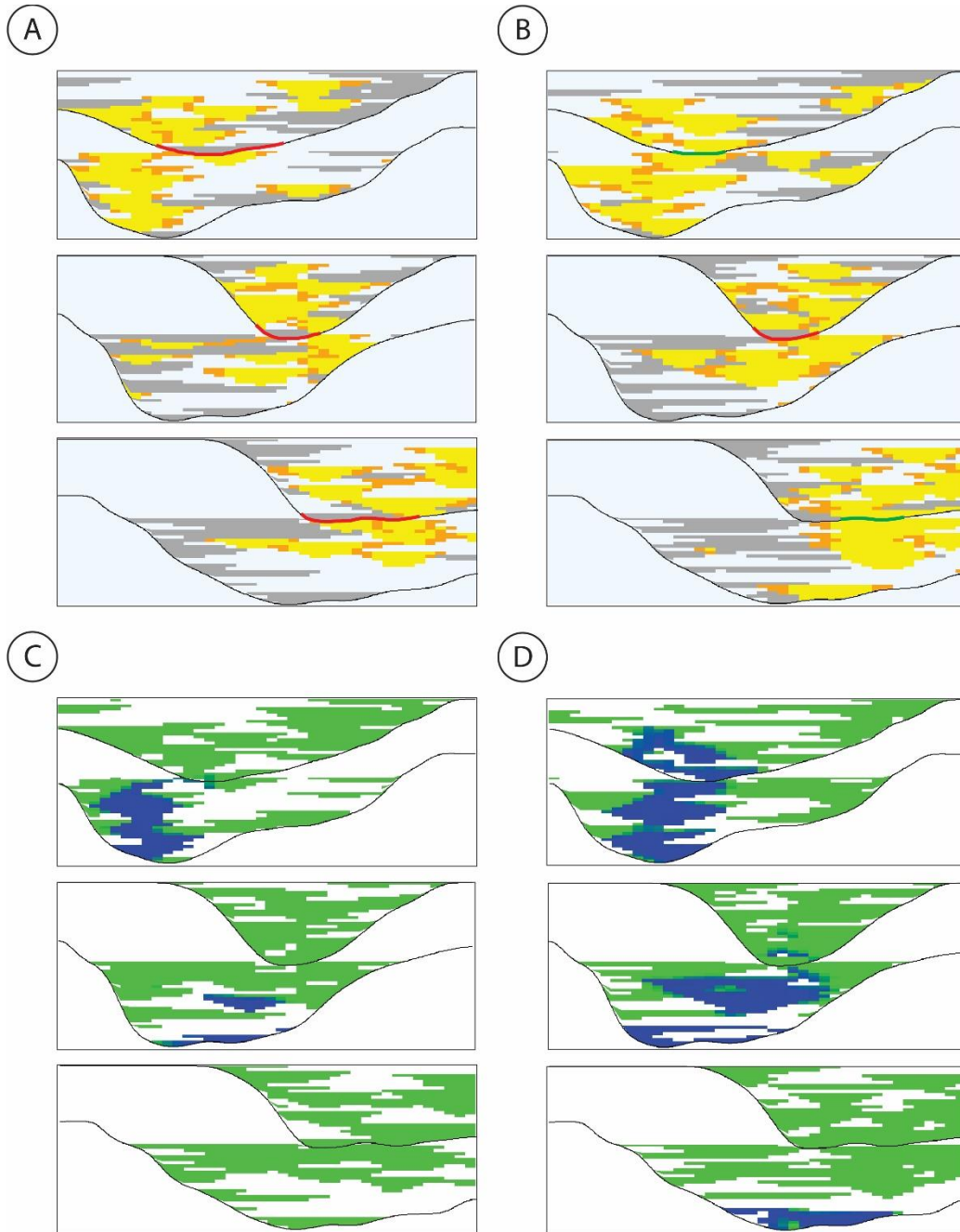


Figure 39. Stochastic model intersection slides comparing two models generated using the same object proportions, but different channel stacking patterns. Each panel contains three slides showing intersections at the south end, middle, and north end of each model. Flow simulations are shown at the time of breakthrough for the #700 model. (A) Seed #600. The randomly generated MTD object completely covers the flow path between the upper and lower complex sets. (B) Seed #700. The MTD object only partially obstructs flow across the complex sets. (C) Flow simulation of the #600 model. The MTD object acts as a barrier and drastically slows water breakthrough into the upper complex set. (D) Flow simulation of the #700 model. The MTD object acts as a flow baffle, but does not prevent water from breaking through to the producing wells.

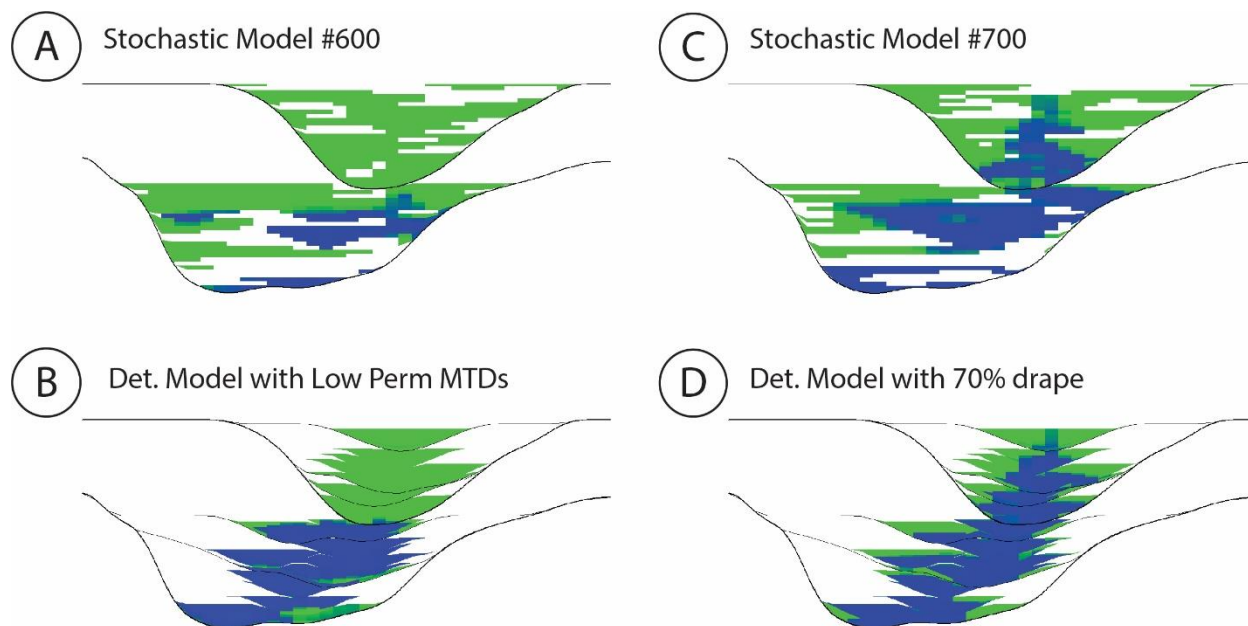


Figure 40. Comparison of flow behaviors between stochastic and deterministic flow simulations. (A) Stochastic model #600, with 30% MTD proportion. Flow is restricted between the upper and lower complex sets due to MTD placement. (B) Deterministic model with an MTD K_z value of 0.001 mD. MTDs significantly slow down fluid flow, resulting in extremely high BT and increased RE . (C) Stochastic model #700, with 30% MTD proportion. MTD facies act to funnel fluid flow, helping to quickly achieve BT . (D) Deterministic model with 70% *drape* coverage. Fluid flow is funneled, reducing BT .

5.3 Reservoir Compartmentalization

Much of this study focuses on the metric of recovery efficiency at water breakthrough. This is merely oil produced at a given time (e.g. BT) divided by the original oil in place ($OOIP$). While this metric is a succinct and effective way to compare the simulation results of different models, it does not provide a comprehensive explanation for what is really happening. What can be lost in this simple equation are the concepts of reservoir compartmentalization and bypassed pay.

Reservoir compartmentalization describes a scenario where specific reservoir zones are being siloed or isolated from the rest of the reservoir. The deterministic outcrop model exhibits this behavior in a few laterally divergent channel elements, which are entirely bypassed in all flow

simulations. Likewise, the randomly generated channels in the stochastic model series can be completely detached from the bulk of the reservoir, with no chance to contribute to production. Examples of each of these scenarios are shown in Figure 41. In both cases, these siloed reservoirs contribute to the *OOIP*, yet are completely bypassed by the producing wells, in effect lowering the overall *RE*.

While the vertically, diagonally, and laterally stacked simple model flow simulations also leave bypassed pay, the mechanism for this differs from that of the compartmentalization seen in the deterministic and stochastic models. Rather than containing sections of reservoir that are completely detached from the main body, the simple stacking patterns of the simple models result in one continuous “tank,” with all pay being connected. The bypassed pay is a result of water finding the most efficient path between aquifer and producer, not a lack of accessibility to all sections of the reservoir.

Additional metrics must be considered when evaluating flow simulation results, including *BT* and cumulative oil produced at a standard number of pore volumes injected. It is only through a combined viewing of the results that the true flow behavior trends begin to emerge.

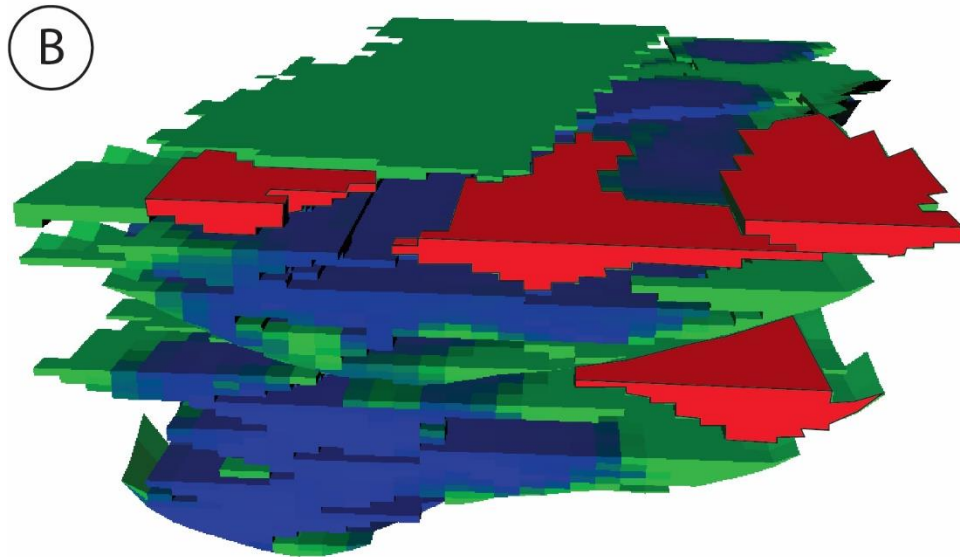
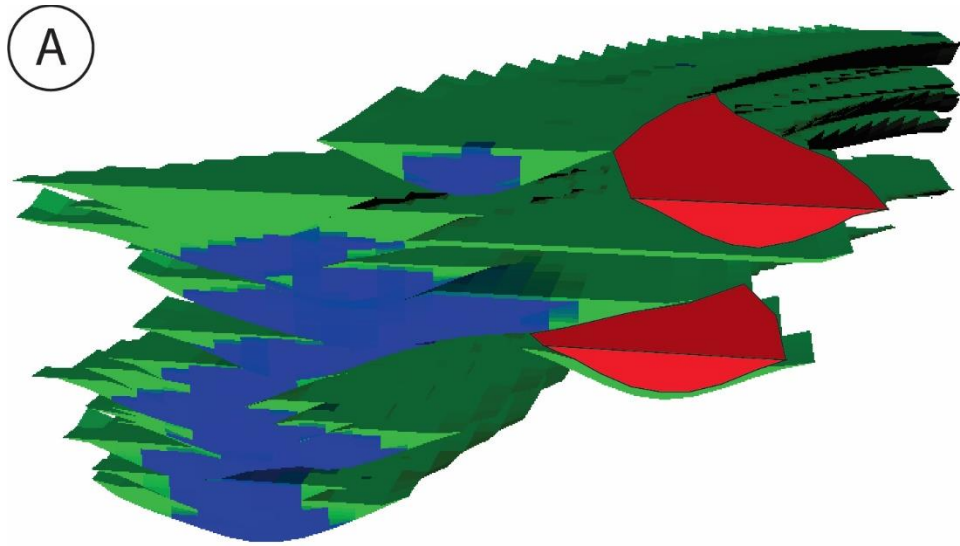


Figure 41. Flow simulation results highlighting reservoir compartmentalization (bypassed pay) in red. (A) Deterministic model with 50% *NTG*. (B) Stochastic model with 15% MTD facies.

CHAPTER 6: CONCLUSIONS AND FUTURE WORK

6.1 Conclusions

A three-part sensitivity analysis was conducted to answer the question of whether specific hierarchical architectural features had distinct characteristic flow behaviors, and if so, whether they could be modeled with stochastic modeling algorithms. Chapter one used simple, idealized models to isolate key flow characteristics related to channel element stacking pattern, net to gross ratio, and channel base drape coverage. Chapter two used a deterministic model of the Laguna Figueroa outcrop to build upon the simple model results using realistic stacking patterns and architectural features, including MTDs. Chapter three used stochastic object-based modeling with limited hard-data input to assess whether flow behaviors seen in the simple and deterministic models could be captured using standard geostatistical reservoir modeling methods. The three chapters of the analysis varied in complexity, and were meant to build upon each other to create a more robust depiction of the effects of the architectural elements being evaluated. Similar results were seen across all three chapters of the sensitivity analysis, highlighting the three key flow behaviors associated with flow baffles, flow barriers, and reservoir compartmentalization.

In all three phases of the analysis, *drapes* and/or low *NTG* margins acted as baffles to constrict fluid flow between adjacent channel elements, creating a funneling effect that reduced water *BT*. As *drape* was increased or *NTG* was lowered, a threshold was eventually reached whereby the flow baffle became a flow barrier, and *BT* was delayed or never reached. In the case of increasing *drape* coverage, the reduction in *BT* directly corresponded with a decrease in *RE*. With decreasing *NTG*, however, the reduction in *BT* was somewhat offset by a reduction in *OOIP*, resulting in a flatter *RE* curve.

In addition to *drape* and *NTG*, it was found that stochastically generated MTD objects could act as flow baffles when their placement did not completely block the flow path between

adjacent channel elements. However, when the stochastic placement of MTDs did completely obstruct the flow pathway, the low permeability features acted as flow barriers, similar to in the deterministic model. This discrepancy in the influence of stochastically generated MTDs on flow behavior points to the conclusion that object-based modeling in Petrel is not an effective method to reproduce MTDs. The naturally disjointed nature of the stochastic process often doesn't create a complete barrier between neighboring channel elements, resulting in more of a flow baffle than barrier.

This study also revealed that reservoir compartmentalization can be created in a variety of ways, including laterally divergent stacking patterns, channel base drape coverage, low *NTG* margins, and the presence of MTDs. This compartmentalization effectively reduces *RE*, as the total *OOIP* includes these sections of reservoir that are ultimately bypassed and unable to contribute to production. Compartmentalization was seen in all three phases of analysis. In the simple models, pay that was initially bypassed was generally recoverable in a long enough simulation. However, at very high *drape* levels in the diagonally and laterally stacked models, flow between adjacent channel elements was completely cut off, effectively siloing each element. In the deterministic model, the complex stacking patterns created impermeable boundaries between some adjacent channel elements in lower *drape* and higher *NTG* cases. Additionally, MTDs had the effect of compartmentalizing the reservoir when they were assigned extremely low K_z values. The stochastic models exhibited compartmentalization due to the stochastic object placement naturally producing disconnected elements.

Ultimately it is clear from this analysis that factors are influencing flow behavior in slope-channel systems at a variety of hierarchical levels, and a combination of modeling methods is critical to deciphering these patterns.

6.2 Future Work

Simple Models

The workflows used in the simple modeling chapter of the sensitivity analysis were direct and efficient, but could be expanded upon and improved. Ideally, a spectrum of stacking patterns would be examined, rather than the limited series of vertically, diagonally, and laterally stacked channels. This could illuminate thresholds for certain flow behaviors, and allow the simulation results to more effectively translate to the deterministic and stochastic models. Additionally, the workflow may be improved by testing alternative methods for creating channel base drapes. The transmissibility multiplier concept used was effective in the sense of restricting flow along the base of the channels, but wasn't necessarily representative of what a channel base drape might look like in outcrop.

Deterministic Model

The primary objective moving forward with the deterministic model would be to generally improve its realism. In this study, all zones apart from the channel elements and mass transport deposits were designated as "background" facies, and contained no storage or flow properties. This was done to simplify the results and maintain focus on the sensitivity variables being tested. In outcrop, these zones generally contain thin-bedded inner and outer levee facies, which could contribute to storage and allow for anisotropic fluid flow. Incorporating these levee facies would complicate the flow simulation results, but would contribute to the realism of the simulations.

Another avenue for increasing realism would be to incorporate asymmetry and more detailed facies distribution into the channel elements. The elements in the current model are entirely symmetrical and have hard *NTG* cutoffs to determine distribution of inter-channel facies,

whereas channel elements in outcrop are much more nuanced. While including finer-resolution heterogeneity within channel elements would be useful, it would also create problems with upscaling and creating models that could be flow simulated efficiently.

Additionally, some decisions were made when constructing the model that would be revised in future studies. Channel elements L11 and L12 in the Lower Figueroa appear to diverge, which is a result of a linear extrapolation of the partially interpreted L12 element. Realistically this element should have more closely followed the outcrop, which would change the stacking pattern slightly. The complex set surfaces used in the deterministic model are also considerably wider than those of the conceptual model, and contain too shallow of a slope along the edges. This was a result of the method used to construct these surfaces, but in a future study, efforts would be made to more closely match the conceptual model.

Stochastic Models

The methods used in the stochastic modeling chapter of the analysis could be improved in several ways to achieve more robust results. The object-based method used to recreate MTDs was largely ineffective, as the placement of the objects was not representative of what was seen in outcrop and they tended to act more as flow baffles than barriers. A different method would have to be used, perhaps with the aid of a more fixed hierarchical framework to facilitate a closer reproduction of the deterministic model. Additionally, the limited inputs available for the stochastic channel generation only included two facies: channel sands, and levees. In this study, channel sands were treated as axis, while levees were treated as off-axis. Should the study be replicated, the levees should be treated as an amalgamation of off-axis and margin, with an

appropriate reduction in porosity and permeability. Lastly, many more total model simulations would be useful to solidify the flow behavior trends observed and eliminate outliers.

Flow Simulations

One of the primary challenges with the flow simulation setup used in this study was that the constant flux analytic aquifer did not react to changes in reservoir pressure during simulation, and instead continued adding water to the system at a constant rate. When producing wells were unable to maintain production, such as after water breakthrough, the overall reservoir pressure tended to increase rapidly. While this is not expected to influence the overall results of the study, it is worth noting and should be addressed in future studies. A solution perhaps would be to have the aquifer flux controlled as a function of well production or reservoir pressure, rather than a constant. Alternatively, the actual simulation setup could be altered, such as by adding more producing wells or using a constant outflow rather than rate controlled producers.

Another thing worth noting is that the boundary conditions used in this study, namely the constant flux aquifer and impermeable background facies, likely had an impact on overall breakthrough times. A more realistic aquifer setting would more likely result in generally longer breakthrough times, as the aquifer would provide less supporting pressure as the reservoir was depleted.

REFERENCES

- Alpak, F. O., Barton, M. D., & Castineira, D. (2011). Retaining geological realism in dynamic modelling: a channelized turbidite reservoir example from West Africa. *Petroleum Geoscience*, 17(1), 35–52. <https://doi.org/10.1144/1354-079309-033>
- Alpak, F. O., Barton, M. D., & Naruk, S. J. (2013). The impact of fine-scale turbidite channel architecture on deep-water reservoir performance. *AAPG Bulletin*, 97(2), 251–284. <https://doi.org/10.1306/04021211067>
- Alpak, F. O., & van der Vlugt, F. F. (2014). Shale-Drape Modeling for the Geologically Consistent Simulation of Clastic Reservoirs. *SPE Journal*, 19(05), 832–844. <https://doi.org/10.2118/169820-PA>
- Alpak, F., Barton, M., Pirmez, C., Prather, B., & Tennant, S. (2008). Simplified modelling of turbidite channel reservoirs. *Society of Petroleum Engineers*, (January 2009), 41–51.
- Caers, J., & Zhang, T. (2005). Multiple-point geostatistics: A quantitative vehicle for integrating geologic analogs into multiple reservoir models. *AAPG Memoir*, (80), 383–394.
- Clark, J. D., & Pickering, K. T. (1996). Architectural elements and growth patterns of submarine channels: Application to hydrocarbon exploration. *AAPG Bulletin*, 80(2), 194–221. <https://doi.org/10.1306/64ed878c-1724-11d7-8645000102c1865d>
- Covault, J. A., Normark, W. R., Romans, B. W., & Graham, S. A. (2007). Highstand fans in the California borderland: The overlooked deep-water depositional systems. *Geology*, 35(9), 783–786. <https://doi.org/10.1130/G23800A.1>
- Covault, J. A., Romans, B. W., & Graham, S. A. (2009). Outcrop expression of a continental-margin-scale shelf-edge delta from the Cretaceous Magallanes Basin, Chile. *Journal of Sedimentary Research*, 79(7–8), 523–539. <https://doi.org/10.2110/jsr.2009.053>
- Covault, J. A., Sylvester, Z., Hubbard, S. M., Jobe, Z. R., & Sech, R. P. (2016). The Stratigraphic Record of Submarine-Channel Evolution. *The Sedimentary Record*, 14(3), 4–11. <https://doi.org/10.2110/sedred.2016.3.4>
- De Ruig, M. J., & Hubbard, S. M. (2006). Seismic facies and reservoir characteristics of a deep-marine channel belt in the Molasse foreland basin, Puchkirchen Formation, Austria. *AAPG Bulletin*, 90(5), 735–752. <https://doi.org/10.1306/10210505018>
- Deptuck, M. E., Steffens, G. S., Barton, M., & Pirmez, C. (2003). Architecture and evolution of upper fan channel-belts on the Niger Delta slope and in the Arabian Sea. *Marine and Petroleum Geology*, 20(6–8), 649–676. <https://doi.org/10.1016/j.marpetgeo.2003.01.004>

- Deptuck, M. E., Sylvester, Z., Pirmez, C., & O'Byrne, C. (2007). Migration-aggradation history and 3-D seismic geomorphology of submarine channels in the Pleistocene Benin-major Canyon, western Niger Delta slope. *Marine and Petroleum Geology*, 24(6–9), 406–433. <https://doi.org/10.1016/j.marpetgeo.2007.01.005>
- Fanchi, J. R. (2002). Chapter 16 - Improved Recovery. In *Shared Earth Modeling* (pp. 272–281). Butterworth-Heinemann. <https://doi.org/10.1016/B978-0-7506-7522-2.50016-1>
- Fildani, A., Cope, T. D., Graham, S. A., & Wooden, J. L. (2003). Initiation of the Magallanes foreland basin: Timing of the southernmost Patagonian Andes orogeny revised by detrital zircon provenance analysis. *Geology*, 31(12), 1081–1084. <https://doi.org/10.1130/G20016.1>
- Fildani, A., & Hessler, A. M. (2005). Stratigraphic record across a retroarc basin inversion: Rocas Verdes-Magallanes Basin, Patagonian Andes, Chile. *Bulletin of the Geological Society of America*, 117(11–12), 1596–1614. <https://doi.org/10.1130/B25708.1>
- Fosdick, J. C., Romans, B., Fildani, A., Bernhardt, A., Calderon, M., & Graham, S. A. (2011). Kinematic evolution of the Patagonian retroarc fold-and-thrust belt and Magallanes foreland basin, Chile and Argentina, 51°30'S. *Geological Society of American Bulletin*. <https://doi.org/10.1130/B30242.1>
- Hovadik, J. M., & Larue, D. K. (2007). Static characterizations of reservoirs: Refining the concepts of connectivity and continuity. *Petroleum Geoscience*, 13(3), 195–211. <https://doi.org/10.1144/1354-079305-697>
- Hovadik, J., & Larue, D. (2011). Predicting Waterflood Behavior by Simulating Earth Models with No or Limited Dynamic Data: From Model Ranking to Simulating a Billion-Cell Model. *Uncertainty Analysis and Reservoir Modeling: AAPG Memoir 96*, 29–55. <https://doi.org/10.1306/13301406M961028>
- Hubbard, S. M., Fildani, A., Romans, B. W., Covault, J. A., & McHargue, T. R. (2010). High-Relief Slope Cliniform Development: Insights from Outcrop, Magallanes Basin, Chile. *Journal of Sedimentary Research*, 80(5), 357–375. <https://doi.org/10.2110/jsr.2010.042>
- Hubbard, S. M., Covault, J. A., Fildani, A., & Romans, B. W. (2014). Sediment transfer and deposition in slope channels: Deciphering the record of enigmatic deep-sea processes from outcrop. *Bulletin of the Geological Society of America*, 126(5–6), 857–871. <https://doi.org/10.1130/B30996.1>
- Hubbard, S. M., de Ruig, M. J., & Graham, S. A. (2009). Confined channel-levee complex development in an elongate depo-center: Deep-water Tertiary strata of the Austrian Molasse basin. *Marine and Petroleum Geology*, 26(1), 85–112. <https://doi.org/10.1016/j.marpetgeo.2007.11.006>

- Hubbard, S. M., Fildani, A., Romans, B. W., Covault, J. A., & McHargue, T. R. (2010). High-relief slope cliniform development: Insights from outcrop, magallanes Basin, Chile. *Journal of Sedimentary Research*, 80(5–6), 357–375. <https://doi.org/10.2110/jsr.2010.042>
- Jackson, A., Stright, L., Hubbard, S. M., & Romans, B. W. (2019). Static connectivity of stacked deep-water channel elements constrained by high-resolution digital outcrop models. *AAPG Bulletin*, 103(12), 2943–2973. <https://doi.org/10.1306/03061917346>
- Jobe, Z. R., Howes, N. C., & Auchter, N. C. (2016). Comparing submarine and fluvial channel kinematics: Implications for stratigraphic architecture. *Geology*, 44(11), 931–934. <https://doi.org/10.1130/G38158.1>
- Kane, I. A., & Hodgson, D. M. (2011). Sedimentological criteria to differentiate submarine channel levee subenvironments: Exhumed examples from the Rosario Fm. (Upper Cretaceous) of Baja California, Mexico, and the Fort Brown Fm. (Permian), Karoo Basin, S. Africa. *Marine and Petroleum Geology*, 28(3), 807–823. <https://doi.org/10.1016/j.marpetgeo.2010.05.009>
- Katz, H. R. (1963). Revision of Cretaceous Stratigraphy in Patagonian Cordillera of Ultima Esperanza, Magallanes Province, Chile. *AAPG Bulletin*, 47(3), 506–524.
- Labourdet, R. (2007). Integrated three-dimensional modeling approach of stacked turbidite channels. *American Association of Petroleum Geologists Bulletin*, 91(11), 1603–1618. <https://doi.org/10.1306/06210706143>
- Labourdet, R., & Bez, M. (2010). Element migration in turbidite systems: Random or systematic depositional processes? *AAPG Bulletin*, 94(3), 345–368. <https://doi.org/10.1306/09010909035>
- Labourdet, R., Poncet, J., Seguin, J., Temple, F., Hegre, J. A., & Irving, A. (2006). Three-dimensional modelling of stacked turbidite channels in West Africa: Impact on dynamic reservoir simulations. *Petroleum Geoscience*, 12(4), 335–345. <https://doi.org/10.1144/1354-079306-705>
- Larue, D. K., & Hovadik, J. (2008). Why is reservoir architecture an insignificant uncertainty in many appraisal and development studies of clastic channelized reservoirs? *Journal of Petroleum Geology*, 31(4), 337–366. <https://doi.org/10.1111/j.1747-5457.2008.00426.x>
- Larue, D. K., & Hovadik, J. (2006). Connectivity of channelized reservoirs: a modelling approach. *Petroleum Geoscience*, 12(4), 291–308. <https://doi.org/10.1144/1354-079306-699>
- Lerat, O., Nivlet, P., Doligez, B., Lucet, N., Roggero, F., Berthet, P., ... Vittori, J. (2007). Construction of a stochastic geological model constrained by high-resolution 3D seismic data - Application to the Girassol field, offshore Angola. *Proceedings - SPE Annual Technical Conference and Exhibition*, 4, 2789–2804. <https://doi.org/10.2523/110422-ms>

- Li, H., & Caers, J. (2007). Hierarchic modeling and history matching of multiscale flow barriers in channelized reservoirs. *Proceedings - SPE Annual Technical Conference and Exhibition*, 1(August). <https://doi.org/10.2523/109252-MS>
- Li, H., & Caers, J. (2011). Geological Modelling and History Matching of Multi-Scale Flow Barriers in Channelized Reservoirs: Methodology and Application. *Petroleum Geoscience*, 17(1), 17–34. <https://doi.org/10.1144/1354-079309-825>
- Lowe, D. R. (1982). SEDIMENT GRAVITY FLOWS: II. DEPOSITIONAL MODELS WITH SPECIAL REFERENCE TO THE DEPOSITS OF HIGH-DENSITY TURBIDITY CURRENTS. *Journal of Sedimentary Petrology*, 52(1).
- Macauley, R. V., & Hubbard, S. M. (2013). Slope channel sedimentary processes and stratigraphic stacking, Cretaceous Tres Pasos Formation slope system, Chilean Patagonia. *Marine and Petroleum Geology*, 41(1), 146–162. <https://doi.org/10.1016/j.marpetgeo.2012.02.004>
- Mayall, Mike; Jones, Ed; Casey, M. (2006). Turbidite channel reservoirs - Key elements in facies prediction and effective development.
- McHargue, T., Pyrcz, M. J., Sullivan, M. D., Clark, J. D., Fildani, A., Romans, B. W., ... Drinkwater, N. J. (2011). Architecture of turbidite channel systems on the continental slope: Patterns and predictions. *Marine and Petroleum Geology*, 28(3), 728–743. <https://doi.org/10.1016/j.marpetgeo.2010.07.008>
- McHargue, T. R., Pyrcz, M. J., Sullivan, M., Clark, J. D., Fildani, A., Levy, M., ... Covault, J. A. (2011). Event-based modeling of turbidite channel fill, channel stacking pattern, and net sand volume. *Outcrops Revitalized: Tools, Techniques and Applications*, (10), 163–173.
- Meirovitz, C., Stright, L., Hubbard, S., & Romans, B. W. (2018). Impact of Channel-Fill Asymmetry in Field-Scale Dynamic Reservoir Performance Prediction for Deep-Water Channelized Turbidite Systems. In *AAPG ACE 2018*. Retrieved from <http://www.searchanddiscovery.com/abstracts/html/2018/ace2018/abstracts/2857529.html>
- Meirovitz, C. D., Stright, L., Hubbard, S. M., & Romans, B. W. (2020). The Influence of Inter- and Intra-channel Architecture on Deep-water Turbidite Reservoir Performance. *Petroleum Geoscience*. <https://doi.org/https://doi.org/10.1144/petgeo2020-005> To
- Moscardelli, L., & Wood, L. (2008). New classification system for mass transport complexes in offshore Trinidad. *Basin Research*, 20(1), 73–98. <https://doi.org/10.1111/j.1365-2117.2007.00340.x>
- Moscardelli, L., Wood, L., & Mann, P. (2006). Mass-transport complexes and associated processes in the offshore area of Trinidad and Venezuela. *American Association of Petroleum Geologists Bulletin*, 90(7), 1059–1088. <https://doi.org/10.1306/02210605052>

- Pemberton, E. A. L., Stright, L., Fletcher, S., & Hubbard, S. M. (2018). The influence of stratigraphic architecture on seismic response: Reflectivity modeling of outcropping deepwater channel units. *Interpretation*, 6(3), T783–T808. <https://doi.org/10.1190/int-2017-0170.1>
- Posamentier, H. W., & Kolla, V. (2003). Seismic geomorphology and stratigraphy of depositional elements in deep-water settings. *Journal of Sedimentary Research*, 73(3), 367–388. <https://doi.org/10.1306/111302730367>
- Romans, B. W., Fildani, A., Graham, S. A., Hubbard, S. M., & Covault, J. A. (2010). Importance of predecessor basin history on sedimentary fill of a retroarc foreland basin: provenance analysis of the Cretaceous Magallanes basin, Chile (50-52°S). *Basin Research*, 22(5), 640–658. <https://doi.org/10.1111/j.1365-2117.2009.00443.x>
- Romans, B. W., Fildani, A., Hubbard, S. M., Covault, J. A., Fosdick, J. C., & Graham, S. A. (2011). Evolution of deep-water stratigraphic architecture, Magallanes Basin, Chile. *Marine and Petroleum Geology*, 28(3), 612–628. <https://doi.org/10.1016/j.marpetgeo.2010.05.002>
- Shultz, M. R., & Hubbard, S. M. (2005). Sedimentology, stratigraphic architecture, and ichnology of gravity-flow deposits partially ponded in a growth-fault-controlled slope minibasin, Tres Pasos Formation (Cretaceous), southern Chile. *Journal of Sedimentary Research*, 75(3), 440–453. <https://doi.org/10.2110/jsr.2005.034>
- Southern, S.J., Stright, L., Jobe, Z.R., Romans, B., and Hubbard, S., 2017, The stratigraphic expression of slope channel evolution: insights from qualitative and quantitative assessment of channel fills from the Cretaceous Tres Pasos Formation, southern Chile: AAPG Annual Convention, Houston, TX, April 3-5, 2017.
- Sprague, A.R.G., Garfield, T.R., Goulding, F.J., Beaubouef, R.T., Sullivan, M.D., Rossen, C., Champion, K.M., Sickafoose, D.K., Abreu, V., Schellpeper, M.E. and Jensen, G.N., 2005. Integrated slope channel depositional models: the key to successful prediction of reservoir presence and quality in offshore West Africa. Veracruz, Mexico, Colegio de Ingenieros Petroleros de México, pp.1-13.
- Sprague, A. R. G., et al., 2002, The physical stratigraphy of deepwater strata: A hierarchical approach to the analysis of genetically related stratigraphic elements for improved reservoir prediction (abs.): Proceedings of the AAPG Annual Meeting, March 10–13, 2002, p. A167.
- Stright, L. (2006). Modeling, upscaling, and history matching thin, irregularly-shaped flow barriers: A comprehensive approach for predicting reservoir connectivity. *Proceedings - SPE Annual Technical Conference and Exhibition*, 7(Student 12), 5075–5082. <https://doi.org/10.2118/106528-stu>
- Sun, Q., & Alves, T. (2020). Petrophysics of fine-grained mass-transport deposits: A critical review. *Journal of Asian Earth Sciences*, 192(November 2019). <https://doi.org/10.1016/j.jseaes.2020.104291>

- Sylvester, Z., Pirmez, C., & Cantelli, A. (2011). A model of submarine channel-levee evolution based on channel trajectories: Implications for stratigraphic architecture. *Marine and Petroleum Geology*, 28(3), 716–727. <https://doi.org/10.1016/j.marpetgeo.2010.05.012>
- Talling, P. J., Masson, D. G., Sumner, E. J., & Malgesini, G. (2012). Subaqueous sediment density flows: Depositional processes and deposit types. *Sedimentology*, 59(7), 1937–2003. <https://doi.org/10.1111/j.1365-3091.2012.01353.x>
- Wilson, T. J. (1991). Transition from back-arc to foreland basin development in the southernmost Andes: stratigraphic record from the Ultima Esperanza District, Chile. *Geological Society of America Bulletin*, 103(1), 98–111.
- WINN, R. D., & DOTT, R. H. (1979). Deep-water fan-channel conglomerates of Late Cretaceous age, southern Chile. *Sedimentology*, 26(2), 203–228. <https://doi.org/10.1111/j.1365-3091.1979.tb00351.x>
- Zhang, X., Pyrcz, M. J., & Deutsch, C. V. (2009). Stochastic surface modeling of deepwater depositional systems for improved reservoir models. *Journal of Petroleum Science and Engineering*, 68(1–2), 118–134. <https://doi.org/10.1016/J.PETROL.2009.06.019>

Table A.1. Flow simulation results for vertically stacked simple models with varying drape coverage and NTG.

Stacking Pattern	Drape Coverage	NTG	Breakthrough (Days)	CUM Oil @ BT (stb)	OOIP	RE	CUM Oil @ 0.1 PVI
Vertical	0	1	2,261	16,956,020	106,289,285	0.16	12,233
Vertical	0.1	1	2,261	16,941,770	106,289,285	0.16	12,233
Vertical	0.2	1	2,259	16,941,770	106,289,285	0.16	12,233
Vertical	0.3	1	2,259	16,941,760	106,289,285	0.16	12,233
Vertical	0.4	1	2,264	16,977,400	106,289,285	0.16	12,233
Vertical	0.5	1	2,216	16,618,650	106,289,285	0.16	12,233
Vertical	0.6	1	2,090	15,674,290	106,289,285	0.15	12,233
Vertical	0.7	1	1,813	13,596,130	106,289,285	0.13	12,233
Vertical	0.8	1	1,484	11,126,060	106,289,285	0.10	12,014
Vertical	0.9	1	1,211	9,079,348	106,289,285	0.09	11,517
Vertical	0	1	2,261	16,956,020	106,289,285	0.16	12,233
Vertical	0	0.9	2,135	16,010,020	101,408,970	0.16	11,677
Vertical	0	0.8	1,967	14,751,330	95,900,380	0.15	11,040
Vertical	0	0.7	1,834	13,753,090	90,250,112	0.15	10,387
Vertical	0	0.6	1,666	12,492,690	83,718,021	0.15	8,887
Vertical	0	0.5	1,548	11,607,900	77,068,738	0.15	8,123
Vertical	0	0.4	1,374	10,302,290	69,116,754	0.15	7,958
Vertical	0	0.3	1,160	8,698,575	61,501,825	0.14	7,080
Vertical	0	0.2	885	6,630,962	52,964,319	0.13	6,096

Table A.2. Flow simulation results for diagonally stacked simple models with varying drape coverage and NTG.

Stacking Pattern	Drape Coverage	NTG	Breakthrough (Days)	CUM Oil @ BT (stb)	OOIP	RE	CUM Oil @ 0.1 PVI
Diagonal	0	1	5,320	39,899,910	105,377,377	0.38	12,180
Diagonal	0.1	1	5,325	39,937,360	105,377,377	0.38	12,180
Diagonal	0.2	1	5,325	39,937,360	105,377,377	0.38	12,180
Diagonal	0.3	1	5,325	39,937,360	105,377,377	0.38	12,180
Diagonal	0.4	1	5,100	38,249,930	105,377,377	0.36	12,180
Diagonal	0.5	1	4,770	35,774,830	105,377,377	0.34	12,180
Diagonal	0.6	1	4,650	34,874,790	105,377,377	0.33	12,180
Diagonal	0.7	1	4,905	36,787,210	105,377,377	0.35	12,180
Diagonal	0	1	5,320	39,899,910	105,377,377	0.38	12,180
Diagonal	0	0.9	5,190	38,924,900	100,985,854	0.39	11,667
Diagonal	0	0.8	5,115	38,362,390	95,564,657	0.40	11,047
Diagonal	0	0.7	4,920	36,899,800	89,692,106	0.41	10,365
Diagonal	0	0.6	4,560	34,199,910	82,839,485	0.41	9,577
Diagonal	0	0.5	4,230	31,724,860	76,108,250	0.42	8,797
Diagonal	0	0.4	7,625	30,616,180	68,689,968	0.45	1,774
Diagonal	0	0.3	10,150	24,240,090	60,547,355	0.40	986
Diagonal	0	0.2	11,400	19,766,040	52,854,666	0.37	734

Table A.3. Flow simulation results for laterally stacked simple models with varying drape coverage and NTG.

Stacking Pattern	Drape Coverage	NTG	Breakthrough (Days)	CUM Oil @ BT (stb)	OOIP	RE	CUM Oil @ 0.1 PVI
Lateral	0	1	6,800	50,998,450	110,432,534	0.46	12,772
Lateral	0.1	1	6,725	50,435,000	110,432,534	0.46	12,772
Lateral	0.2	1	6,550	49,123,130	110,432,534	0.44	12,772
Lateral	0.3	1	6,447	48,352,420	110,432,535	0.44	12,772
Lateral	0.4	1	6,500	48,745,680	110,432,536	0.44	12,772
Lateral	0	1	6,800	50,998,450	110,432,534	0.46	12,772
Lateral	0	0.9	6,725	50,437,410	105,485,481	0.48	12,202
Lateral	0	0.8	6,500	48,749,930	100,097,838	0.49	11,579
Lateral	0	0.7	6,050	45,373,620	93,781,698	0.48	10,845
Lateral	0	0.6	6,050	45,364,160	87,027,452	0.52	10,065
Lateral	0	0.5	15,350	32,092,000	79,410,051	0.40	1,203

Table A.4. Flow simulation results for the deterministic outcrop model with varying drape coverage, NTG, and MTD permeability.

NTG	Drape	MTD PermX (mD)	MTDPermZ (mD)	MTDPorosity	BT Time (Days)	CUM Oil @ BT (stb)	OOIP [STB]	RE	CUM Oil @ 0.1 PVI
1	0	1	1	0.01	9,810	147,148,500	359,353,838	0.41	41,430
1	0.1	1	1	0.01	9,780	146,699,000	359,353,838	0.41	41,430
1	0.2	1	1	0.01	9,750	146,248,000	359,353,838	0.41	41,430
1	0.3	1	1	0.01	9,630	144,449,600	359,353,838	0.40	41,430
1	0.4	1	1	0.01	9,630	144,448,600	359,353,838	0.40	41,430
1	0.5	1	1	0.01	9,480	142,199,200	359,353,838	0.40	41,430
1	0.6	1	1	0.01	9,240	138,598,300	359,353,838	0.39	41,430
1	0.7	1	1	0.01	8,490	127,348,500	359,353,838	0.35	41,430
1	0.8	1	1	0.01	8,160	122,399,600	359,353,838	0.34	41,430
1	0.9	1	1	0.01	7,740	116,098,500	359,353,838	0.32	41,430
1	0	1	1	0.01	9,810	147,148,500	359,353,838	0.41	41,430
0.9	0	1	1	0.01	9,330	139,948,100	344,981,568	0.41	39,765
0.8	0	1	1	0.01	8,790	131,847,500	327,853,905	0.40	37,800
0.7	0	1	1	0.01	8,040	120,597,100	309,403,227	0.39	35,670
0.6	0	1	1	0.01	6,930	103,946,400	289,266,907	0.36	33,345
0.5	0	1	1	0.01	5,760	73,963,770	265,052,501	0.28	24,880
0.4	0	1	1	0.01	4,830	48,303,840	240,141,771	0.20	18,461
0.3	0	1	1	0.01	3,420	34,202,710	212,434,296	0.16	16,331
0.2	0	1	1	0.01	2,370	23,583,640	184,230,030	0.13	14,056
1	0	0.010	0.001	0.01	30,900	37,504	359,353,838	0.10	1,906
1	0	0.050	0.005	0.01	17,290	76,874	359,353,838	0.21	4,469
1	0	0.1	0.01	0.01	15,210	107,005	359,353,838	0.30	7,902
1	0	0.2	0.02	0.01	13,480	132,198	359,353,838	0.37	14,496
1	0	0.5	0.05	0.01	12,040	153,629	359,353,838	0.43	27,913
1	0	1.0	0.1	0.01	11,440	161,803	359,353,838	0.45	37,882
1	0	10	1	0.01	9,900	148,500	359,353,838	0.41	41,430
1	0	100	10	0.01	8,250	123,750	359,353,838	0.34	41,430
1	0	1,000	100	0.01	6,750	101,249	359,353,838	0.28	41,430
1	0	10,000	1,000	0.01	6,800	102,000	359,353,838	0.28	41,430
1	0	792.5	792.5	0.01	6,480	97,199	359,353,838	0.27	41,430

Table A.5. Flow simulation results for stochastic modeling runs with varying proportion of MTD facies. Highlighted model runs did not achieve water breakthrough. Results continue on the following page.

Seed Number	MTD proportion	BT Time (Days)	CUMOil @ BT (stb)	OOIP [STB]	RE	CUMOil @ 0.1 PVI
100	0.04	9,930	148,946,500	405,216,932	0.37	46,620
200	0.04	2,800	41,997,210	353,069,062	0.12	21,195
300	0.04	4,375	65,622,330	329,276,396	0.20	22,185
400	0.04	17,930	111,686,900	341,013,925	0.33	33,318
500	0.04	3,955	59,324,380	339,296,632	0.17	22,305
600	0.04	14,465	98,083,960	313,984,322	0.31	47,271
700	0.04	13,420	52,770,430	333,206,961	0.16	8,625
800	0.04	-	-	-	-	-
900	0.04	26,700	86,569,010	335,101,877	0.26	53,168
1000	0.04	27,200	63,222,740	346,787,147	0.18	13,367
100	5.97	6,580	62,326,990	352,732,233	0.18	16,773
200	5.71	6,825	80,277,150	348,387,147	0.23	27,480
300	3.99	7,175	107,611,800	350,114,531	0.31	24,255
400	6.52	4,620	69,299,180	371,420,362	0.19	41,745
500	5.39	16,450	129,212,800	365,159,690	0.35	58,520
600	5.65	5,810	87,140,880	347,731,919	0.25	31,710
700	5.96	-	-	-	-	-
800	4.90	13,090	67,875,830	356,599,505	0.19	57,739
900	5.38	2,380	35,687,180	357,260,649	0.10	28,770
1000	6.55	3,045	45,673,540	322,522,914	0.14	26,760
100	9.62	3,430	51,448,360	349,849,571	0.15	13,830
200	9.93	3,745	56,172,860	335,018,040	0.17	19,740
300	10.28	4,935	70,664,310	358,150,885	0.20	54,945
400	10.19	2,240	33,597,120	376,642,485	0.09	13,950
500	10.00	4,025	60,371,690	333,930,384	0.18	19,680
600	9.78	5,355	80,324,800	363,343,251	0.22	22,020
700	10.60	4,305	64,573,480	341,784,362	0.19	26,325
800	9.95	-	-	-	-	-
900	10.86	7,140	107,098,800	370,786,341	0.29	45,945
1000	9.85	4,690	70,349,710	346,333,791	0.20	26,775
100	13.62	3,815	48,346,930	347,048,984	0.14	26,590
200	15.55	3,010	45,149,100	346,948,874	0.13	16,005
300	14.83	1,295	19,413,560	347,634,114	0.06	11,070
400	14.91	3,185	47,770,780	329,471,626	0.14	17,940
500	15.65	3,220	48,297,310	348,456,349	0.14	20,730
600	15.76	2,765	41,474,300	347,516,074	0.12	27,420
700	15.05	5,880	88,199,020	343,027,196	0.26	18,945
800	14.65	2,940	44,090,610	366,486,920	0.12	16,635
900	15.82	3,430	51,445,850	359,594,958	0.14	15,150
1000	15.06	5,985	89,774,450	341,663,306	0.26	30,015

Seed Number	MTD proportion	BT Time (Days)	CUMOil @ BT (stb)	OOIP [STB]	RE	CUMOil @ 0.1 PVI
100	19.840	7,000	104,999,400	354,969,919	0.30	26,700
200	20.260	4,270	64,047,860	314,892,479	0.20	14,250
300	19.780	3,990	59,845,710	351,895,357	0.17	11,940
400	20.400	2,205	33,069,750	329,532,223	0.10	13,965
500	19.500	3,255	48,821,840	338,900,382	0.14	13,425
600	19.740	3,535	53,023,090	365,641,018	0.15	17,190
700	20.350	3,780	56,695,340	368,962,398	0.15	17,880
800	20.030	2,625	39,364,840	350,394,211	0.11	15,150
900	19.240	4,060	60,887,620	340,028,921	0.18	11,775
1000	19.420	5,250	78,748,770	360,000,868	0.22	29,745
100	25.210	4,620	69,299,580	365,252,170	0.19	11,400
200	25.440	1,645	24,665,250	317,021,561	0.08	13,965
300	24.870	2,450	36,749,860	350,112,423	0.10	11,175
400	25.340	2,660	39,899,610	350,153,644	0.11	10,425
500	24.900	2,135	32,020,270	329,769,019	0.10	10,785
600	24.770	4,690	70,347,850	354,376,465	0.20	21,540
700	25.340	4,690	70,349,140	381,974,192	0.18	27,540
800	25.330	4,970	74,549,630	393,257,151	0.19	22,620
900	24.740	3,360	50,396,250	362,189,977	0.14	14,550
1000	24.540	5,635	84,524,830	372,623,097	0.23	22,860
100	31.480	6,510	97,648,370	361,142,470	0.27	11,115
200	31.070	2,380	35,699,160	369,577,642	0.10	12,495
300	30.680	2,485	37,274,880	324,072,817	0.12	9,885
400	30.570	2,905	43,572,000	343,029,252	0.13	9,900
500	30.610	2,695	40,406,590	356,950,410	0.11	10,650
600	29.990	8,295	123,091,400	340,489,341	0.36	40,635
700	30.020	2,590	38,846,050	361,682,907	0.11	17,475
800	30.230	2,450	36,742,130	363,761,083	0.10	11,655
900	30.170	3,465	51,974,790	362,503,653	0.14	13,980
1000	29.880	5,005	75,065,470	374,285,808	0.20	18,945

Table A.6. Flow simulation results for stochastic modeling runs with varying NTG.

Seed Number	Facies 1 NTG	Facies 2 NTG	Mean NTG	MTD proportion	BT Time (Days)	CUM Oil @ BT (stb)	OOIP [STB]	RE	CUM Oil @ 0.1 PVI
400	1	0.8	0.9641	0.15	3,290	49,349,480	341,618,758	0.14	18,600
400	0.9	0.7	0.8641	0.15	3,570	53,547,520	318,598,696	0.17	17,355
400	0.8	0.6	0.7641	0.15	3,290	49,349,760	295,578,635	0.17	16,095
400	0.7	0.5	0.6641	0.15	3,045	45,671,440	272,558,574	0.17	14,835
400	0.6	0.4	0.5641	0.15	2,765	41,474,310	249,538,513	0.17	13,590
400	0.5	0.3	0.4641	0.15	2,520	37,795,620	226,518,452	0.17	12,330
400	0.4	0.2	0.3641	0.15	2,240	33,599,890	203,498,391	0.17	11,085
500	1	0.8	0.9587	15.65	3,325	49,874,230	363,740,282	0.14	21,630
500	0.9	0.7	0.8587	15.65	3,255	48,822,260	339,127,342	0.14	20,175
500	0.8	0.6	0.7587	15.65	3,010	45,146,680	314,514,402	0.14	18,705
500	0.7	0.5	0.6587	15.65	2,765	41,472,160	289,901,461	0.14	17,235
500	0.6	0.4	0.5587	15.65	2,520	37,796,850	265,288,521	0.14	15,780
500	0.5	0.3	0.4587	15.65	2,275	34,121,820	240,675,580	0.14	14,310
500	0.4	0.2	0.3587	15.65	1,610	24,149,430	216,062,640	0.11	12,855
900	1	0.8	0.9594	15.82	3,535	53,023,480	374,830,014	0.14	15,780
900	0.9	0.7	0.8594	15.82	3,465	51,973,540	349,510,396	0.15	14,715
900	0.8	0.6	0.7594	15.82	3,220	48,295,070	324,190,779	0.15	13,650
900	0.7	0.5	0.6594	15.82	2,940	44,098,710	298,871,161	0.15	12,585
900	0.6	0.4	0.5594	15.82	2,695	40,420,290	273,551,544	0.15	11,520
900	0.5	0.3	0.4594	15.82	2,415	36,223,930	248,231,926	0.15	10,455
900	0.4	0.2	0.3594	15.82	1,925	28,873,380	222,912,309	0.13	9,390

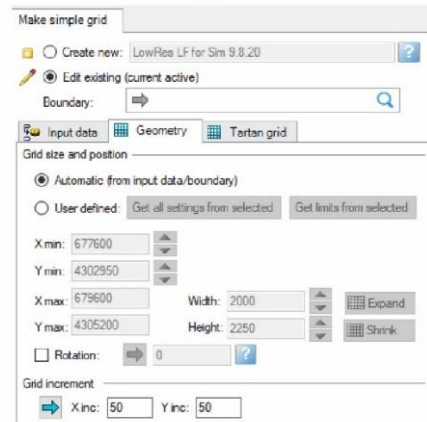
APPENDIX B

Table B.1. List of surfaces used in deterministic model.

Surface Name	Description	Horizon Type
Model Top	Top of Model	Conformatble
BLUE_RC_TOP	Top of element surface	Conformatble
BLU_400_25	Channel element surface	Conformatble
UC4_updated	Upper complex 4 surface	Base
GAB_RC_TOP	Top of element surface	Conformatble
GAB_400_25	Channel element surface	Conformatble
MIS_RC_TOP	Top of element surface	Conformatble
MIS_400_25	Channel element surface	Conformatble
LUC_RC_TOP	Top of element surface	Conformatble
LUC_400_25	Channel element surface	Conformatble
OC6_RC_TOP	Top of element surface	Conformatble
OC6_400_25	Channel element surface	Conformatble
GRE_RC_TOP	Top of element surface	Conformatble
GRE_400_25	Channel element surface	Conformatble
UC3_updated	Upper complex 3 surface	Base
UP_RC_TOP	Top of element surface	Conformatble
UP_400_25	Channel element surface	Conformatble
UC2_updated	Upper complex 2 surface	Base
LP_RC_TOP	Top of element surface	Conformatble
LP_800_25_2	Channel element surface	Conformatble
Smoothed_UpperCS	Upper complex set surface	Base
L12_RC_TOP	Top of element surface	Conformatble
L12_400_25	Channel element surface	Conformatble
L11_RC_TOP	Top of element surface	Conformatble
L11_400_25	Channel element surface	Conformatble
LC3_updated	Lower complex 3 surface	Base
L10_RC_TOP	Top of element surface	Conformatble
L10_400_25	Channel element surface	Conformatble
L9_RC_TOP	Top of element surface	Conformatble
L9_400_25	Channel element surface	Conformatble
L8_RC_TOP	Top of element surface	Conformatble
L8_400_25	Channel element surface	Conformatble
L7_RC_TOP	Top of element surface	Conformatble
L7_400_25	Channel element surface	Conformatble
L6_RC_TOP	Top of element surface	Conformatble
L6_400_25	Channel element surface	Conformatble
L5_RC_TOP	Top of element surface	Conformatble
L5_400_25	Channel element surface	Conformatble
LC2_updated	Lower complex 2 surface	Base
L4_RC_TOP	Top of element surface	Conformatble
L4_400_25	Channel element surface	Conformatble
L3_RC_TOP	Top of element surface	Conformatble
L3_400_25	Channel element surface	Conformatble
L2_RC_TOP	Top of element surface	Conformatble
L2_400_25	Channel element surface	Conformatble
L1_RC_TOP	Top of element surface	Conformatble
L1_400_25	Channel element surface	Conformatble
Smoothed_LowerCS	Lower complex set surface	Base
Model Base	Base of Model	Conformatble

Notes
All surfaces follow Model Top in layering.
RC = reservoir characterization. Surfaces were made for class project.
400_25 refers to 400m wide, 25m thick. Lower Pink is 800m wide.
All surfaces say "Copy of" in front of them because they are not original surfaces.
There is no Lower complex 1 surface because it coincides with the lower complex set surface.

Grid geometry



Input tabs for stochastic modeling in Petrel with 20% MTD proportion.

A



1. Fluvial channels [34%]

Settings | Layout | Section | Levee | Trends

Use body Modify body name: _____

Facies: 1: Highly A | Channel sand | Fraction (%) 34 | Upscaled (%) 42.84
 2: Semi-A | Levee | Fraction (%) 9.68

Number of channels: 10

Do not allow truncated channels at top of zone
 Do not allow truncated channels at base of zone
 Let levee erode older channels

Settings | Layout | Section | Levee | Trends

Channel | Wavelength | Amplitude

	Drift [0-1]	Min	Med/mean	Max/std		
Orientation	Triangul	0.2	15	20	25	[Compass degrees]
Amplitude	Triangul	0.2	200	400	600	[Horizontal distance units]
Wavelength	Triangul	0.2	1500	2000	2500	

If using flow lines in the 'Trend' tab, the orientation will not be used.

Settings | Layout | Section | Levee | Trends

Intersection view: Width | Thickness

	Drift [0-1]	Min	Med/mean	Max/std		
Width	Triangul	0.2	350	400	450	[Horizontal distance units]
Thickness	Triangul	0.2	25	25	25	<input type="checkbox"/> Width fraction

Settings | Layout | Section | Levee | Trends

Thickness | Width

	Drift	Min	Med/mean	Max/std	
Width	Triangul	0.2	0.25	0.3	

Width unit: Frac. of channel width Horizontal distance units

	Thickness	Drift	Min	Med/mean	Max/std	
Thickness	Triangul	0.2	0.5	0.6	0.7	[Relative to channel thickness]

Approximate facies %: Channel 27.88 | Levee 6.12

B



5. Lower half pipe [20%]

Settings | Geometry | Trends | Rules

Use body Modify body name: _____

Facies: 5: MTD | Fraction (%) 20 | Upscaled (%) 17.33

Number of objects: 10

Do not allow truncated objects at top of zone
 Do not allow truncated objects at base of zone

Settings | Geometry | Trends | Rules

Body shape: Lower half pipe | Orientation: Major width | Minor width

	Min	Med/mean	Max/std		
Orientation	Triangul	15	20	25	[Compass degrees]
Minor width	Triangul	1500	2000	2500	[Horiz. distance units]
Maj/Min ratio	Triangul	1.5	2	2.5	
Thickness	Triangul	5	10	15	<input type="checkbox"/> Fraction of width [Fraction of length]

Settings | Geometry | Trends | Rules

Insert ONLY in the following facies: _____

Replace NONE other facies
 Replace ALL other facies (default)
 Replace ONLY the following facies: _____
 Replace ALL but the following facies: _____

Replace stratigraphically older bodies only

Whole body must fit in insertion facies (but may be partly outside model).
 Replace itself. If not only 'isolated' objects will be made.

APPENDIX C

Example .data file for a Vertically Stacked Simple Model For use with Schlumberger ECLIPSE (SimLauncher Version 2016.2.0.0)

```

----- Regions Section -----
-- This section is optional and is not needed for this case
REGIONS

-- Fluid in place regions as channels
INCLUDE
'YS15_FIPRegion.dat' /

----- Solution Section -----
-- Implies the beginning of Solution section
SOLUTION

-- Specify initial state of the reservoir
EQUIL -- DATA FOR INITIALISING FLUIDS TO POTENTIAL EQUILIBRIUM
-- DATUM DATUM DIVE DIVE GDC GDC GDC RSVB RSVB SOLM
-- DEPTH PRESS DEPTH PCOW DEPTH PCOW TABLE TABLE METH
0.0 4800 700.0 0.0 -700 0.0 1 0 0
/

AQUFLUX
1 0.00159 /
/

AQLIANCON
-- Aquifer 1
1 1 134 1 160 34 34 'K* 2* YES' /
/

RPTSOL
'FIP=1'
/

----- Summary Section -----
-- This section is optional, but needed in this case to plot line graphs
-- Implies the beginning of Summary section
SUMMARY

-- Tabulate output of summary file data

RUNSUM
SERIATE
RPTONLY
FOPT
FPR
FWCT
FOPR -- FIELD OIL PRODUCTION RATE
FOE -- request oil recovery

WVPR
'PROD'
/
VWCT
'PROD'
/
WOPR
'PROD'
/
WOPT
'PROD'
/
WBHP
'PROD'
/
/
RWFT
1 2 /
2 3 /
3 4 /
4 5 /
/

--EXCEL

----- Schedule Section -----
-- Implies the beginning of Schedule section
SCHEDULE

-- Controls what outputs are printed to PRT file
RPTSH:HED
'FIP=2' 'SUMMA Rvw1' 'WELLS=2' 'WELPS=3' /
-- Controls what files are every report time
RPTST
'BASIC=2'
/

-- Apply fully implicit solution procedure
IMPICIT

-- Set simulator control parameters
TUNING
-- TSMIN TSMAX2 TSMIN2 TSMIN3 TSMIN4 TSMIN5 TSMIN
1 50 0.1 0.15 5.0 0.0 /
-- TRGTT TRGCLN TRGMETRGCLV
0.1 0.0 /
-- NEWTMIN NEWTMIN2 LTMX LTMIN
40 1 40 1 /

-- TUNING -- min/max timestep [3 sections]
--0.1 100 /
--0.1 1 /
--2*60 /

WELLSPEC == WELL SPECIFICATION DATA
-----
-- WELL GROUP LOCATION BHP PI
-- NAME NAME 1 J DEPTH DEN
'PROD' 'PROD' 67 80 1* 'OIL' 2* 'STOP' 'YES' / -- 0* 'STD' / -- see ECL Manual for details
'PROD' 'PROD' 67 1 1* 'OIL' 2* 'STOP' 'YES' / -- 0* 'STD' / -- see ECL Manual for details
'PROD' 'PROD' 67 160 1* 'OIL' 2* 'STOP' 'YES' / -- 0* 'STD' / -- see ECL Manual for details
/

COMPDAT -- COMPLETION SPECIFICATION DATA
-- WELL LOCATION OREN SAT COBN WELL KH S D AXIS
-- NAME 1 J K1 K2 SHUT TRFACCT DAM
'PROD' 67 80 1 1 'OPEN' 0 -1 0.5 / -- see ECL manual for details
'PROD' 67 1 1 1 'OPEN' 0 -1 0.5 / -- see ECL manual for details
'PROD' 67 160 1 1 'OPEN' 0 -1 0.5 / -- see ECL manual for details
/

WCONPROD -- PRODUCTION WELL CONTROLS
-- WELL OREN CTRL OIL WATER GAS LIQU RES BHP
-- NAME SHUT MODE RATE RATE RATE RATE
'PROD' 'OPEN' 'LEAT' 3* 2500 1* 1000 / -- see ECL manual for details
'PROD' 'OPEN' 'LEAT' 3* 2500 1* 1000 / -- see ECL manual for details
/

-- Insteage can be refined by entering multiple TSTEP keywords
TSTEP -- and run it for 10 yrs, reporting every 10 days
365*7
/

END

```